Seismic and aseismic slip pulses driven by thermal pressurization of pore fluid

D. I. Garagash[1]

Received 23 September 2011; revised 16 February 2012; accepted 21 February 2012; published 26 April 2012.

[1] There are several lines of evidence that suggest that thermal pressurization (TP) of pore fluid within a low-permeability fault core may play the key role in the development of earthquake slip. To elucidate effects of TP on spontaneous fault slip, we consider solutions for a steadily propagating slip pulse on a fault with a constant sliding friction, the level of which may reflect other thermally-activated processes at the rupture front (such as the flash heating on asperities). Upon arrival of the pulse front, essentially undrained-adiabatic TP takes place during the initial slip acceleration from the locked state with a corresponding reduction of the fault strength. With passage of time, the diminishing rate of heating (due to the reduced fault strength) and increasing rate of hydrothermal diffusion from the shear zone offset TP and result in partial recovery of the strength, slip deceleration and eventual locking and healing of the slip. We show that the rupture speed v_r decreases with thickness h of the principal shear zone. For lab-constrained values of fault-gouge parameters, the TP-pulse solution predicts seismic ($v_r \sim$ km/s) slip on a millimeter-to-cm thin principal shear zone; and aseismic slip with $v_r \sim 10$ km/day and slip rates 1–2 orders above the plate rate on a relatively thick ($h \sim 1$ m) shear zone. These and other predictions of the TP-pulse model are consistent with the independent sets of observational constraints for large crustal and subduction interplate earthquakes, and slow slip transients (North Cascadia), respectively. Locking of the slip soon after the diffusive transport of the heat and pore fluid becomes efficient significantly limits the maximum co-seismic temperature rise to values well below previous theoretical estimates. As a result, the onset of macroscopic melting and some of thermal decomposition reactions, recently suggested to explain strong co-seismic fault weakening, are precluded over much of the seismogenic zone.

Citation: Garagash, D. I. (2012), Seismic and aseismic slip pulses driven by thermal pressurization of pore fluid, *J. Geophys. Res.*, *117*, B04314, doi:10.1029/2011JB008889.

1. Introduction

[2] In recent years, a self-consistent hypothesis of low-heat, low-stress operation of earthquake slip on statically-strong but dynamically-weak faults [*Lapusta and Rice*, 2003b; *Rice*, 2006; *Noda et al.*, 2009] has been put forward in general agreement with the three important observations for some of well-studied mature faults: 1) low ratio $\tau^b/\bar{\sigma}_0 \sim 0.06$–$0.4$ of the background shear stress τ^b to the ambient level of the effective normal stress $\bar{\sigma}_0$ resolved onto the fault plane [e.g., *Townend and Zoback*, 2004]; 2) high static (interseismic) strength of fault rocks, $\tau/\bar{\sigma}_0 \sim 0.6$–$0.9$, based on laboratory friction experiments at very low slip rates [*Byerlee*, 1978]; and 3) low average level of the co-seismic fault strength $\tau/\bar{\sigma}_0 \lesssim 0.1$ as suggested by the lack of detectable heat flow anomalies near major fault zones [*Brune et al.*, 1969; *Lachenbruch and Sass*, 1980], assuming $\bar{\sigma}_0 \sim 100$ MPa at the midseismogenic depth, and conspicuous absence of pseudotachylytes in natural faults exhumed from seismogenic depth [e.g., *Sibson and Toy*, 2006].

[3] In this hypothesis, ruptures nucleate on small patches that are either statically weak, or more likely subjected to a locally peaked background stress. The ruptures then propagate out along the fault driven by a much lower, average background stress, with such propagation enabled by strong fault weakening process(es) activated during dynamic slip. This dynamic weakening can be a result of a number of physical processes activated by fault frictional heating with slip, depending on gouge properties and prevailing fault conditions [e.g., *Rice*, 2006; *Di Toro et al.*, 2011, and references therein], with the most ubiquitous ones being thermal pressurization (TP) of pore fluid [*Sibson*, 1973] and flash heating (FH) at microscopic asperity contacts [*Rice*, 1999, 2006].

[4] Building on earlier work [*Lachenbruch*, 1980; *Mase and Smith*, 1987], recent analytical studies of co-seismic TP in the approximation of kinematic slip and constant fault sliding friction, and constrained with lab-derived properties of fault gouge [*Rice*, 2006; *Rempel and Rice*, 2006; *Noda*

[1]Department of Civil and Resource Engineering, Dalhousie University, Halifax, Nova Scotia, Canada.

0148-0227/12/2011JB008889

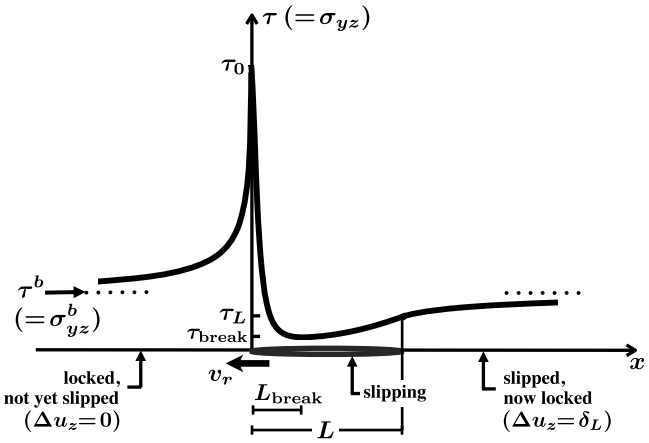

Figure 1. Sketch of a slip pulse and corresponding stress evolution.

and Shimamoto, 2005] provided strong support to the hypothesis. They showed that TP may result in near complete loss of fault strength at large slip, which in turn may limit the temperature rise to values short of the melting threshold in seismogenic crust. The predicted fracture energy and characteristic slip weakening distance in the earthquake slip were found to be in plausible agreement with the seismological estimates.

[5] A number of concurrent numerical studies of spontaneous dynamic slip with thermal pressurization [*Andrews*, 2002; *Bizzarri and Cocco*, 2006a, 2006b; *Noda and Lapusta*, 2010] and, in some cases, also accounting for the flash heating [*Noda et al.*, 2009], provided further validation of the hypothesis. The latter showed that the FH and TP favor the pulse mode of earthquake rupture at low levels of the background stress. However, these solutions have faced strong computational challenges related to the need to accurately resolve various physical processes over a wide range of temporal, spatial, and slip scales, e.g., slip distances associated with evolution of the state of the frictional contact are ~asperity size (10 s micrometers), diffusion of heat and pore fluid takes place on the scale ~millimeters to cms, and stress perturbations on the rupture scale ~kms (see *Noda et al.* [2009] for discussion), and, thus, have been limited in scope to a number of numerical examples.

[6] In this paper we attempt to study the TP effect during spontaneous elastodynamic slip within the constraints of a simplified model which, on one hand, is tractable by analytical and/or efficient numerical methods, and, on the other hand, retains the essential features of the phenomena reviewed in the above. The model that we use is of a spontaneous, steadily propagating slip pulse driven by a uniform background stress under the assumption of a constant sliding friction (friction along the slipping patch) (Figure 1). As in the now standard model of thermal pressurization, slip is accommodated within a saturated gouge layer of a fixed thickness, which is heated by frictional heat and pressurized by the thermal expansion of the pore fluid under conditions when the drainage of the fluid and the heat from the shear zone is limited on the timescale of the slip (Figure 2).

[7] The choice of the self-healing slip-pulse mode for rupture propagation is motivated by the strong seismological evidence [*Heaton*, 1990] that ruptures tend to propagate as pulses with a slip duration (risetime) much shorter than the total event duration. The pulse-mode has also been linked theoretically to low levels of the background, driving stress [*Zheng and Rice*, 1998; *Noda et al.*, 2009] as often inferred

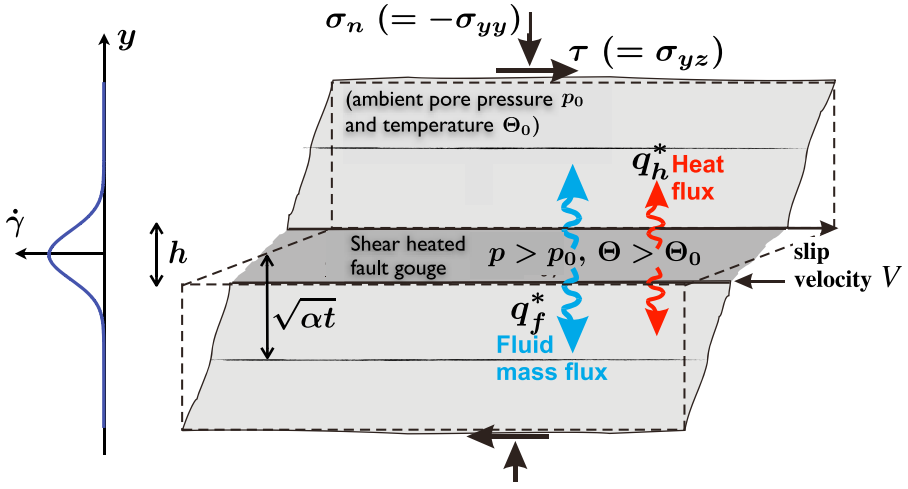

Figure 2. Sketch of a frictionally-heated, saturated fault shear zone.

for major faults. The constant sliding friction may be an appropriate description under the circumstances that the other dynamic fault weakening processes (e.g., FH) have not yet been activated (i.e., the slip rates are below the FH onset rate [*Rice*, 2006; *Beeler et al.*, 2008]), or, quite to the opposite, FH has been activated due to dramatic slip acceleration very near the front of the propagating rupture, which effectively reduced the friction to a nominal (low) dynamic level that is maintained over the majority of the slipping patch with the exception of the trailing edge [*Noda et al.*, 2009]. We note here that FH does require significant localization of slip (to ensure sufficiently high slip rates at the asperity/grain scale), and therefore is not a certain quantity during the dynamic slip. Although, evidence for a requisite level of seismic slip localization has been observed in exhumed fault zones [e.g., *Chester et al.*, 2004] and from theoretical analysis of distributed slip [*Platt et al.*, 2010; J. R. Rice and J. W. Rudnicki, unpublished manuscript, 2006].

[8] Our simple model does not account for any of the previously-proposed slip-healing mechanisms, including velocity-weakening friction [*Cochard and Madariaga*, 1994; *Perrin et al.*, 1995; *Beeler and Tullis*, 1996; *Zheng and Rice*, 1998; *Noda et al.*, 2009], heterogeneities/barriers along the fault plane [e.g., *Day*, 1982; *Johnson*, 1990], and a material contrast across it [*Andrews and Ben-Zion*, 1997]. Yet, we suggest that the pore fluid and heat transport from the heated zone alone can sufficiently offset the pressurization (most pronounced during the initial undrained-adiabatic response of the gouge) over the duration of slip in the pulse, in order to partially restrengthen the slipping fault, lock the slip, and insure restrengthening rates in the wake of the pulse that are higher than the rate of elastic stress rebound (as necessary for the slip to stay "healed" there). This new slip healing mechanism might have been observed in numerical solutions of *Noda et al.* [2009] and *Noda and Lapusta* [2010], yet has not been acknowledged by these authors, due to, presumably, attributing it to the velocity-weakening nature of the friction constitutive law in their treatments.

[9] This paper is organized as follows. In sections 2 and 3 we formulate the proposed model of a steady TP pulse propagation with a constant sliding friction, discuss the corresponding background on the thermal pressurization modeling and pertinent range of fault parameters, and lay down the argument for the possible self-healing nature of these pulses. Section 4 deals with the asymptotic solutions for small-slip pulses that are borne under conditions when the background shear stress is close to the nominal fault strength, $\tau^b/\tau_0 \approx 1$. (The existence of these solutions indicates that the smallness of background stress may not be necessary prerequisite for the pulse-like mode of rupture propagation). It is in this case that we first explore the range of TP pulse solutions as a function of the slip duration, and show that the pulse with the maximum slip duration, set by the timescale of hydrothermal diffusion across the shear zone, possesses the intrinsic self-healing property. The pulses with shorter slip durations (the shortest one corresponding to the undrained-adiabatic conditions everywhere along the pulse), if exist in nature, have to be "healed" by other physical processes, mentioned in the above and not accounted for explicitly in the model. Section 5 presents the general TP pulse solution as a function of the background stress $\tau^b/\tau_0 \leq 1$ in the two bounding regimes corresponding to the undrained-adiabatic slip and the partially-drained, self-healing slip, respectively. Section 6 is concerned with the large-slip limit of these solutions realized under small background stress, $\tau^b/\tau_0 \ll 1$.

[10] Section 7 discusses the important features of the presented TP pulse solutions, constraints set on them by observations, and the implications for seismogenesis. In sections 7.1 and 7.2, we show that the issue of the principal shear zone thickness is critical for defining the main properties of a spontaneous TP slip pulse. Specifically, we predict that shear zones that are relatively thin, cm or less, can only support dynamic rupture pulse propagation at ~km/s, while sufficiently thick (~meter) zones favor aseismic slip pulses propagating at speeds ~kms/day that are representative of slow slip transients observed in the transitional zone of subduction megathrusts (see review by *Schwartz and Rokosky* [2007]). (The latter observation is further explored in section 7.7, where we contrast the properties of aseismic TP pulses with the main spatio/temporal characteristics of along-strike propagation of slow slip transients on the Northern Cascadia subduction interface [*Dragert et al.*, 2001], and argue that TP may be one of the dominant mechanisms governing the slow slip). Sections 7.4 and 7.5 discuss the two related issues, 1) the well-defined slip scale over which most of the fault strength weakening takes place during what is essentially the undrained-adiabatic, initial phase of the pulse before the diffusive transport becomes efficient; and 2) the peak temperature rise, that is much smaller than otherwise anticipated in the kinematic solutions [*Rempel and Rice*, 2006], and generally insufficient to allow for macroscopic melting and some of thermal decomposition reactions that have been suggested recently as candidates for strong co-seismic fault weakening. Section 7.6 presents matching of the TP-model predictions with the data for sets of crustal and large subduction interplate earthquakes. We summarize the findings of our study in section 8.

2. Model

[11] A fault zone parallel to the $y = 0$ plane is sheared at the rate $\dot{\gamma} = \dot{\gamma}(y, t)$ (Figure 2). The 'net' slip velocity $V(t)$ and a characteristic thickness h of the region, centered about $y = 0$, where most of the slip is localized to are defined as

$$V(t) = \int_{-\infty}^{\infty} \dot{\gamma}(y,t)dy \quad \text{and} \quad h = \frac{V(t)}{\dot{\gamma}(0,t)}, \tag{1}$$

respectively. h is time-independent for shear distributions with uniform temporal dependence, i.e. when $\dot{\gamma}(y, t)/\dot{\gamma}(0, t)$ is a function of y only. Formally, this class of distributions can then be defined in terms of an arbitrary function g as,

$$\dot{\gamma}(y,t) = \frac{V(t)}{h} g\left(\frac{y}{h}\right), \quad \text{with} \quad g(0) = \int_{-\infty}^{\infty} g(s)ds = 1. \tag{2}$$

For a uniform shear distribution over a region of thickness h, $g(s) = 1$ when $|s| \leq 0.5$ and 0 when $|s| > 0.5$. For a Gaussian shear distribution, $g(s) = \exp(-\pi s^2)$, which is equivalent to the notation used by *Andrews* [2002] and *Rice* [2006] when their thickness parameter w is set to $h/\sqrt{2\pi}$.

[12] By mechanical equilibrium, the shear τ and the normal σ stresses are uniform across the fault zone, while the

value of σ is also unchanged with the slip: $\tau = \tau(t)$ and $\sigma = const.$ For the duration of slip τ is equal to the frictional strength τ_f,

$$\tau_f = f(\sigma - p) = f\ \bar{\sigma}, \tag{3}$$

in which f is the friction coefficient, p is the pore pressure, and $\bar{\sigma}$ is the effective normal stress. Generally, pore pressure is non-uniform across the fault, $p = p(y, t)$, in response to the non-uniformly distributed shear heating rate and pore fluid diffusion. As the result, applying $\tau = \tau_f$ across the shear zone requires to explicitly account for the dependence of f on (among other things) an a priori unknown shear rate $\dot{\gamma}(y, t)$ [*Platt et al.*, 2010]. Instead, a simplified approach is usually adopted [*Andrews*, 2002; *Rice*, 2006; *Rempel and Rice*, 2006; *Bizzarri and Cocco*, 2006a; *Noda et al.*, 2009], when (*i*) f is considered a function of the 'net' fault variables only (e.g., slip velocity or slip); (*ii*) all variables in (3) are evaluated at the midplane $y = 0$, where maximum pressurization is anticipated, and (*iii*) particular form of spatial distribution of shear, uncoupled from the solution, is postulated as a part of the fault model. Homogeneous and Gaussian shear distributions localized in a narrow region of invariant thickness h have been previously considered for faults during earthquake slip, while observational [e.g., *Wibberley and Shimamoto*, 2003; *Chester and Chester*, 1998; *Chester et al.*, 2004; *Rice*, 2006] and theoretical [*Platt et al.*, 2010] constraints are used to estimate h. Values of h in the cm to sub-mm range, and as low as $\sim$100 μm, have been suggested for seismic slip on mature faults, possibly, as the result of severe slip localization [*Platt et al.*, 2010]. On the other hand, much larger values of h are not ruled out at slow slip on mature faults with a well-developed gouge, as in earthquake nucleation or aseismic slip transients.

[13] Although the friction coefficient f is generally a function of the slip process, which is inherently dependent on physical processes activated by the fault slip, a constant friction approximation is used in this study. This approximation can be justified in two distinct cases.

[14] First, when the actual variation of fault friction in the course of the slip is small (for example when the slip and/or slip rate are small), and the corresponding impact on the fault strength (3) is negligible compared to that of the changes of the effective stress (pore pressure) due, in the context of this work, to the thermal pressurization effects. In this case, and, say, for statically strong faults, the constant fault friction can be approximated by Byerlee's values $f_p \approx 0.6$–0.8.

[15] Second, when the changes of the friction coefficient in the course of slip are not small but localized near the rupture advancing front and the trailing edge (for a pulse-like rupture). Numerical simulation of slip on statically-strong but dynamically weak faults [*Noda et al.*, 2009], whose weakening is governed by thermal pressurization (changes to the effective normal stress) and flash heating on asperities (changes to the friction coefficient) [*Rice*, 2006; *Beeler et al.*, 2008], show that the reduction of the friction coefficient takes place in a extremely thin zone near the rupture front over slip distances $\delta_{FH} \sim$ 10 s to 100 s μm associated with the evolving state of frictional contact. (The increase of the friction coefficient from the dynamic back to the static value at the trailing edge of a self-healing pulse in the simulations of *Noda et al.* [2009] occurred within a similarly thin end zone). In this case, the friction coefficient can be approximated away from the rupture edge by its dynamically-reduced value, reported $f_w \approx 0.1$–0.25 for crustal rocks [*Beeler et al.*, 2008; *Hirose and Bystricky*, 2007; *Kohli et al.*, 2011]. In this scenario we will assume that the fracture energy associated with the reduction of the friction coefficient from the static f_p to dynamic f_w value is negligible compared to other energy sinks (in our case the fracture energy associated with TP). We re-evaluate this assumption once we establish the corresponding slip-pulse solutions.

2.1. Thermal Pressurization of Pore Fluid

[16] Shear heating of the fault and associated pore fluid pressurization is governed by equations of energy and fluid balance together with the corresponding transport laws [e.g., *Rice*, 2006]:

$$\rho c\dot{\Theta} = \tau(t)\dot{\gamma}(t,y) - \frac{\partial q_h}{\partial y}, \quad q_h = -K\frac{\partial \Theta}{\partial y}, \tag{4}$$

$$\rho_f \beta\left(\dot{p} - \Lambda\dot{\Theta}\right) = -\frac{\partial q_f}{\partial y}, \quad q_f = -\rho_f \frac{k}{\eta_f}\frac{\partial p}{\partial y}, \tag{5}$$

where ρc is the volumetric heat capacity of the fault material, β is the fluid storage coefficient, Λ is the fluid thermal pressurization factor, and K and k/η_f are the thermal and hydraulic conductivities in the respective expressions for the energy, q_h, and fluid mass, q_f, fluxes normal to the fault (Figure 2). The fluxes along the fault have been neglected on the assumption that the shear zone thickness h, as well as, thickness of induced thermal and hydrological boundary layers are small compared to the slipping patch dimensions. Additionally, we have assumed that the inelastic dilation [*Segall and Rice*, 1995, 2006] within the shear zone is either negligible or is localized to the advancing front of the rupture, in which case its effect can be accounted for by using an effective (reduced) value of the ambient pore pressure p_0 ahead of the main rupture slip [e.g., *Rice*, 2006].

[17] *Rempel and Rice* [2006] and *Vredevoogd et al.* [2007] observed that the effect of non-linearity of (4) and (5) due to the temperature and pressure dependence of fault material parameters, is small, more so when the path-averaged values of these parameters were used. Consequently, we adopt a linearized version of (4) and (5):

$$\dot{\Theta} = \frac{\tau(t)\dot{\gamma}(t,y)}{\rho c} + \alpha_{th}\frac{\partial^2 \Theta}{\partial y^2}, \qquad \dot{p} - \Lambda\dot{\Theta} = \alpha_{hy}\frac{\partial^2 p}{\partial y^2}, \tag{6}$$

where $\alpha_{th} = K/(\rho c)$ and $\alpha_{hy} = k/(\eta_f \beta)$ are the thermal and hydraulic diffusivities, respectively.

[18] From the onset of slip at a given location along the fault, $t \geq 0$, the rise of temperature and fluid pressure induced by the shear heating within the localized shear zone of thickness h is continually redistributed by diffusive transport of heat and fluid mass over thermal and hydrological boundary layers $\sim\sqrt{4\alpha_{th}t}$ and $\sqrt{4\alpha_{hy}t}$, respectively (Figure 2). During the *early-time*, *undrained response* of the shear zone, these boundary layers are small, $\sqrt{4\alpha t} \ll h$, where $\alpha = (\sqrt{\alpha_{th}} + \sqrt{\alpha_{hy}})^2$ is a lumped hydro-thermal diffusivity, and diffusion of *both* the heat and the pore fluid on the scale

of the wet, shear-heated zone is negligible. (The term *drainage* is used in this paper in relation to *both* the pore fluid and the heat transport, and, thus, the term *undrained* is used in the forthcoming interchangeably with the commonly used "undrained-adiabatic"). Time integration of (6) at $y = 0$, while neglecting the transport terms, and use of (1) lead to the following expressions [*Lachenbruch*, 1980]:

$$t \ll T^* : \Theta(0,t) - \Theta_0 = \frac{p(0,t) - p_0}{\Lambda} = \frac{1}{\rho c h}\int_0^t \tau(t')V(t')dt', \quad (7)$$

where $T^* = h^2/(4\alpha)$ is a hydro-thermal diffusion timescale; and Θ_0 and p_0 are the ambient values of Θ and p. The corresponding fault constitutive relation follows from (3), (7), and the identity $\tau V \equiv \tau_f V$:

$$f\bar{\sigma}_0 - \tau_f(t) = \frac{1}{\delta_c}\int_0^t \tau_f(t')V(t')dt', \quad \left(\delta_c = \frac{\rho c}{f\Lambda}h\right), \quad (8)$$

where δ_c is the characteristic slip weakening distance [*Lachenbruch*, 1980] and $\bar{\sigma}_0 = \sigma - p_0$ is the ambient effective stress.

[19] *Rice* [2006, Table 2, and references therein], based on the study of the Medium Tectonic Line (MTL) fault zone by *Wibberley and Shimamoto* [2003], estimated the hydrothermal properties of the fault gouge within the principal shear zone at the ambient conditions at the mid-seismogenic depth of 7 km: $\rho c = 2.7$ MJ/m^3 K, $\alpha_{th} = 0.7$ mm^2/s, $\alpha_{hy} = 0.86$ to 3.52 mm^2/s, $\Lambda = 0.98$ to 0.34 MPa/°C, where the bounds of the ranges refer to the "intact elastic" and the "highly damaged" fault walls conditions, respectively. For the former case, we note the estimates of the hydrothermal diffusion timescale $T^* \approx (h/(4\text{ mm}))^2$ s and the characteristic slip weakening distance $\delta_c \approx (3/f)h$, which further suggests $T^* \approx$ 0.6 ms to 160 s and $\delta_c \approx 2$ mm to 1 m for shear zone thickness h within the range from 100 μm to 50 mm, and $f \approx$ 0.15. These values are of note, since, as we further find, T^* and δ_c actually scale the slip duration and the total slip, respectively, on a self-healing rupture pulse in the constant friction model as long as the background (driving) stress is not exceedingly small compared to the nominal strength. We further note that *Rice*'s α_{hy}-range corresponds to the low-end value of the gouge permeability, $k \sim 10^{-20}$ m^2, and higher values, by one-to-two orders of magnitude, are not unwarranted [*Faulkner and Rutter*, 2000; *Wibberley and Shimamoto*, 2003; *Noda and Shimamoto*, 2005; *Mizoguchi et al.*, 2008; *Tanikawa and Shimamoto*, 2009]. Under the undrained conditions, $t \ll T^*$, (8) suggests exponentially fast degradation of fault strength over slip distance $\sim\delta_c$. If T^* scales the slip duration, we observe that pulses with average slip rate in excess of $\delta_c/T^* \approx 3$ to 0.006 m/s for the above h-range are likely to result in a near complete loss of the dynamic fault strength.

[20] The *large-time*, *drained shear zone response* is attained if slip at a given location along the fault is sustained long enough, $t \gg T^*$. Under this condition, the shear zone is much thinner than the hydro-thermal boundary layer, suggesting the "slip on a mathematical plane" approximation, $h \to 0$, [*Mase and Smith*, 1987; *Lee and Delaney*, 1987; *Rice*, 2006]:

$$t \gg T^* : \dot{\gamma}(y,t) = V(t)\delta_{Dirac}(y), \quad (9)$$

where $\delta_{Dirac}(y)$ is the Dirac delta function. The temperature change in this problem when a unit rate of shear heating, $\tau(t)V(t)/(\rho c) = 1$, is 'turned on' at $t = 0$ defines the Green's function [*Carslaw and Jaeger*, 1959]

$$G(y,t,\alpha_{th}) = \frac{1}{\sqrt{4\pi\alpha_{th}t}}\exp\left(-\frac{y^2}{4\alpha_{th}t}\right). \quad (10)$$

The general solution can then be obtained by superposition in the form a convolution integral in time with kernel (10) [*Rice*, 2006], the specific form of which for the temperature and pressure changes at $y = 0$ is

$$t \gg T^* : \Theta(0,t) - \Theta_0 = \sqrt{\frac{\alpha}{\alpha_{th}}}\frac{p(0,t) - p_0}{\Lambda} = \frac{1}{\rho c}\int_0^t \frac{\tau(t')V(t')}{\sqrt{4\pi\alpha_{th}(t-t')}}dt'. \quad (11)$$

The corresponding fault constitutive relation can be written as

$$f\bar{\sigma}_0 - \tau_f(t) = \frac{1}{\delta^*}\int_0^t \frac{\tau_f(t')V(t')dt'}{\sqrt{\pi(t-t')/t^*}}, \quad \left(\delta^* = \frac{\rho c}{f\Lambda}\sqrt{4\alpha t^*}\right) \quad (12)$$

where t^* and δ^* are characteristic time and slip, respectively. Similarly to the role of δ_c under the undrained conditions, (8), δ^* provides a measure of the fault slip over which pressurization-induced fault weakening becomes important under the drained shear zone conditions. However, the requisite slip weakening distance δ^* depends on the time t^* over which this slip is accumulated, while δ_c does not. *Rice* [2006] considers a kinematic slip process, in which fault slips indefinitely with constant V and f from the moment of the slip onset. In this case, $t^* = \delta^*/V$, which leads to the expression $\delta^* = (\rho c/f\Lambda)^2(4\alpha/V)$ for the kinematic slip weakening distance (see Rice's L^*). The corresponding analytical solution of (12), $\tau_f = f\bar{\sigma}_0 \exp(\delta/\delta^*)\,\mathrm{erfc}(\sqrt{\delta/\delta^*})$, predicts the progressive fault weakening over all scales of the kinematic slip $\delta = Vt$, both small and large compared to δ^* [*Rice*, 2006], with the infinite rate of weakening attained at the vanishing values of slip. This fault-weakening style is distinctively different from the undrained weakening, with a well-defined slip weakening scale, *Lachenbruch*'s [1980] δ_c. As we will show, it is the latter that represents the slip-weakening in a spontaneous TP rupture pulse.

[21] As opposed to the early- and large- time regimes of fault slip discussed above, the intermediate slip regime, $t \sim T^*$, with a *partially-drained shear zone*, actually depends on a particular distribution of shear across the shear zone with small but finite characteristic thickness h. The solution to diffusion equation (6) in this general case can be expressed as a convolution in both time and space utilizing Green's function (10). Corresponding solution for the temperature and pressure change at $y = 0$ [*Rice*, 2006] can be written for the class of shear distributions (2) as follows

$$\Theta(0,t) - \Theta_0 = \frac{1}{\rho c h}\int_0^t \tau(t')V(t')\mathcal{A}\left(\frac{t-t'}{T_{th}}\right)dt', \quad (13)$$

$$\frac{p(0,t) - p_0}{\Lambda} = \frac{1}{\rho c h}\int_0^t \tau(t')V(t')\mathcal{K}\left(\frac{t-t'}{T^*};\frac{\alpha_{hy}}{\alpha_{th}}\right)dt', \quad (14)$$

where $T_{th} = h^2/(4\alpha_{th})$ and $T^* = h^2/(4\alpha)$ are diffusion time-scales, and the normalized convolution kernels $\mathcal{A}$ and $\mathcal{K}$ are defined in Appendix A, (A1) and (A2). Corresponding expression for the fault constitutive law follows as

$$f\bar{\sigma}_0 - \tau_f(t) = \frac{1}{\delta_c}\int_0^t \tau_f(t')V(t')\mathcal{K}\left(\frac{t-t'}{T^*};\frac{\alpha_{hy}}{\alpha_{th}}\right)dt'. \qquad (15)$$

[22] Evaluation of $\mathcal{K}$ for different shear distributions (e.g., uniform and Gaussian), and different values of the diffusivity ratio α_{hy}/α_{th} shows a maximum 20% variation of $\mathcal{K}$ with each factor. Similarly limited dependence of the slip solutions on these two factors is to be expected. Furthermore, it is not difficult to show based on the definition (A2) and property $\partial\mathcal{A}(\zeta, \chi)/\partial\zeta \geq 0$ established in the Appendix A that the minimum (maximum) value of the diffusivities' ratio, i.e., $\alpha_{hy}/\alpha_{th} = 1$ ($\alpha_{hy}/\alpha_{th} = 0$ or ∞), corresponds to the kernel $\mathcal{K}$'s maximum (minimum), i.e., $\mathcal{K}(\zeta, \{0, \infty\}) \leq \mathcal{K}(\zeta, \chi) \leq \mathcal{K}(\zeta, 1)$ for all $\zeta \geq 0$ and $\chi \geq 0$. Consequently, the $\alpha_{hy} = \alpha_{th}$ case corresponds to the maximum TP effect for a fixed value of the lump diffusivity parameter $\alpha = (\sqrt{\alpha_{th}} + \sqrt{\alpha_{hy}})^2$.

[23] The early-time ((7) and (8)) and large-time ((11) and (12)) asymptotic expressions of the fault response can be recovered from (13)–(15) and the kernels' asymptotics (Appendix A): $\mathcal{A}(0) = \mathcal{K}(0) = 1$ and $\mathcal{A}(\zeta) = \mathcal{K}(\zeta; \cdot) = 1/\sqrt{\pi\zeta}$ when $\zeta \to \infty$.

2.2. Steady-State Elastodynamic Slip Pulse

[24] We consider a spontaneous elastodynamic slip pulse confined to a patch of length L that propagates unilaterally with a constant velocity v_r along a 2-D fault loaded by a uniform background stress τ^b (Figure 1). This type of a self-healing rupture with a steady-state space-time dependence has been previously considered by *Freund* [1979], *Perrin et al.* [1995], *Broberg* [1999], and *Rice et al.* [2005] among others in the context of various slip-weakening strength models. Slip velocity V and shear stress τ on the fault plane are functions of a single variable: the coordinate x in the reference system moving with the rupture tip, or, alternatively, the time $t = x/v_r$ from the onset of slip at a fixed location along the fault. For a sub-sonic anti-plane (Mode III) or in-plane (Mode II) rupture pulse, V and τ are related by the elastodynamic integral equation [*Weertman*, 1980]

$$\tau(x) - \tau^b = \frac{\bar{\mu}}{2\pi v_r}\int_0^L \frac{V(x')dx'}{x'-x}, \quad \text{with} \quad V(x) = v_r\frac{d\delta}{dx}. \qquad (16)$$

Here $\bar{\mu} = \mu\, F(v_r/c_s)$ is an apparent shear modulus which is monotonically decreasing with v_r from the quasi-static value $= \mu$ for mode III and $\mu/(1-\nu)$ for mode II (with ν being Poisson's ratio), to zero when v_r is approaching the shear speed c_s (mode III) or the Rayleigh speed c_R (mode II) [*Kostrov and Nikitin*, 1970; *Rice*, 1980]. Specifically, $F = \sqrt{1-(v_r/c_s)^2}$ for mode III, and a lengthier expression for mode II can be found in the work by *Rice et al.* [2005, equation (11)].

[25] The stress τ is equal (less than) the strength τ_f along the slipping (locked) part of the fault:

$$\tau = \tau_f \quad (x \in [0, L]), \qquad \tau < \tau_f \quad (x \notin [0, L]). \qquad (17)$$

Ahead of the rupture front, $\tau_f(x \leq 0) = f\bar{\sigma}_0$. Behind the rupture front, including both the slipping and locked parts, $\tau_f(x > 0)$ is given by constitutive law (15) or one of its asymptotes.

[26] When no back slip is allowed, differentiation of (16) outside of the slipping patch suggests that $d\tau/dx > 0$ there [e.g., *Perrin et al.*, 1995]. Thus, the stress is rising from the background value τ^b ahead of the rupture up to the strength level τ_0 ($>\tau^b$) at the rupture edge, followed by cumulative weakening over the duration of slip to a certain dynamic stress level τ_L ($<\tau^b$) at the pulse's trailing edge, and rebounding back to τ^b past the trailing edge (Figure 1).

[27] We seek further insight into the stress/strength changes behind the advancing edge of the rupture by differentiating the fault constitutive relation (15) in time ($t > 0$):

$$\frac{d\tau_f}{dt} = \frac{df}{dt}\bar{\sigma}_0 - \frac{1}{\delta_c}\tau_f V - \frac{1}{\delta_c}\int_0^t \tau_f(t')V(t')\mathcal{K}'\left(\frac{t-t'}{T^*};\frac{\alpha_{hy}}{\alpha_{th}}\right)\frac{dt'}{T^*}, \qquad (18)$$

where $\mathcal{K}'(\zeta; \cdot) = \partial\mathcal{K}/\partial\zeta$. The first term in (18) corresponds to the direct effect of the friction change onto the strength change. The rate of τ_f change along the patch, $d\tau_f/dx = (1/v_r)(d\tau_f/dt)$, is always bounded on the assumption of bounded df/dt. The *negative* second term in (18) corresponds to the instantaneous (undrained) fault weakening with the slip. The *positive* third term in (18) (in view of $\mathcal{K}' < 0$, Appendix A) corresponds to the fault strengthening due to the hydro-thermal diffusion from the pressurized and heated shear zone. When changes of f are neglected along the slipping patch (or these changes due to the onset/cessation of slip take place over negligibly small zones near the patch ends), the adiabatic-undrained weakening ($d\tau_f/dx < 0$) dominates the fault response in the immediate vicinity of the rupture edge; while the diffusive strengthening ($d\tau_f/dx > 0$) dominates the response in the vicinity to the trailing edge due to the vanishing 2nd term in (18). We note that non-monotonic character of stress changes along a slipping patch also arises in other physically-motivated models of dynamic fault weakening (e.g., flash-heating on asperities [*Rice*, 2006; *Noda et al.*, 2009]). We show next that it is a prerequisite for intrinsic self-healing of the slip for steadily propagating elastodynamic pulses.

[28] Asymptotic considerations of the elastodynamic equation (16) near the patch edges (Appendix B) show that, in general, the slip velocity vanishes as the square root of the distance from an edge, and the shear stress rate along the locked parts of the fault is singular at the edges. Specifically, at the trailing edge, (B3) gives $V(x) \sim v_r(k_L/\bar{\mu})\sqrt{L-x}$ and $d\tau/dx \sim k_L/(4\sqrt{x-L})$ with k_L given by (B4) when the trailing edge is approached from the slipping and locked sides, respectively. From (18), the strength recovery rate $d\tau_f/dx > 0$ behind the trailing edge can be driven by frictional aging [e.g., *Perrin et al.*, 1995] (if the 1st term in (18) is positive), and/or by pore pressure dissipation (the 3rd term in (18)). Since this rate is *bounded* at $x = L$, the fault healing requires that the rate of stress rebound $d\tau/dx$ there is non-singular, or, according to (B3) and (B4),

$$k_L \equiv -\frac{4}{\pi\sqrt{L}}\int_0^L \sqrt{\frac{x}{L-x}}\frac{d\tau}{dx}dx = 0. \qquad (19)$$

Under this condition, $V(x) \sim (L-x)^{3/2}$ as $x \to L^-$, and $d\tau/dx$ is not only bounded, but is also continuous at the trailing edge, $d\tau/dx = d\tau_f/dx$ at $x = L$. Consequently, locked slip immediately behind the trailing edge now requires

$$d^2\tau/dx^2 < d^2\tau_f/dx^2 \quad \text{as} \quad x \to L^+. \tag{20}$$

It is not difficult to see, by differentiating (B1), that $d^2\tau/dx^2 = -\infty$ as $x \to L^+$. On the other hand, differentiating (18) and using the V-asymptotics with $k_L = 0$ and properties of the kernel $\mathcal{K}$ stated in Appendix A, one can show that $d^2\tau_f/dx^2$ is bounded in the same limit. Thus, condition (20) for locked slip in the immediate vicinity of the trailing edge is satisfied automatically when (19) is. We do not furnish a general proof that (19) is also a sufficient condition for locked slip at finite distances behind the trailing edge, but do observe that it is the case for the self-healing pulse solutions developed in this work.

2.2.1. Physical Relevance of Pulse Solutions With and Without Intrinsic Slip Healing

[29] *Freund* [1979], *Heaton* [1990], *Nielsen and Madariaga* [2003], and *Rice et al.* [2005] among others considered slip-pulse models where no specific physics was included to explicitly model the healing process, or, in fact, validate that the locked slip condition is satisfied behind the rupture pulse. Nevertheless, these solutions have been very useful in studying characteristic features of pulse-like ruptures and related scaling constraints [e.g., *Heaton*, 1990; *Rice et al.*, 2005]. In this paper, we do not aim at accounting for *all* healing mechanisms that may be physically relevant. Notably, we do not explicitly consider the dependence of friction coefficient on the rate and state of slip, which can alone generate self-healing pulses [*Perrin et al.*, 1995; *Rubin and Ampuero*, 2009]. Yet, we account for a slip healing process driven by the pore pressure and temperature diffusion away from the shear zone, which, as we show, does generate the unique self-healing pulse solution for a fixed value of background stress. This solution is the physically relevant one if the model assumption (that of constant sliding friction) is approximately valid, and if the pore pressure diffusion is indeed the dominant slip-healing mechanism. From this perspective, the slip-pulse solutions of our model that do not have the intrinsic slip healing property, i.e., do not satisfy constraint (19), may still be relevant approximations of the solutions to more physically complete models that possess the intrinsic healing feature, and, thus, are not a priori discarded. An example of such "non-healing", but possibly relevant, pulse solution within our model is the undrained-adiabatic pulse.

3. Slip-Pulse Equations for Constant Friction and Method of Solution

[30] We focus on the slip-pulse solutions under the assumption of a constant friction along the slipping part of the fault, $f(x) = f_0$, $x \in (0, L)$. One can rewrite the elasto-dynamic equation (16) in terms of the normalized slip rate V/V_c, slip δ/δ_c, and coordinate x/L as,

$$\frac{L}{L_c}\left(\frac{\tau(x)}{\tau_0} - \frac{\tau^b}{\tau_0}\right) = \frac{1}{2\pi}\int_0^L \frac{V(x')}{V_c}\frac{dx'}{x'-x} \quad \text{with} \quad \frac{V(x)}{V_c} = \frac{d(\delta/\delta_c)}{d(x/L)}. \tag{21}$$

Here L_c and V_c are characteristic values defined by

$$L_c = \frac{\bar{\mu}}{\tau_0}\delta_c \quad (\bar{\mu} = \mu\ F(v_r/c_s)), \qquad V_c = \frac{\delta_c}{T} \tag{22}$$

and $T = L/v_r$ is the slip duration (dislocation rise time). The fault constitutive equation (15) with $f = f_0 = \tau_0/\bar{\sigma}_0$ is:

$$1 - \frac{\tau_f(x)}{\tau_0} = \int_0^x \frac{\tau_f(x')}{\tau_0}\frac{V(x')}{V_c}\mathcal{K}\left(\frac{T}{T^*}\frac{x-x'}{L}; \frac{\alpha_{hy}}{\alpha_{th}}\right)\frac{dx'}{L}, \tag{23}$$

the undrained-adiabatic limit of which is given by the exponential slip-weakening law

$$T \ll T^* : \tau_f(x)/\tau_0 = \exp(-\delta(x)/\delta_c). \tag{24}$$

[31] It is shown in the next section that solution $\delta(x)$ of equations (21)–(23) and (17) in the limit of small ($\delta \ll \delta_c$), undrained ($T \ll T^*$) slip exists only for a specific value of the normalized pulse length L/L_c, and that this solution is unique. We presume by continuity that the unique solution exists for the entire range of problem parameters (although no rigorous proof is furnished here).

[32] The scaling of the governing equations suggests that the solution for the normalized distributions, δ/δ_c, V/V_c, and τ/τ_0 versus x/L, and for the normalized patch length L/L_c are a function of the normalized background loading τ^b/τ_0, pulse duration T/T^*, and the diffusivity ratio α_{hy}/α_{th}. In other words, for a given loading τ^b/τ_0 of a fault with fixed α_{hy}/α_{th}, there exist a multitude of pulse solutions with different rupture velocity v_r parameterized by the pulse duration T/T^*. It is an additional physical constraint, such as the intrinsic slip healing property, (19), that would allow the fault to select a unique slip-pulse solution.

[33] Once the slip solution of (21) and (23) is known, the normalized pressure and temperature perturbations on the fault can be calculated from

$$\frac{p(x) - p_0}{\bar{\sigma}_0} = 1 - \frac{\tau_f(x)}{\tau_0}, \tag{25}$$

$$\frac{\Theta(x) - \Theta_0}{\bar{\sigma}_0/\Lambda} = \int_0^x \frac{\tau_f(x')}{\tau_0}\frac{V(x')}{V_c}\mathcal{A}\left(\frac{T}{T_{th}}\frac{x-x'}{L}\right)\frac{dx'}{L}, \tag{26}$$

respectively. (Here (26) is a normalized form of (13)). In the undrained limit, $\tau_f(x)$ is given by (24), and the normalized pressure/temperature perturbations (25) and (26) are identical.

[34] In the following sections 4–6, we discuss details of various numerical and analytical slip-pulse solutions. The numerical approach relies on the expansion of the slip-rate distribution into the series of Chebyshev polynomials with appropriate asymptotics (B3) at the rupture ends; which then allows the evaluation of the elasticity equation (21) for the corresponding stress series expansion. Using the slip-rate and the stress expansions to evaluate the constitutive law (23) at a number of collocation points along the patch allows us to solve for the expansion coefficients and the normalized length of the patch. Appendix D presents the details of the method and its specializations to the various limiting cases of interest here.

[35] Section 4 considers a small-slip solution, when the fault is stressed almost to its maximum strength ($\tau_0 - \tau^b \ll \tau_0$), as a function of the normalized slip-pulse duration T/T^*. It is in this limiting case of the fault loading, we show for the first time that a slip-pulse solution exists in a finite range of pulse duration, $0 \le T/T^* \le (T/T^*)_{\text{s.h.}}$, where the lower and upper bounds correspond to the undrained and the partially-drained, *self-healing* slip solutions, respectively. Existence of the upper bound implies the nonexistence of a steady slip pulse on a plane (i.e., pulse with a drained shear zone, $T/T^* \gg 1$) in the model with a constant friction along the slipping patch. The results for the two bounding solutions are presented in section 5 for a range of the background stress. Section 6 follows with a detailed investigation of the large slip limit of these solutions when the background stress is low compared to the maximum fault strength ($\tau^b \ll \tau_0$).

[36] The numerical solutions for a partially-drained slip pulse assume a Gaussian shear distribution across the fault zone.

4. Small Slip Pulse ($\tau_0 - \tau^b \ll \tau_0$)

[37] When the background shear stress is close to the maximum fault strength, $\tau_0 - \tau^b \ll \tau_0$, the fault weakening during a slip event is expected to be small. This suggests that the corresponding slip and its rate are also small. Consequently, the constitutive law (23) can be linearized by replacing the shear heating rate $\tau_f V$ with $\tau_0 V$ under the integral.

4.1. Undrained-Adiabatic Limit ($T \ll T^*$)

[38] In this limit, the slip-weakening law (24) reduces to $\tau_f(x)/\tau_0 \simeq 1 - \delta(x)/\delta_c$. Using the latter to evaluate (21) along the patch ($\tau = \tau_f$), and dividing the result by a small parameter $\epsilon \equiv (\tau_0 - \tau^b)/\tau_0 \ll 1$, we obtain a linear integral equation

$$\frac{L}{L_c}\left(1 - \frac{\delta(x)}{\epsilon \delta_c}\right) = \frac{1}{2\pi}\int_0^L \frac{V(x')}{\epsilon V_c}\frac{dx'}{x' - x}. \tag{27}$$

This confirms that the slip and slip rate are small, $O(\epsilon)$ fractions of the characteristic values δ_c and V_c, respectively. It is shown in Appendix C that the solution of (27) for patch length L and slip rate $V(x)$ is unique, and is mathematically related to the solution of auxiliary eigen problem considered by *Uenishi and Rice* [2003]. This solution is given by $L \simeq 1.158\, L_c$ and the distributions of the slip rate, slip, and stress shown in Figure 4 (marked by $T/T^* = 0$). $V(x)$ is symmetric with respect to the center of the patch, $x = L/2$. This, in turn, corresponds to the antisymmetry of $1 - \delta(x)/(\epsilon\delta_c)$ and $\tau - \tau^b$, and suggests the exact expressions for the total slip and the dynamic stress drop, respectively:

$$\delta_L = 2\left(1 - \frac{\tau^b}{\tau_0}\right)\delta_c, \quad \tau^b - \tau_L = \tau_0 - \tau^b. \tag{28}$$

4.2. General Case

[39] The normalized length of the slipping patch and the total accumulated slip are shown in Figure 3 for two bounding values of the diffusion ratio, $\alpha_{\text{hy}}/\alpha_{\text{th}} = 1$ (black lines) and $\alpha_{\text{hy}}/\alpha_{\text{th}} = 0$ (gray lines), respectively. (Note, that due to the symmetry of the kernel in (23), $\mathcal{K}(\cdot, \chi) = \mathcal{K}(\cdot, 1/\chi)$ where $\chi = \alpha_{\text{hy}}/\alpha_{\text{th}}$, the normalized solution with $\alpha_{\text{hy}}/\alpha_{\text{th}} = \infty$ is identical to the one with $\alpha_{\text{hy}}/\alpha_{\text{th}} = 0$). Figure 3 shows that the maximum variation of the small-slip solution with the diffusivities' ratio is about 20%, which is in-line with the extent of the kernel $\mathcal{K}$ dependence on $\alpha_{\text{hy}}/\alpha_{\text{th}}$. Larger contrast between the thermal and hydraulic diffusivities within the fault zone results in somewhat larger slip accommodated on a larger slipping patch over a shorter slip duration (i.e., at higher overall slip velocity).

[40] The solution's lower bound corresponds to the undrained solution discussed above, while the partially-drained, *self-healing* pulse corresponds to the maximum slip duration, which is a finite multiple of the characteristic diffusion time: $T_{\text{s.h.}} \simeq 2.536\, T^*$ for $\alpha_{\text{hy}}/\alpha_{\text{th}} = 1$ and $2.047\, T^*$ for $\alpha_{\text{hy}}/\alpha_{\text{th}} = \{0, \infty\}$. Attempted solutions with $T > T_{\text{s.h.}}$ result in a non-physical backslip near the trailing edge of the rupture. Consequently, the slip pulse on a plane when $T \gg T^*$ does not exist in the model with a constant fault friction. A general proof of this conjecture not limited by the small slip assumption and is given in Appendix E.

[41] Distributions of the slip velocity, slip, and stress in the pulse solution for $\alpha_{\text{hy}}/\alpha_{\text{th}} = 1$ are shown in Figure 4 for various values of the normalized pulse duration. We observe that higher values of the maximum slip rate are achieved closer to the advancing edge of the rupture with the increasing drainage of the shear zone, i.e., increasing normalized slip duration T/T^*, while slip rates slower than in the undrained solution are predicted closer to the trailing edge (Figure 4a). This results in higher initial rates of fault weakening for higher values of T/T^*, which changes to strengthening as the trailing edge is approached (Figure 4c) and diffusion overcomes the diminished effect of shear heating (due to diminished shear stress), resulting in pore pressure dissipation. This is consistent with the observed maximum temperature that is reached at intermediate distance along the patch (Figure 4d), and, consequently, does not correspond to the maximum level of accumulated slip (reached at the trailing edge).

5. General Slip-Pulse Solution

[42] As seen from the analysis of a small-slip pulse, the solution is bounded by the (i) undrained solution, and (ii) partially-drained, self-healing slip solution, that correspond to the minimum and the maximum slip duration, respectively. The minimum (undrained slip) duration is undetermined within the model of a fault with a constant friction, other than that it is small compared to the diffusion timescale T^*. The maximum (self-healing slip) duration is a multiple of T^*, the value of which is defined as a function of the background stress normalized by the nominal strength. General results pertaining to the normalized form of the two bounding solutions as a function of τ^b/τ_0 are presented next.

5.1. Normalized Slip, Slip Duration, and Pulse Size

[43] Figure 5 shows the normalized slip duration T/T^* (Figure 5a), length of the slipping patch L/L_c (Figure 5b), and total slip δ_L/δ_c (Figure 5c). We observe that the slip duration in the self-healing pulse indeed scales with the hydrothermal diffusion timescale T^* when background

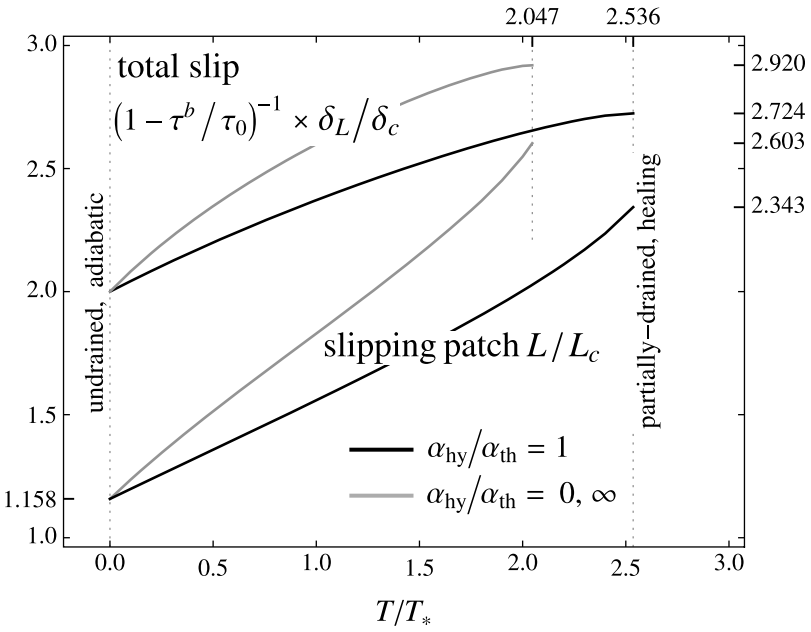

Figure 3. Small slip solution: normalized slipping patch and total slip versus normalized slip duration. Black and gray lines correspond to $\alpha_{hy}/\alpha_{th} = 1$ and $\alpha_{hy}/\alpha_{th} = 0, \infty$, respectively.

stress is a moderate fraction of the strength. This scaling breaks down for small values of τ^b/τ_0, when T/T^* becomes very small while the total accumulated slip δ_L/δ_c (Figure 5c) large, in what is further referred to as the large-slip solution. The corresponding large-slip asymptotic solution is developed in section 6, and is given, in the first approximation, by the undrained solution characterized by diverging normalized slip $\delta_L/\delta_c \approx (\tau^b/\tau_0)^{-1}$ and normalized patch size $L/L_c \approx (\pi\tau^b/\tau_0)^{-2}$, and, for the self-healing pulse, vanishing slip duration $T/T^* \propto (\tau^b/\tau_0)^{2/3}$ (where the coefficient of proportionality is $O(1)$). In the other limit, when the background stress is large, $\tau^b/\tau_0 \approx 1$, the solutions approach the small-slip asymptotic solution (section 4), which corresponds to the maximum slip duration and the minimum (but finite) patch size and the vanishing slip. The effect of the diffusivities' ratio, as discussed above for the small-slip limit, is to diminish the slip duration and increase the patch size and the slip.

[44] As already anticipated from the small-slip solution (section 4), more slip is accumulated in a partially-drained pulse than in the undrained one at the same background stress level (Figure 5c). A similar observation can be made regarding the size of the patch over which this slip is accumulated. Although, the rupture velocity is indeterminate in the undrained solution (due to the indeterminacy of the corresponding slip duration), it should be higher than that of the partially-drained pulse (see section 7.1), which therefore would result in smaller values of the characteristic length $L_c = (\mu\delta_c/\tau_0)F(v_r)$, (22), for the undrained pulse. Consequently, $(L/L_c)^{\text{part.dr.}} > (L/L_c)^{\text{und}}$ (Figure 5b) implies the same inequality for L.

5.2. Development of Slip, Stress, Pore Pressure, and Temperature in the Pulse

[45] Profiles of the normalized slip rate $(1-\tau^b/\tau_0)^{-1}\, V/V_c$ (a–b), slip $(1-\tau^b/\tau_0)^{-1}\,\delta/\delta_c$ (c–d), shear stress τ/τ_0 and strength τ_f/τ_0 (e–f), and the temperature rise $(\Theta-\Theta_0)/(\bar{\sigma}_0/\Lambda)$ (g–h) along the fault plane in the undrained pulse and the partially-drained, self-healing pulse with $\alpha_{hy}/\alpha_{th} = 1$ are shown in Figure 6 for various values of the normalized background stress τ^b/τ_0. The self-healing pulse solution with $\alpha_{hy}/\alpha_{th} = 0, \infty$ is shown in Figure S2 in the auxiliary material.[1]

[46] We first acknowledge the similarity of the undrained pulse (left) and partially-drained, self-healing pulse (right) solutions, which underscores the fact that the solutions are identical in the vicinity of the advancing rupture front, where response is essentially undrained. The differences in the two solutions develop further away from the advancing front where the falling efficiency of the thermal pressurization (with decreasing shear stress) is overcome by the fluid and heat exchange with the fault surroundings in the latter case. This similarity is manifested in distributions of slip (Figures 6c and 6d) and of the rate of slip accumulation along the normalized length of the patch (Figures 6a and 6b) in the two solutions, with somewhat larger values in the partially-drained case.

[47] Note that the characteristic slip rate V_c that is used to scale V is defined in terms of the slip duration, $V_c = \delta_c/T$, and, therefore, varies with the background stress in the partially-drained pulse solution, and is indeterminate in the undrained pulse solution. Since the slip in the undrained pulse develops over much shorter times and distances than in the partially-drained one, the absolute value of the slip rate would have to be much higher for those pulses.

[48] Both pulse solutions predict asymmetric slip rate distributions characterized by very high normalized rates near the advancing tip when the background stress is small. This localization of the slip rate can be further gauged from

[1] Auxiliary materials are available in the HTML. doi:10.1029/2011JB008889.

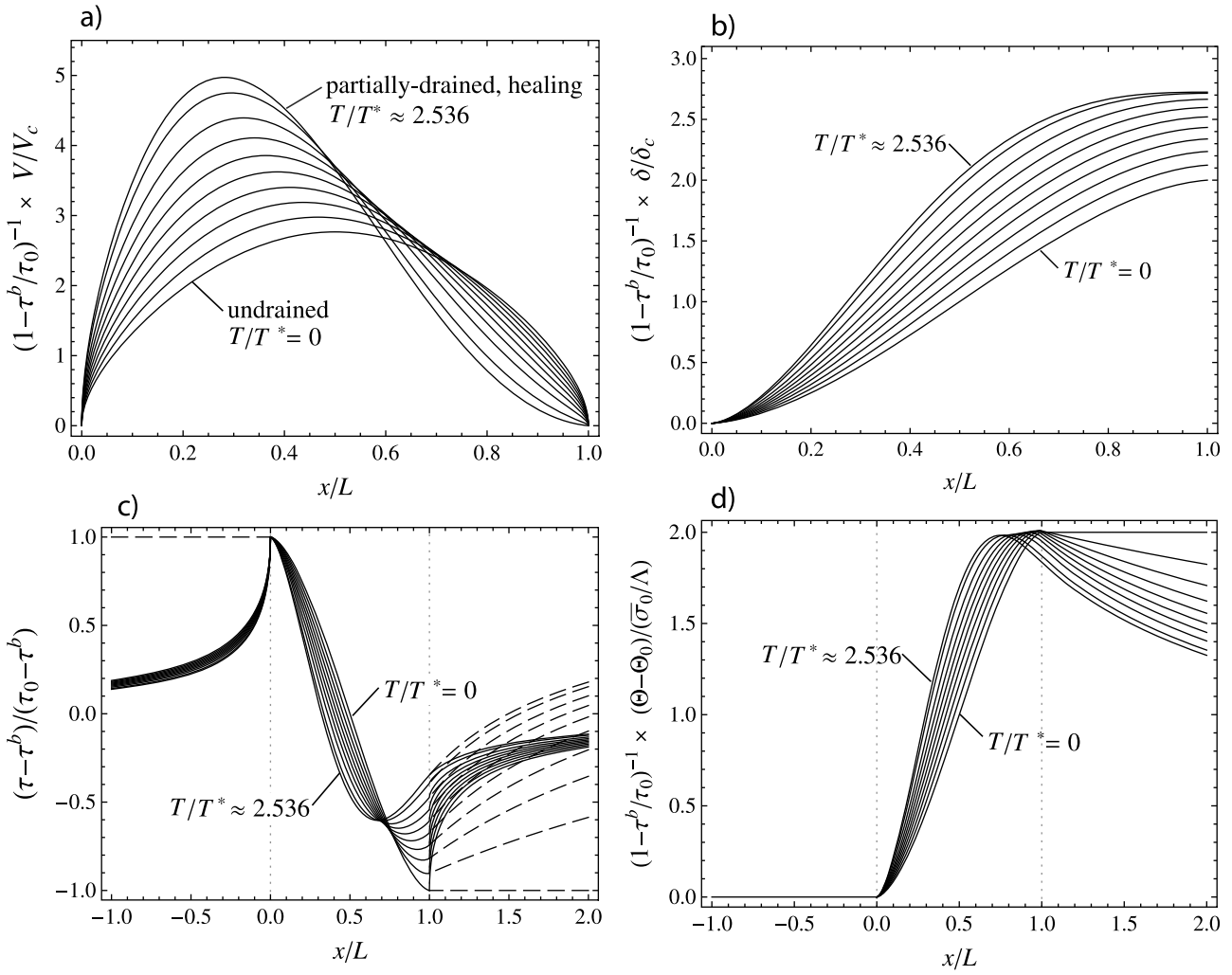

Figure 4. Small slip solution with $\alpha_{hy} = \alpha_{th}$: profiles of the (a) normalized slip velocity, (b) slip, (c) deviation of the stress from the background level, and (d) temperature rise for various values of the slip duration, $T/T_* = \{0, 0.3, 0.6, \ldots, 2.4, 2.5357\}$. (Slip and slip velocity are shown within the slipping patch only.)

the contrast between the maximum V_{max} and the average $\langle V \rangle = \delta_L/T$ values of the slip rate, which can be estimated based on the asymptotic solution of section 6 as $V_{max}/\langle V \rangle \approx 0.1376\ (\tau^b/\tau_0)^{-1}$ for $\tau^b \ll \tau_0$ in the entire range of drainage conditions (from the undrained to the partially-drained, self-healing).

[49] Evolution of the stress/strength along the slipping patch is characterized by the initial undrained weakening, followed, in the case of the partially-drained pulse, by the partial strengthening. In the latter case, the distance behind the advancing edge of the pulse (L_{break}) and the slip value (δ_{break}) corresponding to the minimum dynamic stress (τ_{break}) (see also Figure 1) are shown in Figures 5b and 5c, respectively, by dotted lines. As discussed earlier, it is the partial restrengthening of the fault in a partially-drained pulse that allows for the healing of slip in its wake ($x/L > 1$ in Figure 6f), as manifested by faster recovery of the strength (long-dashed line) than that of the stress (solid line). The extent of the fault dynamic weakening is moderated by the ratio of the driving stress to the nominal strength, such that more weakening is required to drive a pulse at a lower background stress, and near complete dynamic loss of fault traction is observed for $\tau^b/\tau_0 \lesssim 0.1$.

[50] Evolution of the normalized pore fluid pressure is the mirror image of that of the normalized stress, (25), i.e., the fault weakening corresponds to the fluid pressurization, and the fault restrengthening to the decreasing pore pressure due to the diffusive transport away from the fault. The normalized temperature rise develops similarly to that of the pore pressure (Figures 6g and 6h), and exactly so when $\alpha_{hy}/\alpha_{th} = 0$. For $\alpha_{hy}/\alpha_{th} > 0$, the heat diffusion "lags behind" that of the pore pressure, such that, for example, the onset of the cooling in a partially-drained, self-healing pulse takes place after the onset of the depressurization (the fault restrengthening), see Figures 6f and 6h for $\alpha_{hy}/\alpha_{th} = 1$, and Figure S3 in the auxiliary material for other values of the diffusivity ratio.

[51] The peak temperature rise along the pulse, $\Theta_{peak} - \Theta_0$, takes place at the peak (intermediate) value of the slip for the undrained (partially-drained) pulse. $\Theta_{peak} - \Theta_0$ is seen to increase with decreasing magnitude of the background stress up to the maximum value closely

approximated by $\bar{\sigma}_0/\Lambda$. More detailed investigation (see Figure S4 in the auxiliary material) actually shows that the maximum magnitude of the peak temperature rise corresponds to a small, but finite value of τ^b/τ_0, and which increases slightly with the diffusivity ratio: $(\frac{\tau^b}{\tau_0}, \frac{\Theta_{peak}-\Theta_0}{\bar{\sigma}_0/\Lambda}) \approx$ (0, 1), (0.08, 1.021), and (0.26, 1.129) for α_{hy}/α_{th} = 0, 1, and ∞, respectively.

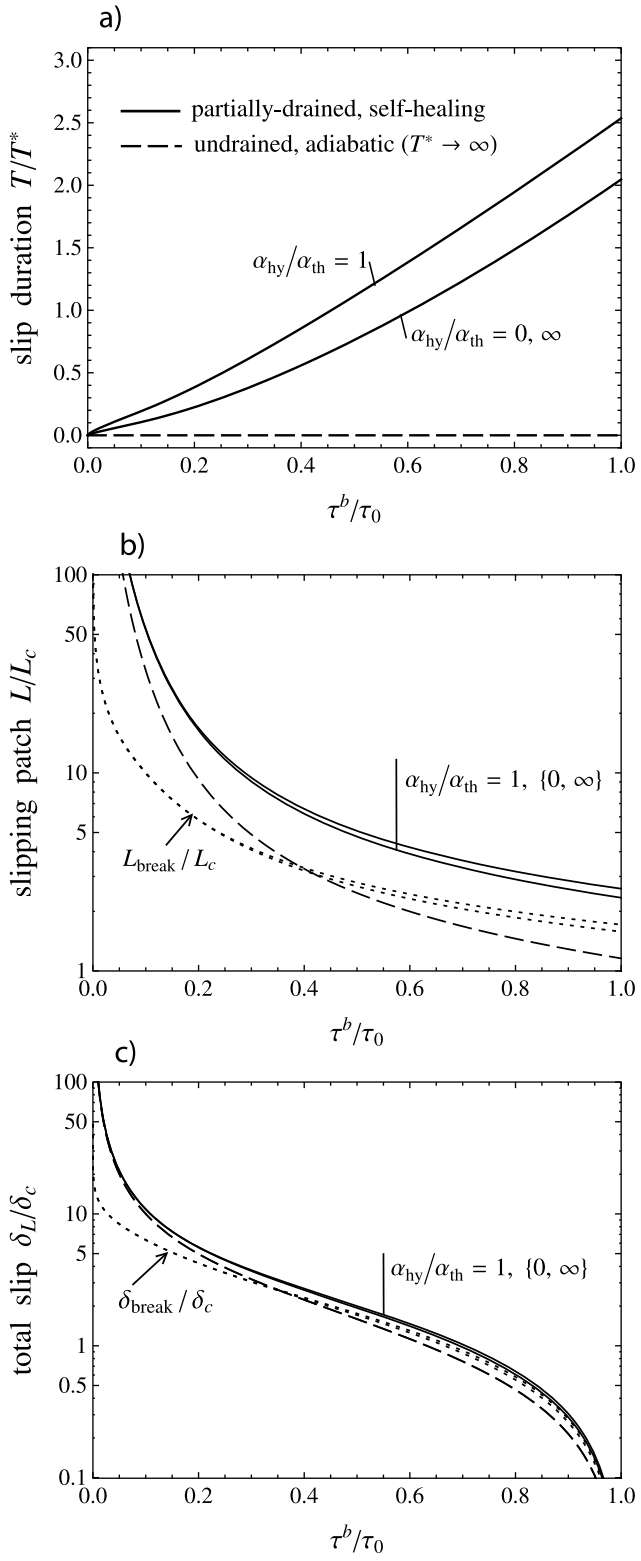

5.3. Fracture Energy

[52] For continuous fault slip-weakening (e.g., the undrained pulse, Figure 6e), the fracture energy can be estimated as the area under the τ versus δ curve and above the minimum dynamic stress line, $\tau = \tau_L$ [*Ida*, 1972; *Palmer and Rice*, 1973]. In this case, the fracture energy can be simply expressed as the product of the dynamic stress drop and the total slip, $G = (\tau^b - \tau_L)\delta_L$. The normalized stress drop and fracture energy of the undrained slip pulse are shown in Figures 7a and 7b, respectively, by dashed lines. G varies between the maximum value $\tau_0\delta_c$ corresponding to the vanishing background stress $\tau^b \ll \tau_0$ (based on the complete dynamic loss of the fault strength) and the minimum value 2 $(1 - \tau^b/\tau_0)^2\,\tau_0\delta_c$ when $\tau^b \approx \tau_0$, (28).

[53] In a more general case, when the initial slip-weakening response may be followed by slip-strengthening (such as the case of the partially-drained, self-healing pulse, Figure 6f), the definition of fracture energy can be generalized, following *Tinti et al.* [2005] (using their "breakdown work W_b"),

$$G = \int_0^{L_{break}} (\tau - \tau_{break}) V\, dx \qquad (29)$$

where, as before, L_{break} = distance from the rupture edge where the stress is at its minimum dynamic value τ_{break} (Figure 1). The stress drop and fracture energy of the self-healing slip pulse are shown in Figures 7a and 7b, respectively, by solid lines. It is interesting to point out that the fracture energy of the self-healing pulse can be closely approximated by the classical formulae (dynamic stress drop $\times$ slip), if understood in terms of the maximum values incurred during the pulse, i.e., $G \approx (\tau^b - \tau_{break})\delta_L$, see the corresponding dotted line in Figure 7b.

[54] *Rice et al.* [2005] furnished the analytical solution to the model of a steady pulse driven by a prescribed, linear stress drop with the distance from the advancing tip, down to a certain residual dynamic level. They have used this solution to constrain the fracture energy scaling with the pulse parameters: $1/\pi \le G/(\bar{\mu}\delta_L^2/L) \le 2/\pi$, where the lower bound corresponds to the instantaneous dynamic stress drop (at the advancing tip) and the upper bound corresponds to gradual weakening over the entire pulse length. Our solutions for the spontaneous TP slip pulses land further support to this scaling: Figure 8 shows that *Rice et al.*'s lower bound for the scaled fracture energy $(1/\pi)$ is recovered from our solutions in the large slip limit ($\tau^b \ll \tau_0$), while the upper bounds in

Figure 5. (a) Scaled slip duration, (b) slipping patch, and (c) total slip versus background stress in the undrained pulse solution (dashed) and the partially-drained, self-healing pulse solutions (solid) with α_{hy}/α_{th} = 1 and {0, ∞}, respectively. Slip duration T is undetermined in the undrained solution, while T/T^* = 0 since $T^* \to \infty$ in this limit. Dotted lines in Figures 5b and 5c correspond to the scaled distance from the rupture edge and the slip value, respectively, when the stress is at its minimum $\tau = \tau_{break}$ in the partially-drained, self-healing pulse. The top and bottom curves in the sets of solid and dotted lines in Figures 5b and 5c correspond to α_{hy}/α_{th} = 1 and {0, ∞}, respectively.

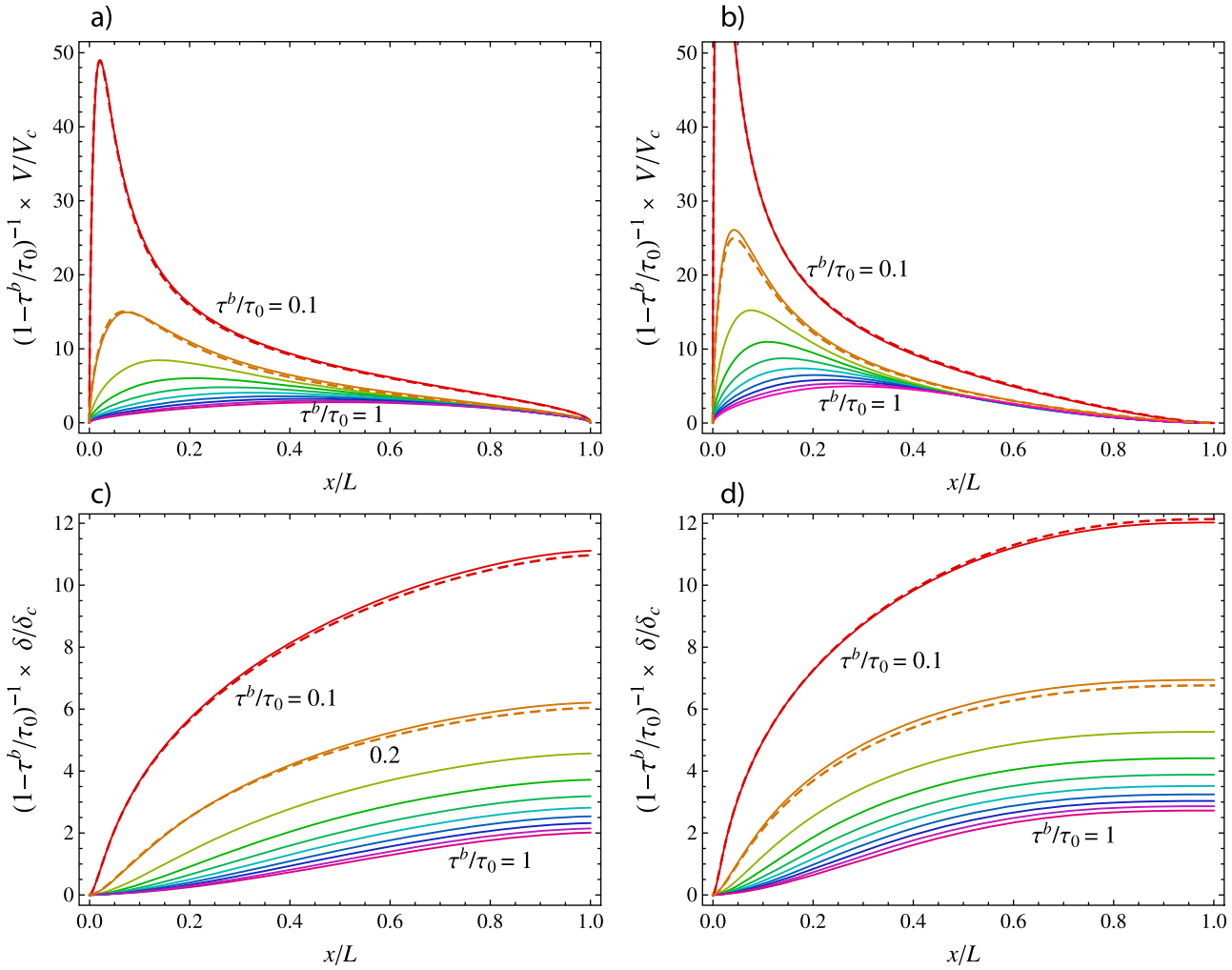

Figure 6. Profiles of (a and b) normalized slip velocity, (c and d) slip, (e and f) stress and strength (long-dash lines), and (g and h) temperature rise in the undrained pulse (Figures 6a, 6c, 6e, and 6g) and the partially-drained, self-healing pulse with $\alpha_{hy} = \alpha_{th}$ (Figures 6b, 6d, 6f, and 6h) for various values of the background stress, $\tau^b/\tau_0 = \{0.1, 0.2, \ldots, 1\}$. Small-slip asymptotic solutions correspond to $\tau^b/\tau_0 = 1$. Large-slip asymptotic solutions are shown by short-dash lines for $\tau^b/\tau_0 = 0.1, 0.2$.

our solutions are attained in the small slip limit ($\tau^b \approx \tau_0$), and are somewhat smaller than $2/\pi$. The stress drop in a spontaneous slip-pulse solution (like the ones considered in this work) develops in response to a particular fault constitutive response, and is usually nonlinear with the distance along the pulse. Details of this spatial distribution (i) are inconsequential when the drop is localized to a vicinity of the advancing tip (thus, the exact agreement of the lower bound values of the scaled fracture energy), and (ii) do matter when the drop is distributed along the pulse (thus, differing values for the upper bound).

[55] Finally, we note that the fracture energy of the partially-drained, self-healing TP pulses depends ever so slightly on the diffusivity ratio α_{hy}/α_{th} to be noticeable in Figure 7b: maximum variation (≈3%) takes place in the small slip limit, where the asymptotic solution gives $(1 - \tau^b/\tau_0)^{-2}(G/\tau_0\delta_c) \approx 1.635$ and 1.69 for $\alpha_{hy}/\alpha_{th} = 1$ and $\{0, \infty\}$, respectively. When scaled with the slip and the patch length (Figure 8), the fracture energy is independent of α_{hy}/α_{th} to the precision of the numerical solution.

6. Large Slip Pulse ($\tau^b \ll \tau_0$)

6.1. Undrained-Adiabatic Boundary Layer at the Advancing Tip

[56] When the background stress is small compared to the nominal strength ($\tau^b \ll \tau_0$), the dynamic stress drop is complete and the corresponding fast slip growth and shear strength reduction are mostly confined to a boundary layer (BL) near the advancing tip of the rupture. The BL approximation corresponds to the problem of a semi-infinite rupture ($L/L_c \to \infty$) driven by vanishing background stress ($\tau^b/\tau_0 \to 0$). Corresponding asymptotic form of the elastodynamic equation (16) is

$$\frac{\tau^{BL}(x)}{\tau_0} = \frac{1}{2\pi}\int_0^\infty \frac{V^{BL}(x')}{(\tau_0/\bar{\mu})v_r}\frac{dx'}{x'-x}, \qquad (30)$$

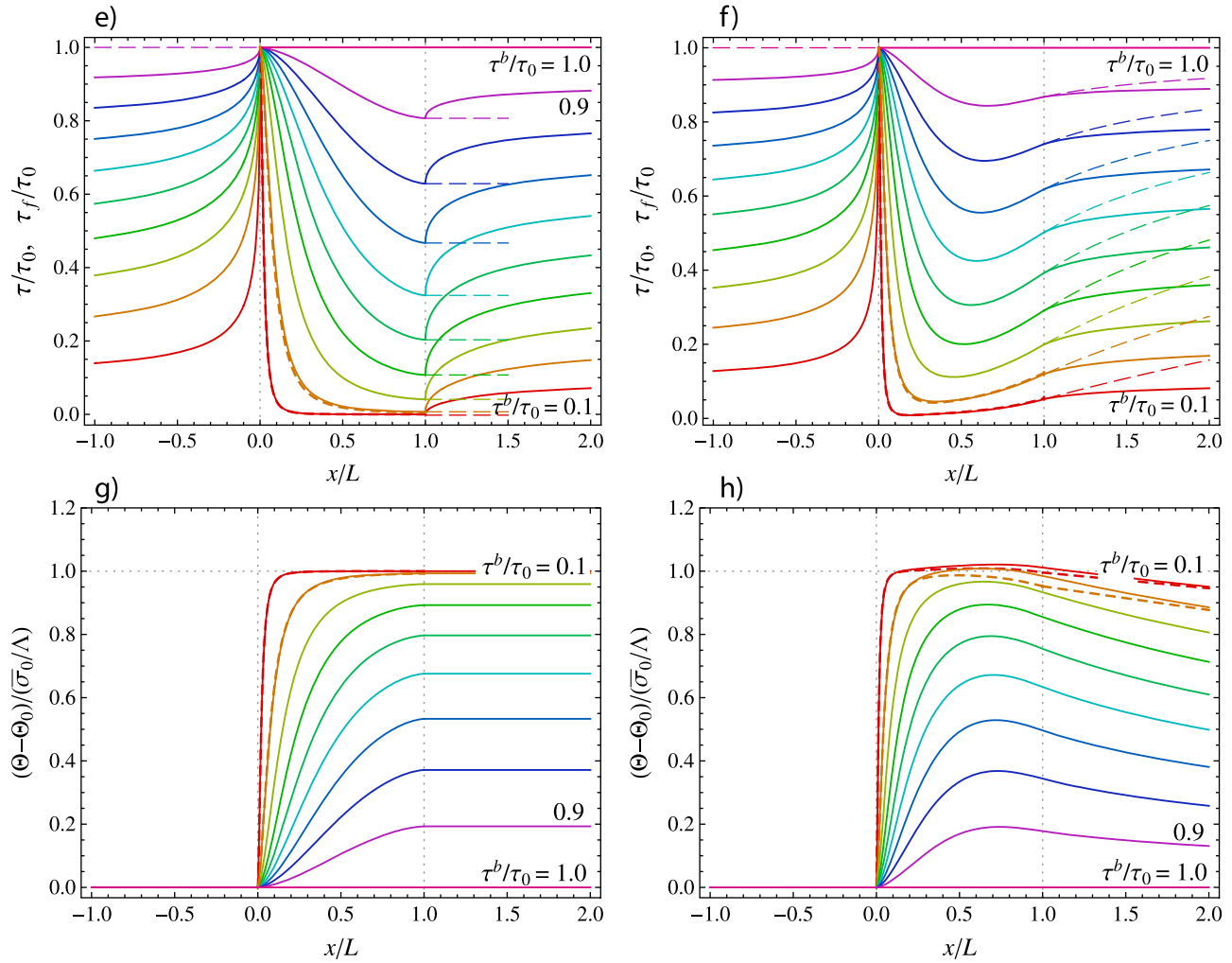

Figure 6. (continued)

where the superscript refers to the BL approximation. The normalized relation between the slip and the slip rate, 2nd in (21), can be rewritten in the scaling suggested by (30) as

$$\frac{V^{\mathrm{BL}}(x)}{(\tau_0/\bar{\mu})v_r} = \frac{d\left(\delta^{\mathrm{BL}}/\delta_c\right)}{d(x/L_c)}. \tag{31}$$

Scaling of equations (30)–(31) together with the undrained law (24) suggests that the normalized field variables

$$\tilde{V} = \frac{V^{\mathrm{BL}}}{(\tau_0/\bar{\mu})v_r}, \quad \tilde{\delta} = \frac{\delta^{\mathrm{BL}}}{\delta_c}, \quad \tilde{\tau} = \frac{\tau^{\mathrm{BL}}}{\tau_0} \tag{32}$$

are of order unity within the BL with the spatial scale $x \sim L_c$.

[57] Vanishing shear strength outside of the crack tip boundary layer ($x \gg L_c$) leads to the condition characterized in fracture mechanics as the "small scale yielding" [*Rice*, 1968]. It states that the slip outside of the immediate vicinity of the rupture front ($x \gg L_c$) can be described by the classical inverse square root singularity solution, $\delta^{\mathrm{BL}} = (K/\bar{\mu})\sqrt{8x/\pi}$, where $K = \sqrt{2\bar{\mu}G}$ is the stress intensity factor required to propagate the crack. Upon evaluating the fracture energy based on the undrained constitutive law (24) and the assumption of large slip resulting in the complete loss of strength, $G = \int_0^\infty \tau_f d\delta = \tau_0\delta_c$, one can express the far field asymptotics for the slip and slip rate, (31), as

$$x \gg L_c : \frac{\delta^{\mathrm{BL}}}{\delta_c} = \frac{4}{\sqrt{\pi}}\sqrt{\frac{x}{L_c}}, \qquad \frac{V^{\mathrm{BL}}}{(\tau_0/\bar{\mu})v_r} = \frac{2}{\sqrt{\pi}}\sqrt{\frac{L_c}{x}}. \tag{33}$$

[58] The BL solution for the normalized slip rate, slip, and stress, (32), as a function of the normalized coordinate $\tilde{x} = x/L_c$, is obtained in section F1 and shown in Figure 9. Dashed lines represent asymptotic behavior of the slip rate in the near field, $\tilde{V} = 1.848\sqrt{x/L_c}$ ($x \ll L_c$), and the far field, $\tilde{V} = 2\sqrt{L_c/\pi x}$ ($x \gg L_c$). The corresponding far field slip asymptote $\tilde{\delta} \simeq 4\sqrt{x/\pi L_c}$ suggests that $\tilde{\delta}$ is large when $x \gg L_c$, and the normalized stress $\tilde{\tau} = \exp(-\tilde{\delta})$, (24) with (32), is exponentially small outside of the tip boundary layer of thickness L_c.

[59] An important implication of this boundary layer solution is that the details of the fast, large slip rate changes near the advancing tip ($x \sim L_c$) of a large-slip rupture operating at small background stress can be simply modeled by

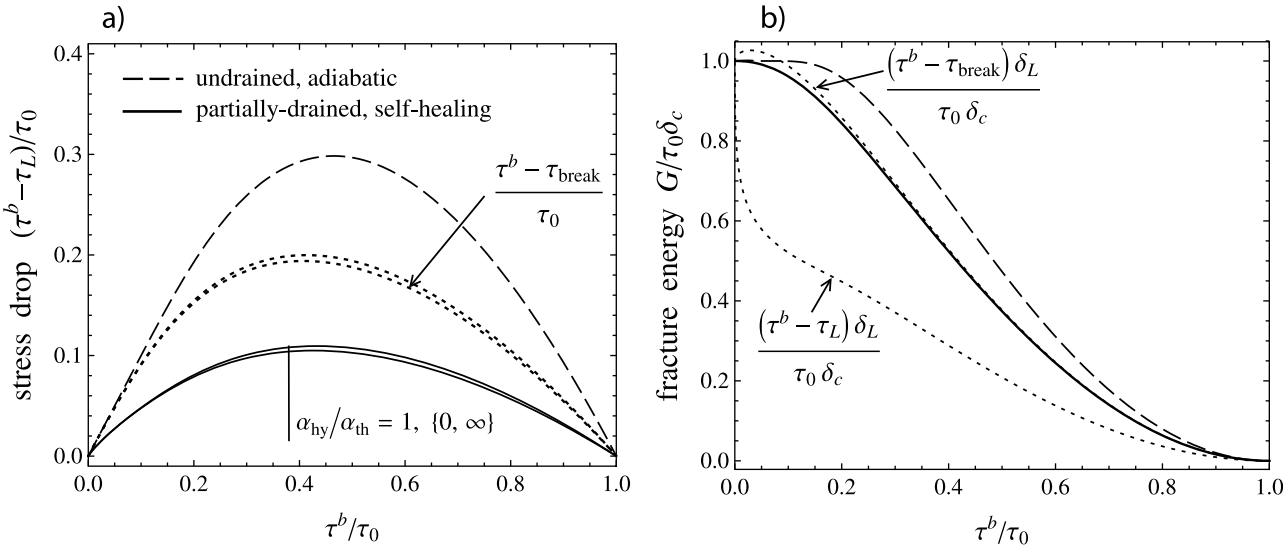

Figure 7. (a) Normalized dynamic stress drop at the trailing edge $(\tau^b - \tau_L)/\tau_0$ and (b) normalized fracture energy $G/\tau_0\delta_c$ versus background stress in the undrained pulse solution and the partially-drained, self-healing pulse solutions with $\alpha_{\rm hy}/\alpha_{\rm th} = 1$ and $\{0, \infty\}$. Dotted lines in Figure 7a show the maximum value of the normalized dynamic stress drop along the slipping patch, $(\tau^b - \tau_{break})/\tau_0$, in the partially-drained solutions. Dotted lines in Figure 7b show normalized quantities related to the fracture energy, as defined in the graph. The fracture energy parameters of the partially-drained solutions plotted in Figure 7b are approximately independent of $\alpha_{\rm hy}/\alpha_{\rm th}$.

the inverse square root singularity (33) on the scale of the rupture ($x \sim L \gg L_c$). Two such solutions corresponding to a large-slip rupture pulse under the undrained conditions and the partially-drained, self-healing slip conditions, respectively, are discussed next.

6.2. Undrained-Adiabatic Large-Slip Solution

[60] According to section B3, the slip rate and shear stress distributions along the finite rupture pulse characterized by the complete stress drop localized to the tip boundary layer is simply given by the BL solution multiplied by $\sqrt{1 - x/L}$, (B9). This correction factor is irrelevant for the stress, which is exponentially small outside of the boundary layer. For the slip velocity, in view of the scaling identity $(L/L_c)V_c = (\tau_0/\bar{\mu})v_r$, we have

$$\frac{V}{V_c} = \frac{L}{L_c}\sqrt{1 - \frac{x}{L}}\,\tilde{V}\left(\frac{x}{L_c}\right) \tag{34}$$

where $\tilde{V}(x/L_c)$ is given in Figure 9a. (The slip distribution follows by integration). The solution outside of the boundary layer (outer solution) follows from (34) with (33),

$$L_c \ll x \le L : \frac{V}{V_c} = \frac{2}{\sqrt{\pi}}\sqrt{\frac{L}{L_c}}\sqrt{\frac{L - x}{x}} \tag{35}$$

A useful analytical scaling of the background stress and the total slip with the pulse size in the large-slip, undrained solution

$$\frac{1}{\tau^b/\tau_0} = \sqrt{\pi\frac{L}{L_c}} = \frac{\delta_L}{\delta_c} \tag{36}$$

is recovered from (B11), $\tau^b/\tau_0 = 0.5\tilde{V}(L/L_c)$, evaluated using the far filed asymptote of $\tilde{V}(\tilde{x})$, and from the integration of (35), respectively.

6.3. Partially-Drained, Large-Slip Solution

[61] As seen from the asymptotic and numerical solutions for the undrained pulse with $\tau^b \ll \tau_0$, the large, rapid slip within the boundary layer at the advancing rupture tip produces a near complete loss of the fault strength (see, e.g., the stress profile for $\tau^b/\tau_0 = 0.1$ in Figure 6e), and the loss of the shear heating power. As the result of the diminished TP rate, the pore fluid and/or heat drainage (when allowed for) is

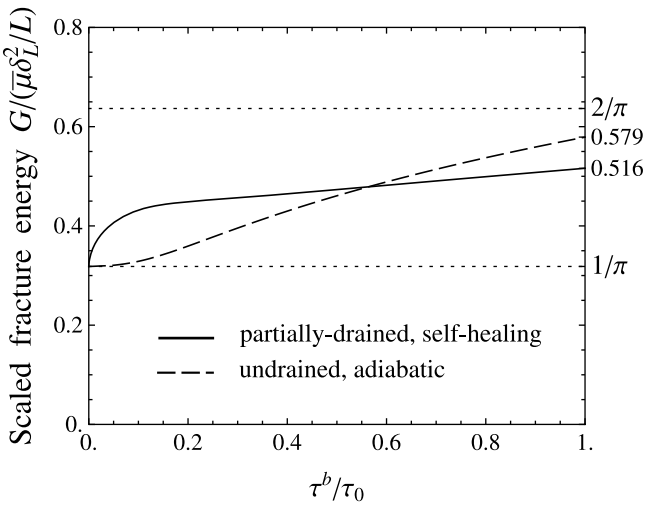

Figure 8. Scaled fracture energy $G/(\bar{\mu}\,\delta_L^2/L)$ versus background stress.

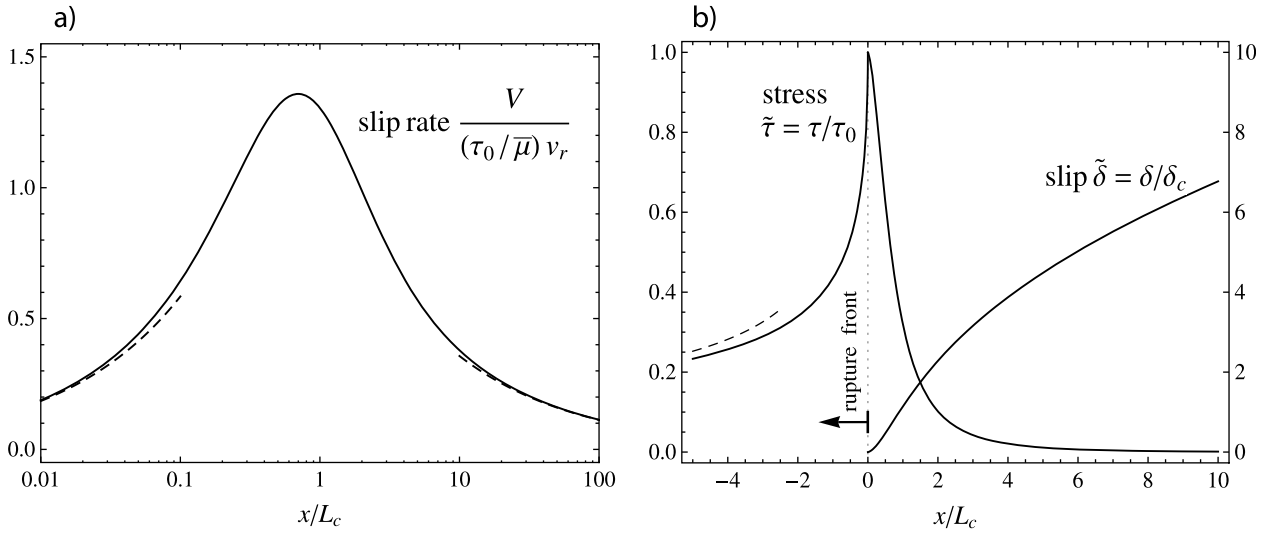

Figure 9. Boundary layer near the advancing tip in the large-slip, undrained solution: variation of (a) the normalized slip velocity and (b) the normalized stress and slip with the distance from the tip $x = 0$. The near and far field slip velocity asymptotes are shown by dashed lines.

expected to cause a small, gradual dissipation of the pore pressure from a high, near-lithostatic value immediately behind the advancing tip BL, and the corresponding small recovery of the fault strength with the increasing distance from the advancing tip. This behavior is apparent in the numerical solution for the partially-drained, self-healing pulse at, for example, $\tau^b/\tau_0 = 0.1$ (Figure 6f). Although deviation from the undrained conditions and the strength recovery away from the advancing tip of the rupture are small in large slip events, they are expected to govern the slip healing and, therefore, duration of the pulse under the stated conditions.

[62] Let us decompose the slip rate and the shear stress in the partially-drained, large-slip pulse into the undrained value and its perturbation due to the hydrothermal diffusion, respectively,

$$V(x) = V^{\text{und}}(x) + \Delta V(x), \quad \tau(x) = \tau^{\text{und}}(x) + \Delta\tau(x), \qquad (37)$$

where $V^{\text{und}}(x)$ is given by (34) and $\tau^{\text{und}}(x) = \tau_0 \exp(-\delta^{\text{und}}(x)/\delta_c)$, (24). Since τ^{und} is exponentially small outside of the boundary layer at the advancing tip, perturbation $\Delta\tau(x)$ is expected to be dominant there (yet still much smaller than the nominal stress level τ_0), i.e.

$$L_c \ll x \le L: \quad \tau(x) \simeq \Delta\tau(x) \ll \tau_0. \qquad (38)$$

The perturbation $\Delta V(x)$ is expected to be small compared to $V^{\text{und}}(x)$ everywhere along the pulse with the exception of the trailing edge. Indeed, the slip healing requires that $V(x)$ vanish as $(L - x)^{3/2}$ when $x \to L$, and, therefore, $\Delta V(x) \simeq -V^{\text{und}}(x) \simeq (v_r/\bar{\mu}) k_L^{\text{und}} \sqrt{L - x}$ for x near L, where $k_L^{\text{und}} = (2/\sqrt{\pi})\, \tau_0 \sqrt{L_c}/L > 0$ is recovered from (35).

[63] These considerations suggest that the perturbation of the undrained solution introduced by the hydrothermal diffusion is localized to a boundary layer near the trailing edge of the pulse. In the following, we develop an asymptotic expression for the fault constitutive law under *nearly* undrained conditions, which we then use to formulate and solve the equations governing the BL at the trailing tip. The overall asymptotic solution (37) for the large-slip, self-healing rupture pulse is also presented.

6.3.1. Asymptotic Form of the Constitutive Law

[64] For a nearly undrained pulse ($T \ll T^*$), the convolution kernel in the fault constitutive law (23) can be expanded into Taylor series, $\mathcal{K}(\zeta; \alpha_{\text{hy}}/\alpha_{\text{th}}) \simeq 1 + \mathcal{K}'(0; \alpha_{\text{hy}}/\alpha_{\text{th}})\zeta$ where $\zeta \ll 1$ and the prime denotes the partial derivative in the first argument. Differentiating the resulting expression for (23) in x/L, we obtain

$$-\frac{d\tau_{\text{f}}}{dx/L} = \tau_{\text{f}} \frac{V}{V_c} - \kappa \frac{T}{T^*} \frac{1}{\delta_c} \int_0^{\delta} \tau_{\text{f}}\, d\delta \qquad (39)$$

where $\kappa \equiv -\mathcal{K}'(0; \alpha_{\text{hy}}/\alpha_{\text{th}}) = -\mathcal{A}'(0)(\alpha_{\text{hy}} + \alpha_{\text{th}})/\alpha$, (A2), and prime denotes the derivative in the first argument. The second term in the right hand side of (39), when non-zero, represents the non-trivial, first-order diffusion correction to the otherwise undrained fault response. It can be shown from (A1) that $\mathcal{A}'(0) = g''(0)/4$, which, for example, suggests that $\kappa > 0$ for all shear distributions which are concave at $y = 0$, $g''(0) < 0$. For the Gaussian distribution, $g''(0) = -2\pi$, and $\kappa = \pi/4$ ($\alpha_{\text{hy}}/\alpha_{\text{th}} = 1$) or $\pi/2$ ($\alpha_{\text{hy}}/\alpha_{\text{th}} = 0, \infty$). (We note that this analysis would have to be revised for shear distributions with $g''(0) = 0$, such as a uniform shear distribution).

[65] The constitutive law (39) can be simplified by approximating the integral in the right hand side to the first order, $\int_0^{\delta} \tau_{\text{f}}\, d\delta/\delta_c \simeq \tau_0(1 - \exp(-\delta/\delta_c))$, and limiting the considerations to large slip, $\delta \gg \delta_c$:

$$L_c \ll x \le L: \quad -\frac{d\tau_{\text{f}}/\tau_0}{dx/L} = \frac{\tau_{\text{f}}}{\tau_0} \frac{V}{V_c} - \kappa \frac{T}{T^*}. \qquad (40)$$

Similar considerations for the temperature, (26), yield

$$\frac{1}{\bar{\sigma}_0/\Lambda} \frac{d(\Theta - \Theta_0)}{dx/L} = \frac{\tau_{\text{f}}}{\tau_0} \frac{V}{V_c} - \kappa_{\text{th}} \frac{T}{T^*}, \qquad (41)$$

where $\kappa_{th} \equiv -\mathcal{A}'(0)\ \alpha_{th}/\alpha$. Eliminating the heating term $\tau_f V/(\tau_0 V_c)$ between (40) and (41) and integrating gives the relation between the temperature change and the strength:

$$L_c \ll x \le L: \quad \frac{\Theta(x)-\Theta_0}{\bar{\sigma}_0/\Lambda} = 1 - \frac{\tau_f(x)}{\tau_0} + \kappa_{hy}\frac{T}{T^*}\frac{x}{L}, \qquad (42)$$

where $\kappa_{hy} \equiv -\mathcal{A}'(0)\ \alpha_{hy}/\alpha$. In (42), the $x/L \to 0$ limit corresponds to the undrained conditions immediately outside of the advancing tip BL.

6.3.2. Boundary Layer at the Trailing Tip and Overall Solution

[66] Let us now consider the perturbed solution (37) and its background stress value τ^b as a function of the patch length L. Representing τ^b as the sum of the undrained value $(\tau^b)^{\text{und}} = (\pi L/L_c)^{-1/2}$, the 1st in (36), and the perturbation $\Delta\tau^b$,

$$\tau^b = \left(\tau^b\right)^{\text{und}} + \Delta\tau^b, \quad \text{with} \quad \Delta\tau^b = \frac{1}{\pi}\int_0^L \frac{\Delta\tau(x')}{\sqrt{x'(L-x')}}dx', \qquad (43)$$

where the $\Delta\tau^b$-expression is based on (B7) and (37). In view of (37) and (43), the elastodynamic equation (21) becomes

$$\frac{L}{L_c}\left(\frac{\Delta\tau(x)}{\tau_0} - \frac{\Delta\tau^b}{\tau_0}\right) = \frac{1}{2\pi}\int_0^L \frac{\Delta V(x')}{V_c}\frac{dx'}{x'-x}. \qquad (44)$$

[67] For a perturbation localized to a BL near the trailing tip, $L - x \ll L$, the 2nd in (43) suggests that $\Delta\tau^b \ll \Delta\tau(x)$ there. Changing to the coordinate system $X = L - x$ moving with the trailing tip, passing to the BL approximation in (44), and neglecting $\Delta\tau^b$, we have

$$\frac{L}{L_c}\frac{\Delta\tau^{\text{BL}}(X)}{\tau_0} = -\frac{1}{2\pi}\int_0^\infty \frac{\Delta V^{\text{BL}}(X')}{V_c}\frac{dX'}{X'-X}, (X = L - x), \quad (45)$$

where the superscript refers to the BL approximation.

[68] On the other hand, the asymptotic form of the constitutive law (40) applied within the boundary layer ($X \ll L$) can be written with the help of (37) and (38) as

$$\frac{d\Delta\tau^{\text{BL}}/\tau_0}{dX/L} = \frac{\Delta\tau^{BL}}{\tau_0}\frac{V^{\text{und}} + \Delta V^{\text{BL}}}{V_c} - \kappa\frac{T}{T^*} \qquad (46)$$

where $V^{\text{und}}/V_c \simeq 2\sqrt{X/\pi L_c}$ in the vicinity of the trailing tip, (35). The terms in the right hand side of (46) correspond to the rates of weakening and strengthening of the fault due to the shear heating and the hydrothermal diffusion, respectively, and the left hand side is the normalized rate of stress change with distance from the trailing tip.

[69] Order of magnitude estimates of the stress-rate and the shear-heating rate in (46) show that they are comparable at distances $X \sim (L/L_c)^{-1/3}\ L \ll L$ from the trailing tip. The latter range defines the BL spatial extent. The BL scaling of the slip velocity and stress perturbations then follows from the self-healing requirement, $\Delta V^{\text{BL}} \sim -V^{\text{und}}$, and the elastodynamics equation (45), respectively: $\Delta V^{\text{BL}} \sim (L/L_c)^{1/3}\ V_c$ and $\Delta\tau^{\text{BL}} \sim (L/L_c)^{-2/3}\ \tau_0$. Further comparison of the diffusion term to the other terms in (46) suggests the scaling for the slip duration: $T \sim (L/L_c)^{-1/3}\ T^*$.

[70] The solution for the normalized slip rate, and shear stress perturbations

$$\Delta\hat{V} = \left(\frac{L}{L_c}\right)^{-1/3}\frac{\Delta V^{\text{BL}}}{V_c}, \quad \Delta\hat{\tau} = \left(\frac{L}{L_c}\right)^{2/3}\frac{\Delta\tau^{\text{BL}}}{\tau_0}, \qquad (47)$$

as a function of the normalized distance from the tip

$$\hat{X} = \frac{L-x}{(L/L_c)^{-1/3}L} \qquad (48)$$

is obtained in section F2 and shown in Figure 10. The corresponding values of the slip duration and the stress perturbation at the trailing edge in this solution are:

$$\frac{T}{T^*} \simeq \frac{0.3727}{\kappa}\left(\frac{L}{L_c}\right)^{-1/3}, \quad \frac{\Delta\tau_L}{\tau_0} \simeq 0.7583\left(\frac{L}{L_c}\right)^{-2/3}. \qquad (49)$$

[71] The *overall* perturbation solution, valid along the entire extent of the pulse, is given in terms of the BL solution as (see section B3)

$$\{\Delta V, \Delta\tau\} = \sqrt{x/L} \times \left\{\Delta V^{\text{BL}}, \Delta\tau^{\text{BL}}\right\}. \qquad (50)$$

A simpler form of this solution valid outside of the trailing tip BL (i.e., the outer solution, $(L/L_c)^{-1/3}\ L \ll L - x \le L$) can be obtained by replacing the BL solution in (50) with its far-field asymptote, which normalized form is given by (F11). Omitting the explicit expressions for brevity, we note the resulting estimates $\Delta V/V_c \sim (L/L_c)^{1/6}\ln(L/L_c)$ and $\Delta\tau/\tau_0 \sim (L/L_c)^{-5/6}$ for the slip rate and stress perturbations, respectively, away from the rupture tips.

[72] Adopting expression (B11) to the trailing tip BL, $\Delta\tau^b \simeq -0.5(\bar{\mu}/v_r)\ \Delta V^{\text{BL}}(0)$, and using (47) with (F11), allows

$$\frac{\Delta\tau^b}{\tau_0} \simeq \left(\frac{L}{L_c}\right)^{-5/6}\left(0.035\ln\frac{L}{L_c} + 0.5045\right). \qquad (51)$$

Substitution of this expression in (43) yields an asymptotic expression of τ^b in terms of L, the inverted form of which is

$$\frac{L}{L_c} = \frac{1}{\pi(\tau^b/\tau_0)^2} - \frac{0.1158\ln\left(\tau^b/\tau_0\right) - 0.7675}{(\tau^b/\tau_0)^{4/3}}. \qquad (52)$$

Here the 2nd term in the right hand side corresponds to drainage perturbation to the otherwise undrained solution (the 1st term).

[73] The large-slip asymptotic solution is shown in Figure 6 by short-dash lines for two values of the background stress, $\tau^b/\tau_0 = 0.1, 0.2$. We observe that the asymptotics provides an excellent approximation to the numerical solutions for the slip rate (Figures 6a and 6b), slip (Figures 6c and 6d), and stress (Figures 6e and 6f) for both the undrained pulse and partially-drained, self-healing pulse, respectively. The asymptotic solution for the temperature in the partially-drained pulse (Figure 6h) is not as accurate for these values of τ^b. This betrays the dependence of the large-slip asymptotics of the temperature (42) on the slip duration, which asymptotic expression, the 1st in (49), is only accurate

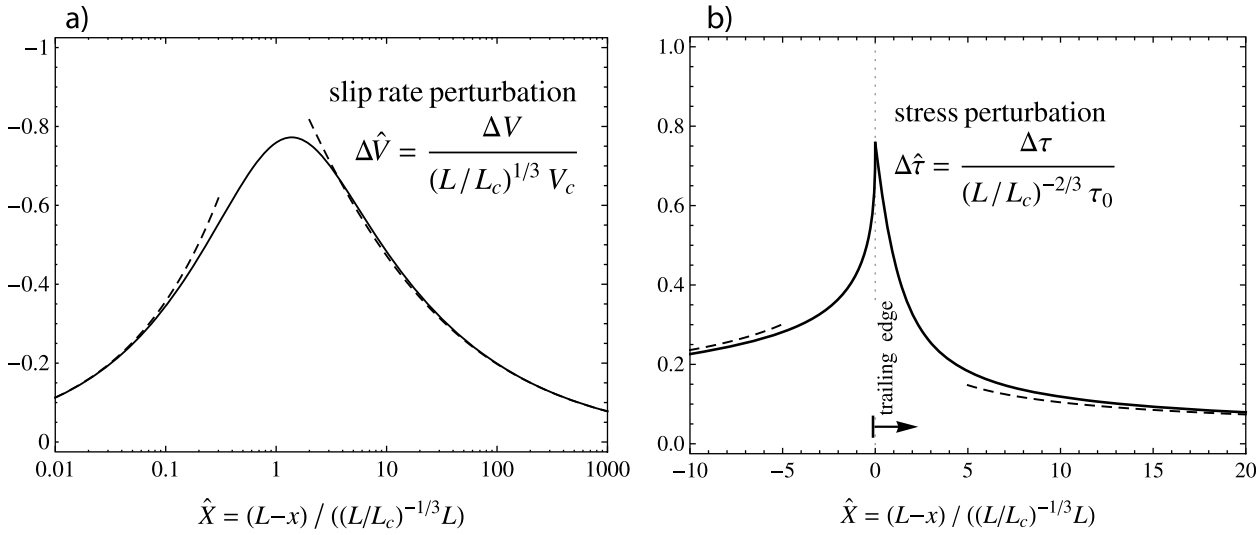

Figure 10. Boundary layer near the trailing tip in the large-slip, partially-drained solution: variation of the normalized perturbations of the (a) slip velocity and (b) stress with the distance from the tip $x = L$. Dashed lines show the near (F8) and far (F11) field asymptotics.

for much smaller values of $\tau^b \lesssim 0.02\tau_0$ (can be shown from comparison of the asymptotics with the numerical solution in Figure 5a).

7. Discussion and Observational Constraints

7.1. Rupture Speed of Self-Healing Pulse and Its Dependence on Shear Zone Thickness

[74] An implicit expression for the rupture velocity (L/T) of the partially-drained, self-healing slip pulse can be obtained from the normalized solutions for L/L_c and T/T^* as a function of τ^b/τ_0 (Figure 5), and the definition of L_c, (22):

$$\frac{v_r/v^*}{F(v_r/c_s)} = \mathscr{V}\left(\tau^b/\tau_0\right) \text{ with } \mathscr{V} \equiv \frac{L/L_c}{T/T^*}, \tag{53}$$

where

$$v^* = \frac{\mu}{\tau_0}\frac{\delta_c}{T^*} = \frac{\mu}{\tau_0}\frac{\rho c}{f\Lambda}\frac{4\alpha}{h} \tag{54}$$

is a characteristic rupture speed. The left hand side of (53) is monotonically increasing function of v_r from zero at $v_r = 0$ to the infinity at $v_r =$ the mode-specific limiting value (c_s or c_R). The right hand side $\mathscr{V}$ has a formal meaning of the normalized rupture velocity in the *quasi-static* limit, since

$$v_r/c_s \ll 1: \quad v_r/v^* = F(0)\mathscr{V}\left(\tau^b/\tau_0\right) \tag{55}$$

where $F(0) = 1$ and $1/(1-\nu)$ for mode III and II ruptures, respectively. Function $\mathscr{V}(\tau^b/\tau_0)$, shown by a heavy line in Figure 11a for $\alpha_{\rm hy}/\alpha_{\rm th} = 1$, is decreasing with the value of the background stress, from the infinite value at $\tau^b/\tau_0 = 0$ to the minimum value of order unity at $\tau^b/\tau_0 = 1$. The corresponding asymptotics,

$$\mathscr{V} \approx 0.458\left(\tau^b/\tau_0\right)^{-8/3} \ \left(\tau^b \ll \tau_0\right), \qquad \mathscr{V} \approx 0.924 \ \left(\tau^b \approx \tau_0\right), \tag{56}$$

are recovered from the large-slip ((36) and (49)) and the small-slip (Figure 3) asymptotic solutions for $\alpha_{\rm hy}/\alpha_{\rm th} = 1$. The rupture velocity of the self-healing pulse increases with the diffusivities' contrast by the maximum factor between 2 (when $\tau^b \ll \tau_0$) to 1.38 (when $\tau^b \approx \tau_0$) attained at $\alpha_{\rm hy}/\alpha_{\rm th} = 0, \infty$ (see also auxiliary material).

[75] Figure 11a illustrates the departure of the normalized rupture velocity v_r/v^* from the quasi-static limit (55), shown by a heavy line, for various fixed values of the ratio of the shear to the characteristic speed (c_s/v^*). In the case with $c_s/v^* = 10$, we track the increase of the mode III rupture speed with decreasing magnitude of the background stress by points "a" through "e", corresponding to a set of values of v_r/c_s from 0.1 to 0.9. The sonic rupture speed is reached asymptotically for vanishing background stress - see the intercept of the mode III v_r/v^*-curve with the vertical axis at the value of c_s/v^*.

[76] The ratio c_s/v^*, when greater than unity, sets the range of possible values of the rupture speed, such that v_r scales with v^* at larger values of τ^b/τ_0 (close to 1), and with c_s at smaller τ^b/τ_0 (Figure 11a). Therefore, when $c_s/v^* \gg 1$, slow, quasi-static rupture pulses are becoming first possible in the $\tau^b \approx \tau_0$, small-slip limit, while the larger is the value of c_s/v^* the wider is the range of the background stress (below the nominal strength) in which the TP slip pulses propagate aseismically. For example, a pulse propagating quasi-statically at 10% of the shear speed or less would require the background stress in excess of 96% (35%) of the nominal strength for $c_s/v^* = 10$ ($c_s/v^* = 100$), see Figure 11a. On the other hand, when $c_s/v^* \lesssim 1$, i.e., v^* is larger than or of the same order of magnitude as c_s, seismic TP pulses are predicted in the entire range of the driving stress.

[77] Writing $c_s/v^* = h/h_{\rm dyna}$ where

$$h_{\rm dyna} = \frac{\mu}{\tau_0}\frac{\rho c}{f\Lambda}\frac{4\alpha}{c_s} \tag{57}$$

denotes a characteristic shear zone thickness, the above observations about the rupture speed variability with the

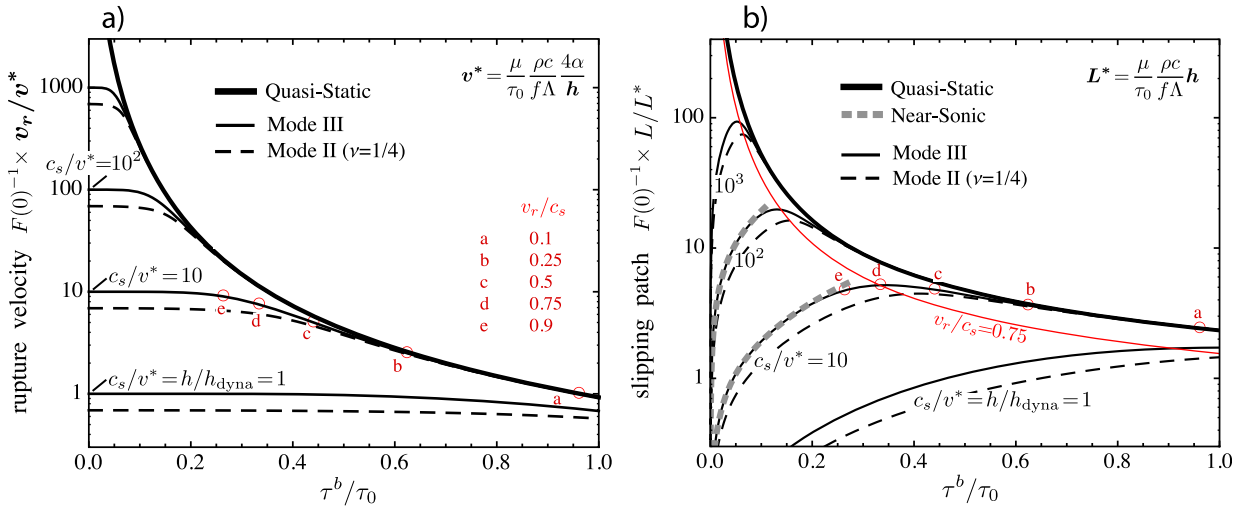

Figure 11. Partially-drained, self-healing pulse with $\alpha_{hy} = \alpha_{th}$: (a) normalized rupture velocity $v_r/F(0)v^*$ and (b) slipping patch L/L^* versus background stress τ^b/τ_0 for various values of ratio c_s/v^* for mode III ($F(0) = 1$) and mode II ($F(0) = 4/3$, dashed lines) cracks. Heavy solid and heavy dotted lines show the limits of quasi-static and near-sonic (Figure 11b only) rupture propagation. In view of $v^* \propto 1/h$, ratio $c_s/v^* = h/h_{dyna}$ can also be interpreted as the normalized shear zone thickness with $h_{dyna} = (\mu/\tau_0)(\rho c/f\Lambda)(4\alpha/c_s)$. Quasi-static rupture pulses can only exist on "thick" shear zones ($h \gg h_{dyna}$), where they are further favored at larger background stress.

ratio c_s/v^* can be rephrased in terms of $h/h_{\rm dyna}$. Specifically, one can state that thick shear zones, $h \gg h_{\rm dyna}$, can support aseismic slip transients for large enough ratio of the background stress to the nominal strength ($\tau^b/\tau_0 \le 1$), while thin shear zones, $h \lesssim h_{\rm dyna}$, can only harbor seismic rupture pulses.

[78] What are representative values of the threshold thickness $h_{\rm dyna}$ of a principal slip zone and of the characteristic rupture speed v^*? Using Byerlee's friction $f = 0.7$, the estimate of the hydraulic parameters for elastic fault walls at 7 km depth [*Rice*, 2006, Table 2], $\alpha_{\rm hy} = 0.86$ mm^2/s and $\Lambda = 1$ MPa/°C, together with $\bar\sigma_0 = 126$ MPa, $\rho c = 2.7$ MPa/°C, $\alpha_{\rm th} = 0.7$ mm^2/s, $\mu = 30$ GPa, and $c_s = 3$ km/s, we get $h_{\rm dyna} \approx 5$ μm and $v^* \approx (16$ m/s) (1 mm/h). Consequently, for this values of fault parameters we observe that critically-stressed faults ($\tau^b \approx \tau_0$) would favor slow slip pulses with $v_r \sim v^* < 1\%$ of the shear speed if the principal shear zone is at least half-a-millimeter thick. The choice of Byerlee's friction is justified with a degree of certainty for slow slip events (SSEs), as well as for seismic ruptures under conditions when no strong dynamic friction-weakening is activated by the slip.

[79] The scaling of these results for $h_{\rm dyna}$ and v^* with the most uncertain parameters is

$$\left\{\begin{matrix} h_{\rm dyna} \\ v^* \end{matrix}\right\} = \left\{\begin{matrix} 5\ \mu\text{m} \\ 16\dfrac{\text{m}}{\text{s}}\left(\dfrac{1\ \text{mm}}{h}\right) \end{matrix}\right\} \left(\frac{0.7}{f}\right)^2 \left(\frac{1\ \text{MPa/°C}}{\Lambda}\right) \cdot \left(\frac{\alpha}{3.1\ \text{mm}^2/\text{s}}\right). \quad (58)$$

For example, using a dynamically-reduced value of friction $f = 0.25$, and the estimate of the hydraulic parameters for damaged fault walls [*Rice*, 2006, Table 2], $\alpha_{\rm hy} = 3.52$ mm^2/s and $\Lambda = 0.34$ MPa/°C, while all else is the same, leads to $h_{\rm dyna} \approx 300$ μm and $v^* \approx (891$ m/s) (1 mm/h). In this case, $h \sim$ decimeter or more would be required for aseismic slip for $\tau^b \approx \tau_0$. On the other hand, limiting h to the maximum of few cms (the upper bound in the observations of inferred principal shear zones of large earthquakes on mature faults [e.g., *Ma et al.*, 2006; *Boullier et al.*, 2009]) or less precludes aseismic slip-pulse propagation in the entire range of the driving stress, and is therefore consistent with the assumed dynamically reduced friction and the fault walls damaged by rapid slip propagation.

7.2. Size of Self-Healing Pulse

[80] Two equivalent expressions for the slipping patch length L can be obtained based on the normalized solutions for $\mathscr{L} \equiv L/L_c$ and $\mathscr{T} \equiv T/T^*$ as a function of τ^b/τ_0 (Figures 5b and 5a), respectively:

$$\frac{L}{L^*} = F(v_r/c_s)\mathscr{L}(\tau^b/\tau_0) \quad \text{and} \quad \frac{L}{L^{**}} = (v_r/c_s)\mathscr{T}(\tau^b/\tau_0), \quad (59)$$

where

$$L^* = \frac{\mu}{\tau_0}\delta_c = \frac{\mu}{\tau_0}\frac{\rho c}{f\Lambda}h, \qquad L^{**} = c_s T^* = \frac{c_s h^2}{4\alpha} \quad (60)$$

are the two corresponding patch lengthscales simply related by $L^{**}/L^* = c_s/v^*$. Using either one of the two expressions in (59) together with the v_r-solution (Figure 11a), we plot the normalized length of the pulse L/L^* versus background stress τ^b/τ_0 in Figure 11b for various fixed values of the shear-to-characteristic speed ratio c_s/v^* (as in Figure 11a). Figure 11b illustrates the departure of the pulse length from the quasi-static limit (shown by a heavy line, $L/L^* = F(0)\mathscr{L}(\tau^b/\tau_0)$) with the diminishing background stress and increasing rupture speed. (The latter exemplified for the case

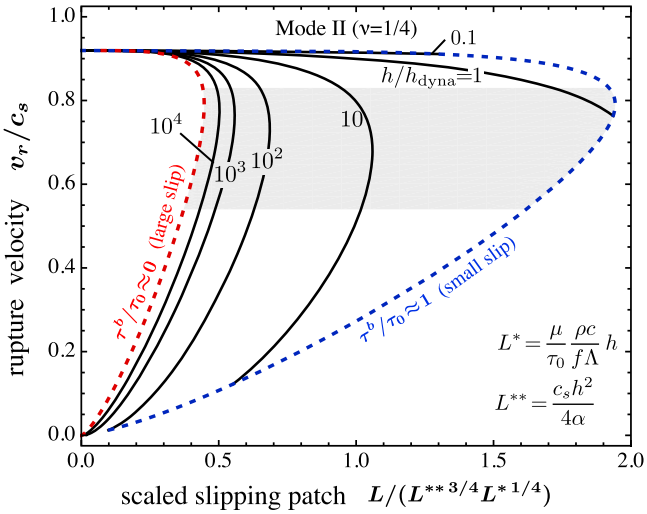

Figure 12. Partially-drained, self-healing, mode II pulse with $\alpha_{\rm hy} = \alpha_{\rm th}$: normalized rupture velocity v_r/c_s versus the scaled size of the slipping patch (in the $L_{\rm max}$-scaling) for various values of h/h_{dyna} ($=c_s/v^*$). The small- and large-slip asymptotic solutions are shown by dotted lines. Shaded area corresponds to the rupture speed range ($v_r/c_s = 0.69 \pm 0.14$) for earthquakes in Table 1, and is roughly correlated with the maximum predicted pulse size.

with $c_s/v^* = 10$ by points "a" through "e"). As the background stress becomes small compared to the nominal strength, the rupture speed approaches the sonic value and the corresponding limit of the pulse length $L/L^{**} = \mathscr{T}(\tau^b/\tau_0)$ follows from the 2nd in (59) by setting $v_r = c_s$ for a mode III pulse. (Analogous expression, adjusted by the factor c_R/c_s, is valid for a mode II, near-sonic pulse). The near-sonic asymptote is exemplified in Figure 11b for the cases with $c_s/v^* = 10$ and 100 by a heavy dotted line.

[81] Therefore, the size L of the slipping patch scales with L^* in the quasi-static and with L^{**} in the near-sonic propagation regimes, which, according to definitions in (60), implies linear and quadratic scaling of L with the principal slip zone thickness h, respectively. Since the corresponding asymptotic expressions predict decreasing ($\propto \mathscr{L}$) and increasing ($\propto \mathscr{T}$) patch size with the background stress (τ^b/τ_0), the maximum patch size is achieved at small-to-intermediate values of τ^b/τ_0, as seen in Figure 11b, and corresponds to subsonic dynamic rupture with v_r/c_s of roughly 0.7 to 0.8 (see the contour-line with $v_r/c_s = 0.75$ for mode III crack, Figure 11b). Under these conditions, using $F(v_r/c_s) \sim v_r/c_s \sim 1$ together with the asymptotics $\mathscr{L} \sim (\tau^b/\tau_0)^{-2}$, (36), and $\mathscr{T} \sim (\tau^b/\tau_0)^{2/3}$, (49), in the respective expressions for L in (59), and subsequently eliminating τ^b/τ_0 between them, we can obtain the following scaling for the maximum patch size:

$$L_{\rm max} \sim L^{**3/4} L^{*1/4} = \left(\frac{c_s}{4\alpha}\right)^{3/4} \left(\frac{\mu}{\tau_0}\frac{\rho c}{f\Lambda}\right)^{1/4} h^{7/4} \qquad (61)$$

Figure 12 shows the rupture velocity of the mode II pulse, normalized by c_s, versus the patch size in the $L_{\rm max}$-scaling, $L/(L^{**3/4}\ L^{*1/4})$, for various fixed values of $c_s/v^* = h/h_{dyna}$. Figure 12 validates the maximum patch scaling (61), by showing that (i) $L_{\rm max}/(L^{**3/4}\ L^{*1/4})$ is $O(1)$ irrespective of value of the shear zone thickness $h/h_{\rm dyna}$, and, furthermore, confined to a narrow range between 1.05 and 0.45 for $h/h_{\rm dyna} \geq 10$; and (ii) the maximum predicted patch size correlates well with the average subsonic values of rupture speed inferred from seismological observations (see the shaded area in Figure 12).

[82] Using the estimate of the fault parameters for elastic fault walls (see section 7.1) together with $f = 0.7$, we can obtain $L^* \approx 1.3$ m $\times$ (h/1 mm) and $L_{\rm max} \sim 66$ m $\times$ (h/1 mm)$^{7/4}$ from (60) and (61), respectively. (We also note that the L_{max}-scaling does not change appreciably when the estimate of hydraulic parameters for damaged fault walls (see also section 7.1) is used instead, together with a reduced $f = 0.25$). Then, a dynamically slipping patch $\sim$1 km long at low background stress would suggest a few mm-thick shear zone ($L_{\rm max}$-scaling). On the other hand, a similarly-sized, slow slip transient operating at $\tau^b \approx \tau_0$ would require a meter-thick shear zone (L^*-scaling).

7.3. Constant Friction Model for Earthquake Slip?

[83] Statically-strong faults that operate at low stress level $\tau^b/\bar{\sigma}_0 \sim 0.1$–$0.2$ require existence of strong dynamic weakening processes, of which the flash heating (FH) on asperities and the thermal pressurization (TP) are likely the two most universal ones [*Rice*, 2006; *Noda et al.*, 2009]. The classical rate-and-state dependence of the fault friction inferred from laboratory observations at below-seismic rates [*Dieterich*, 1979; *Blanpied et al.*, 1991], can account for only a small fraction (less than 10% of the peak friction value $f_p \sim 0.7$–0.8) of the required fault weakening. Thus, the classical rate-and-state effects are likely to be dwarfed by the FH and TP processes during a mature rupture characterized by large slip rates and large accumulated slip. This assertion is further supported by dynamic rupture calculations that account for the classical rate-and-state friction dependence, the FH, and the TP [*Noda et al.*, 2009]. (This situation is expected to be different in the absence of strong dynamic weakening, such as in slow slip events [e.g., *Liu and Rice*, 2007], and/or during the nucleation of earthquake slip [*Dieterich*, 1992; *Lapusta and Rice*, 2003a; *Rubin and Ampuero*, 2005, 2009]).

[84] Numerical solutions of *Noda et al.* [2009] show the evidence that the FH weakening is likely to be localized in a very small region near the tip of advancing rupture, as the most of the corresponding friction drop from the static f_p to the dynamic $f_w \sim 0.1$–0.2 value takes place over very small slip distances $\delta_{\rm FH} \sim 0.01$–$1$ mm associated with the evolution of the frictional contact. The low-end value of the $\delta_{\rm FH}$-range (0.01 mm) is comparable to the asperity size [*Noda et al.*, 2009]. The high-end value (1 mm) is reported by *Kohli et al.* [2011] based on the velocity-stepping experiments at coseismic slip rates in serpentinite, and interpreted by these authors as the slip distance over which the severe localization of the sheared gouge layer takes place, as required for the onset of the FH at asperities contacts. The FH part of the fracture energy can, therefore, be estimated as $G_{\rm FH} \sim (f_p - f_w)\bar{\sigma}_0\delta_{\rm FH} \sim 10^{-3} - 0.1$ MJ/m^2, and is likely to be much smaller than the seismologically-inferred values of the fracture energy of large earthquakes, $G \sim 0.1$–10 MJ/m^2 [e.g., *Rice et al.*, 2005; *Tinti et al.*, 2005; *Abercrombie and Rice*, 2005], and our estimates of

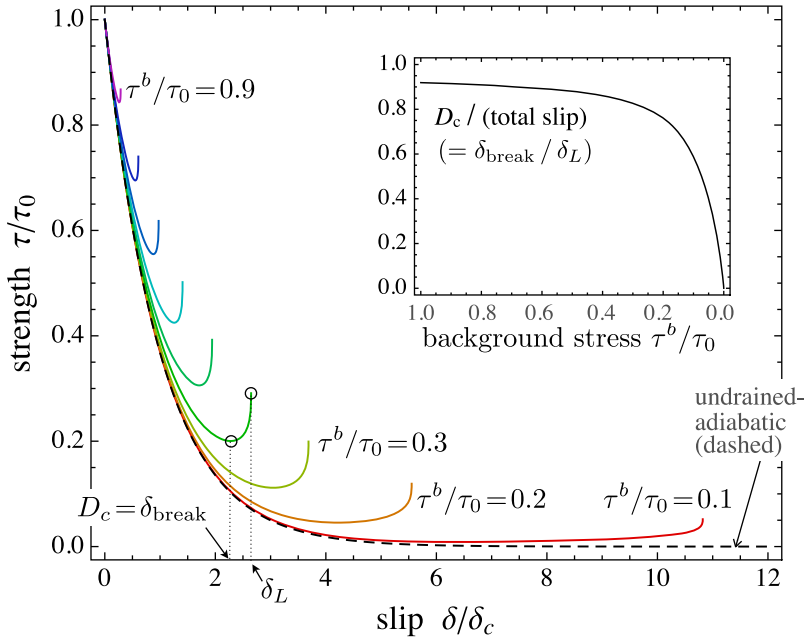

Figure 13. Strength versus slip in the partially-drained, self-healing pulse solution with $\alpha_{\rm hy} = \alpha_{\rm th}$ for various values of the background stress (increment 0.1). The inset shows the breakdown slip ($\delta_{\rm break} = D_c$) as the fraction of the total pulse slip (δ_L) versus the background stress.

the fracture energy associated with the thermal pressurization, $G_{\rm TP} \sim f_w \bar{\sigma}_0 \delta_c \sim$ 1–10 MJ/m^2 (based on the range of $\delta_c \sim$ 0.1–1 m, see section 7.6).

[85] The constant (dynamically-reduced) friction model is, therefore, deemed a reasonable approximation for earthquake ruptures with average slip rates that are sufficiently higher than the FH-activation threshold $V_w \sim 0.1$ m/s [*Rice*, 2006; *Beeler et al.*, 2008; *Kohli et al.*, 2011]. We note in passing that when the $G_{\rm FH}$ is not negligible in the fracture energy balance, an appropriate slip-rate singularity would need to be introduced at the advancing rupture tip if the constant friction model is to be used. This, for example, may be the case when the background stress exceeds the nominal fault strength in the constant friction formulation, $\tau^b > \tau_0 = f_w \bar{\sigma}_0$.

7.4. Slip Weakening Distance in a TP Pulse

[86] In order to examine the nature of fault strength weakening with slip in a TP pulse solution, we plot in Figure 13 the dependence of the strength on the slip in the partially-drained, self-healing TP pulses for different values of the driving stress τ^b/τ_0, as obtained from the corresponding spatio/temporal distributions in Figures 6d and 6f. As already hinted in the discussion of slip development during a TP pulse (section 5.2), Figure 13 clearly illustrates that the most of the dynamic strength loss takes place during largely undrained pressurization process (shown by the dashed line), which is purely slip-controlled, with the well-defined characteristic slip distance given by the *Lachenbruch*'s [1980] δ_c. (We note that this behavior is very different from the TP model of slip on a plane, when the shear zone thickness is neglected [*Rice*, 2006], which is characterized by progressive weakening on all slip scales). The extent of the weakening process in a TP rupture pulse (i.e., the breakdown values of slip and stress) is controlled by the ability of the diffusive heat and pore fluid transport to offset the pressurization, and is the function of the driving stress to the nominal strength ratio (Figure 13).

[87] The breakdown slip $\delta_{\rm break}$ can be identified with the critical slip weakening distance D_c that is usually introduced in the literature in the context of a linear slip-weakening model [e.g., *Ida*, 1972]. The breakdown slip in the TP pulse solution strongly correlates with the total slip, $\delta_{break}/\delta_L \approx$ 0.7–0.9 when δ_L/δ_c is not very large ($\tau^b/\tau_0 \gtrsim 0.15$, see the inset of Figure 13). In the large-slip case ($\tau^b/\tau_0 \lesssim 0.15$) characterized by the complete loss of dynamic strength, the breakdown slip is capped at $\delta_{\rm break} \sim 10\ \delta_c$ (Figure 5c). These $\delta_{\rm break}$-estimates with independently constrained values of the *Lachenbruch*'s [1980] $\delta_c \sim$ few mms to a meter are consistent with (i) seismologically inferred values of D_c in the range of decimeters to meters for moderate-to-large earthquakes [e.g., *Tinti et al.*, 2005; *Mikumo et al.*, 2003, and references therein], and (ii) correlation between D_c and the total slip observed in many of these studies.

7.5. Melting?

[88] As discussed in the above, the spontaneous dynamic TP pulse solution never approaches the state with a fully-drained shear zone, when the approximation of slip on a mathematical plane (i.e., when the shear zone thickness is negligible) [*Rice*, 2006] would be valid. This is the consequence of locking of the slip soon after the diffusion transport of the heat and pore fluid becomes efficient and a relatively small amount of fault restrengthening is realized. As the result, the maximum temperature rise in a spontaneous rupture pulse is smaller (and sometimes significantly so) than the estimates from the kinematic slip solutions (for a fault slipping at constant velocity and friction), in which the hydrothermal regime necessarily evolves from the undrained

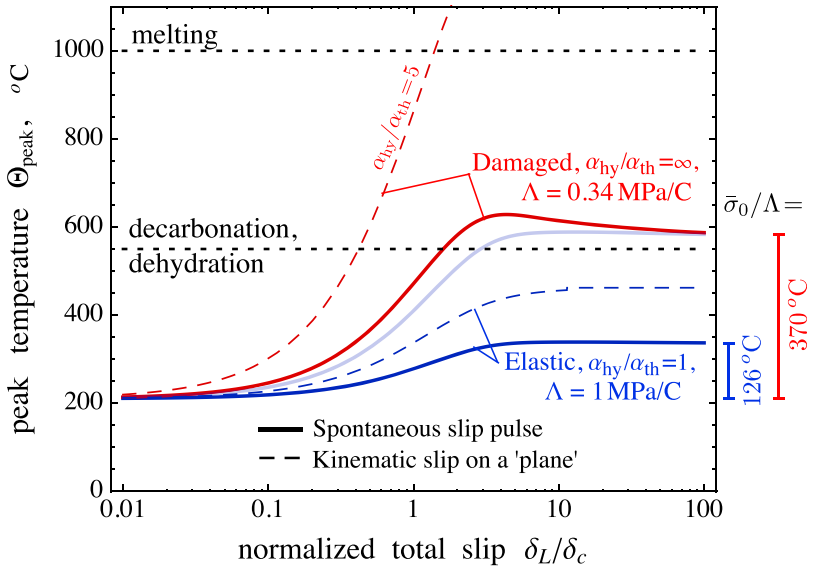

Figure 14. Peak temperature in the partially-drained, self-healing pulse as a function of the normalized total slip for two different estimates of hydraulic parameters corresponding to elastic ($\alpha_{hy}/\alpha_{th} \approx 1$ and Λ = 1 MPa/°C) and damaged ($\alpha_{hy}/\alpha_{th} \gg 1$ and Λ = 0.34 MPa/°C) fault walls at the depth of 7 km, respectively, and the ambient state with $\bar{\sigma}_0$ = 126 MPa and Θ_0 = 210°C. (Note the actual slip value at which the peak temperature is attained within the pulse is ≤ the total slip accumulated during the pulse.) Dashed lines show the solutions for the kinematic slip on a plane [*Rice*, 2006, equation (24)] at a constant slip velocity equal to the average value in the corresponding dynamic pulse solution (where finite "damaged" value α_{hy}/α_{th} = 5 is used). The colored vertical bars show the measure of maximum possible temperature rise ($\bar{\sigma}_0/\Lambda$) for the two sets of fault conditions. The representative temperatures for the onset of melting ~1000°C and thermal decomposition (kaolinite/antigorite dehydration, dolomite decarbonation) ~550°C are indicated by dotted lines. The faint-colored thick line shows the peak temperature rise in the TP pulse for a "mixed-value" estimate of parameters ($\alpha_{hy}/\alpha_{th} \approx 1$ from the elastic-walls estimate and Λ = 0.34 MPa/°C from the damaged-walls estimate). Together with the prediction for damaged walls (thick red line), it is indicative of the limited dependence of the peak temperature on the contrast between the hydraulic and thermal diffusivities.

to the fully-drained regime for large enough slip [*Rempel and Rice*, 2006; *Rice*, 2006; *Noda and Shimamoto*, 2005].

[89] Indeed, the peak temperature rise in a TP pulse can be at most the value closely approximated by the undrained, large-slip solution, i.e., $\Delta\Theta_{peak} \lesssim \bar{\sigma}_0/\Lambda$. (The actual upper bound is a factor of 1 to 1.129 times $\bar{\sigma}_0/\Lambda$, depending on the value α_{hy}/α_{th}). On the other hand, the peak temperature rise in the kinematic slip solution is bounded by the asymptotics of large slip on a mathematical plane, $\Delta\Theta_{peak} \leq (1 + \sqrt{\alpha_{hy}/\alpha_{th}})(\bar{\sigma}_0/\Lambda)$ [*Rempel and Rice*, 2006; *Rice*, 2006]. Therefore, the kinematic slip solution can over-predict the temperature rise by a factor ~2 when $\alpha_{hy}/\alpha_{th} \approx 1$ (e.g., the estimate of *Rice* [2006] for the MTL fault gouge at 7 km depth assuming elastic fault walls), or by a significantly larger factor when $\alpha_{hy} \gg \alpha_{th}$ (e.g., the estimate $\alpha_{hy}/\alpha_{th} \approx 5$ of *Rice* [2006] for damaged fault walls). This is illustrated in Figure 14, which shows the peak temperatures achieved in a self-healing slip pulse (solid lines) and in the kinematic slip on a plane (dashed lines) solutions as a function of the total slip accumulated in the pulse, for two different estimates of hydraulic parameters assuming elastic and damaged fault walls conditions, respectively, at the midseismogenic depth of 7 km ($\bar{\sigma}_0$ = 126 MPa and Θ_0 = 210°C). The solution for the temperature rise during the kinematic slip on a plane [*Rice*, 2006, equation (24)] shown by dashed lines in Figure 14 has been evaluated using the total slip δ_L and the average slip rate δ_L/T values from the pulse solution (which led to the expression $(\delta_L/\delta_c)^2/(T/T^*)$ for the normalized kinematic slip distance in Rice's equation (24)).

[90] The significant implication of our analysis of spontaneous, self-healing TP pulses is that melting, as well as, other thermally-activated fault processes that have been recently linked to strong dynamic fault weakening in rotary shear experiments [e.g., *Di Toro et al.*, 2011, and references therein] are less likely to occur during earthquake slip on mature faults than the kinematic slip solution [*Rempel and Rice*, 2006] would have it. It is evident from Figure 14 that the maximum-possible temperature rise ~126°C (370°C) that can be achieved during a large-slip pulse assuming elastic (damaged) fault walls would elevate the absolute temperature at the midseismogenic depth to ~336°C (580°C). TP pulses of arbitrary magnitude therefore remain relatively cool and far removed from melting temperatures ~1000°C. (The kinematic slip solution, however, predicts melting for large enough slip under the damaged fault walls conditions). Similarly, a number of representative thermal decomposition reactions with the onset temperature ~550°C - dehydration of kaolinite in clay-rich gouge [*Brantut et al.*, 2008], dehydration of antigorite-serpentinite [*Hirose and*

Bystricky, 2007; *Kohli et al.*, 2011], and decarbonation in dolomite-bearing gouges [*De Paola et al.*, 2011] - are ruled out for TP slip pulses under elastic fault walls conditions, and are barely probed in moderate-to-large slip pulses ($\delta_L/\delta_c \gtrsim 1$) when damaged fault walls are assumed (Figure 14).

[91] One can use Figure 14 to estimate the depth below which the critical temperature for a selected decomposition process may be reached coseismically by simply shifting the predicted peak co-seismic temperature curve up to reflect increase of the ambient temperature with depth. Implicit in this exercise is the assumption that the ambient effective stress does not change appreciably with depth below 7 km, which is consistent with the hypothesis [e.g., *Rice*, 1992] that pore pressure tracks the lithostatic gradient below midcrustal depth. Using 27°C/km geothermal gradient, the onset of macroscopic melting (decarbonation/dehydration) is placed for large slip pulses at 31.5 km (15 km) depth for the "elastic" and at 22.5 km (6 km) for "damaged" fault walls conditions.

[92] We note that although our theoretical analysis plays down the likelihood of *macroscopic* melting and thermal decomposition for the assumed range of fault gouge parameters (mainly that of the thermal pressurization factor Λ), it does not contradict the possibility of short-lived, excessive temperature rises borne at grain/asperity contacts (flash heating) that can result in melting/thermal decomposition on the *microscopic* scale. Such microscopic phenomena (which nevertheless can result in dramatic weakening of the sliding friction) have been evidenced in rotary shear experiments where the bulk temperature increase, as measured by thermo-couples near the principal shear zone and/or modeled by FEM, has been below the relevant reaction temperature, yet the reaction products were observed in the mineralogical analysis of the slid gouge [e.g., *Hirose and Bystricky*, 2007; *Brantut et al.*, 2008; *Kohli et al.*, 2011].

7.6. Observational Constraints: Earthquakes

[93] Although spatio-temporal characteristics of earthquake slip inferred from seismic signal inversions are highly variable, an attempt is made to compare the steady slip-pulse solutions for a simplified fault model developed here to the space/time averages of earthquake data. This comparison may help to assess the relevance of the underlying fault model and its assumptions on one hand, and to probe the constitutive parameters of the dynamic fault slip on the other.

[94] We use a compilation (Table 1) of well-studied and constrained, large-to-great earthquakes ($5.7 \le M_w \le 8.8$), with several published kinematic models for each event. The core of the compilation are the events studied by *Heaton* [1990], *Tinti et al.* [2005], and *Cocco and Tinti* [2008]. The latter two studies including estimates of the fracture energy, with some of the recent well-studied great subduction interplate events and large crustal events also added. The choice of particular kinematic models was constrained by the availability of published data on the spatial distributions of slip, rise time, and arrival time, obtained from the WWW data repositories and/or directly from the published manuscripts. These finite fault model data were processed to obtain the average earthquake source parameters shown in Table 1.

[95] We note that a small number of inversions in the compilation (the Denali, Landers, and Parkfield events) are characterized by highly heterogeneous rupture velocity and possible episodic supershear [*Asano et al.*, 2005; *Wald and Heaton*, 1994; *Custodio et al.*, 2009]. Contrasting the fault-averaged data from these events to steady slip-pulse solutions may be somewhat dubious, (unless, as in the case of the Parkfield here, the average is taken over a part of the fault with a diminished rupture heterogeneity). For example, the normalized value of the slipping patch length, L/L_c, for the Denali earthquake is too large to even appear within the range plotted in Figure 15a (discussed below), owing to a near-sonic value of the fault-average rupture velocity, which results in a vanishing characteristic patch size in our model, $L_c \to 0$. The main reason for including these three events in the compilation is to contrast their fracture energy G estimates with the TP-model predictions, as, at least in the undrained limit, G, when expressed as a function of the slip, is independent of rupture model's assumptions (e.g., steady versus unsteady propagation, pulse versus expanding crack, etc.). The fracture energy comparisons can therefore help constrain the impact of the TP processes on the studied events, even when the applicability of the steady, sub-sonic rupture pulse model is questionable.

7.6.1. Inferred Characteristic Slip δ_c and Time T^* Scales, Stress and Nominal Strength

[96] Since the background stress is not readily inferred from a kinematic inversion of seismological data, we represent the TP slip-pulse solution for the normalized patch length L/L_c, fracture energy $G/\tau_0\delta_c$, and pulse duration T/T^* as a function of the total slip and contrast it with the earthquake data in Figures 15a, 15b, and 15c, respectively. The two sets of curves in Figures 15a and 15b correspond to the characteristic fault slip-weakening distance of $\delta_c = 1.2$ m and 0.1 m, respectively: the dashed lines correspond to the undrained pulse solution, while the gray bands correspond to the partially-drained, self-healing pulse solution with $0 \le \alpha_{hy}/\alpha_{th} < \infty$. The model predictions for different values of δ_c can be obtained by translation along a line with slope 1 in the log-log scale of Figures 15a and 15b, which allows to identify the boundary (shown by a dotted line) with the region where no TP pulse solutions exist. The scaled earthquake data in Figures 15a and 15b have been obtained from the data in Table 1 using corresponding values of the apparent dynamic modulus $\bar{\mu}(v_r) = \mu F(v_r)$, calculated for the Mode II and III ruptures; the nominal fault strength, $\tau_0 = f\bar{\sigma}_0$ with a weakened friction $f = 0.25$ (representing, e.g., the flash heating); and $\bar{\sigma}_0$ based on the lithostatic/hydrostatic gradients and the event's median depth, while capped at 126 MPa. We note that the imposed upper bound on the ambient normal effective stress is consistent with the hypothesis of elevated interseismic pore pressure along active faults in a deeper part of the seismogenic zone [*Rice*, 1992]. The corresponding range of variation for the events in Table 1 is $\bar{\sigma}_0 \approx 56$–126 MPa, and, for the corresponding nominal strength, $\tau_0 \approx 14$–32 MPa.

[97] We mention in passing that low nominal strength $\tau_0 = f\bar{\sigma}_0$ is essential in matching the scaled data with the pulse solution predictions in Figures 15a and 15b. Thus, the assumed low friction value (0.25) is not required for the matching as long as the cap value of the ambient effective stress can be reduced within reason. For example, a similar

Table 1. Earthquake Source Parameters[a]

Event	M_o (10^{18}Nm)	Depth (km)	$\sqrt{S}$[b] (km)	c_s (km/s)	v_r (km/s)	T[c] (s)	L (km)	$\bar{\delta}$ (m)	δ_{max} (m)	G[d] (MJ/m^2)	Reference to Kinematic Model[e]
Maule '10	16700	10–65	312	4.7	2.3[f]	18	42	2.4	14	–	A. Sladen and S. Oweng[g]
Nias-Simeulue '05	10000	4–59	275	4.5	2	18	37	2	15	–	*Konca et al.* [2007]
Pisco '07	1210	3–76	99	4.7	2.6[f]	13	33	1.8	–	–	1
Fault 1	364	32–76	63	4.7	2.5[f]	7.9	20	1.3	–	–	
Fault 2	844	8–31	76	4.7	2.8[f]	15	41	2.1	–	–	
Michoacan '85	1500	6–40	155	3.7	2.6	5	13	1.7	6.5	–	2, *Mendoza and Hartzell* [1988]
Benkulu '07	5130	3–98	208	4.7	2.65[f]	6.8	18	1.7	9.6	–	*Konca et al.* [2008]
Pagai Island '07	1100	8–57	130	4.7	2.3[f]	3.3	7.5	0.92	6	–	*Konca et al.* [2008]
Chi-Chi '99	470	0–20	58	3.4	2.5	3.5	8.8	4.5	20	–	*Ma et al.* [2001]
Denali '02	757	0–18	73	3.6	3.3	6.7	22	4.1	11	41.4	*Asano et al.* [2005]
Kashmir '05	282	0–17	50	3.5	2	3.5	7	3.4	10	–	*Avouac et al.* [2006]
Landers'92	77	0–15	33	3.5	2.7	3.5	9.4	2.1	7.9	40.5	*Wald and Heaton* [1994]
Hector Mine '99	63	0–16	32	3.6	1.9	3	5.6	1.8	7	81.2	*Ji et al.* [2002]
Fault 1	26	0–13	21	3.6	1.8	3	5.5	1.7	7	–	
Fault 2	23	0–16	17	3.6	1.8	3.15	5.7	2.3	6.8	–	
Fault 3	14	0–11	17	3.6	2.1	2.5	5.2	1.4	5	–	
San Fernando '71	7	3–16	12	3.5	2.8	0.8	2.2	1.4	2.5	–	2, *Heaton* [1982]
Loma Prieta '89	30	2–20	26	3.6	2.7	1.25	3.2	1.3	4.9	–	*Wald et al.* [1991]
W. Tottori '00	20	1–18	24	3.5	1.8	2.5	4.5	1	2.8	14.3	3
Northridge '94	12	5–20	20	3.6	3	0.92	2.8	0.85	3.2	11.5	*Wald et al.* [1996]
Fukuoka '05	11.5	1–19	22	3.5	2.1	1.9	4	0.76	2.7	10.7	*Asano and Iwata* [2006]
Superst. Hill '87 (3)	3.5	1–12	13	3.2	2.4	0.77	1.8	0.7	1.9	–	*Wald et al.* [1990]
Superst. Hill '87 (2)	0.91	1–12	7.4	3.2	2.4	0.72	1.7	0.6	2.7	–	*Wald et al.* [1990]
Superst. Hill '87 (1)	0.44	1–12	5.9	3.2	2.4	0.71	1.7	0.46	1	–	*Wald et al.* [1990]
Kobe '95	24	0–20	35	3.5	2.8	1.64	4.5	0.63	3.5	3.32	*Wald* [1996]
Borah Peak '83	23	1–21	37	3.5	2.9	0.6	1.7	0.52	1.5	–	2, *Mendoza and Hartzell* [1988]
Imperial Valley '79	5	0–11	19	3.1	2.6	1	2.6	0.5	1.8	3.64	2, *Hartzell and Heaton* [1983]
Colfiorito '97 (Oct)	0.65	3–7	7	3.1	2.3	1	2.3	0.52	0.77	2.22	4
Colfiorito '97 (0940)	1	1–6	9.7	3.1	1.8	1	1.8	0.44	1.4	1.94	4
Colfiorito '97 (0033)	0.44	3–7	6.6	3.1	2.2	1	2.2	0.4	0.64	0.8	4
Morgan Hill '84	2.1	1–12	13	3.1	2.8	0.3	0.84	0.45	1	–	2, *Hartzell and Heaton* [1986]
Morgan Hill '84	2.7	3–13	16	3.5	2.78	0.2	0.56	0.33	2.3	2.72	*Beroza and Spudich* [1988]
Coyote Lake '79	0.35	3–10	6.3	3.3	2.8	0.5	1.4	0.31	1.2	–	2, *Liu and Helmberger* [1983]
N. Palm Springs '86	1.8	4–15	17	3.8	3	0.4	1.2	0.16	0.45	–	2, *Hartzell* [1989]
Parkfield '04	1.1	1–14	19	3.6[h]	3[i]	1.06[i]	3.2	0.09	0.45	0.42	*Custodio et al.* [2009]

[a] M_o, seismic moment; depth range; S, slipped fault area; c_s, shear wave speed in the main source region; v_r, rupture propagation speed; T, duration of slip (rise time); L, length of the slipping patch = $v_r T$; $\bar{\delta}$, average slip in the wake of the pulse = $M_o/\mu S$, assuming $\mu = \rho c_s^2$ and ρ = 2700 kg/m^3 for all but few relatively deeper events (Maule, Nias-Simeulue, Pisco, Benkulu, and Pagai Island, ρ = 3200 kg/m^3); δ_{max}, maximum slip; G, fracture energy.

[b] S values calculated from the kinematic slip model's data available from the Web sites of M. Mai, D. Wald, and A. Sladen (http://www.seismo.ethz.ch/static/srcmod/, http://earthquake.usgs.gov/regional/sca/slipmodels.php, and http://www.tectonics.caltech.edu/sliphistory/, respectively).

[c] T values are the average slip duration over subfaults with significant slip: the lower significant slip bound is $\bar{\delta}/3$ for all events but the Maule, Nias-Simeulue, and Pisco (2 m); and the Benkulu and Pagai Island (est. 0.75 m based on *Konca et al.* [2008]). For inversions with multiple (≥3) time windows, we partition slip episode(s) on a subfault by discounting time windows with negligible slip (<10% of the maximum window slip), and then choosing the longest continuous slip episode from the remaining time-windows. For the Kashmir event, we use median of the 2–5 s range [*Avouac et al.*, 2006].

[d] G values by *Tinti et al.* [2005, 2008] and *Cocco and Tinti* [2008] (their average breakdown work).

[e] References to kinematic slip models are 1, *Sladen et al.* [2010], model with 38 s time delay of the rupture front between the two fault segments; 2, *Heaton* [1990]; 3, H. Sekiguchi (unpublished manuscript, 2002) as reported by *Tinti et al.* [2005]; 4, preliminary model of *Hernandez et al.* [2004] as reported by *Tinti et al.* [2005]; and other references as noted within Table 1.

[f] Average value of v_r estimated from arrival time contours provided in the references.

[g] A. Sladen and S. Owen (Preliminary model combining teleseismic and GPS data 02/27/2010 (Mw 8.8), Chile, 2010, available at http://www.tectonics.caltech.edu/slip_history/2010_chile).

[h] Value of c_s on the SW-side of the fault in a bimaterial crustal model (c_s = 3.3 km/s on the NE-side).

[i] Average values in the area of significant slip to NW of the hypocenter (10–20 km) in the inversion with otherwise highly heterogenous rupture velocity and possible supershear (3.5 km/s) in the hypocentral region [*Custodio et al.*, 2009]. Quoted v_r value (3 km/s) is in line with the direct observation of coseismic surface displacement pulses [*Borcherdt et al.*, 2006] and dynamic modeling [*Ma et al.*, 2008].

quality match to that in Figures 15a and 15b can be obtained by using f = 0.6 and $\bar{\sigma}_0$ = 50 MPa for all events (see auxiliary material), the latter is still within (on the lower-end of) a possible range of the ambient effective stress in the seismogenic crust.

[98] Figure 15a suggests that the relation between the scaled size of the rupture pulse and the accumulated slip for the most part of the considered crustal events can be reasonably bounded by the TP pulse solutions (in the range set by the undrained and the partially-drained, self-healing pulses, respectively) with the unique value of the slip weakening distance, $\delta_c \approx 1.2$ m. Remarkably, this value represents the multitude of crustal events spanning nearly two orders of magnitude of slip, from about 0.1 to 5 m ($\delta/\delta_c \sim 0.1$–4), and the corresponding range of the TP pulse behavior, -from the small-slip pulse asymptotics with $L/L_c \approx 1$–3, independent of slip, to the beginning of the transition to the large-slip pulse asymptote characterized by strong dependence on the slip, $L/L_c \approx \pi^{-1}(\delta/\delta_c)^2$. Corresponding range of the normalized background stress in the TP pulse (Figure 5c)

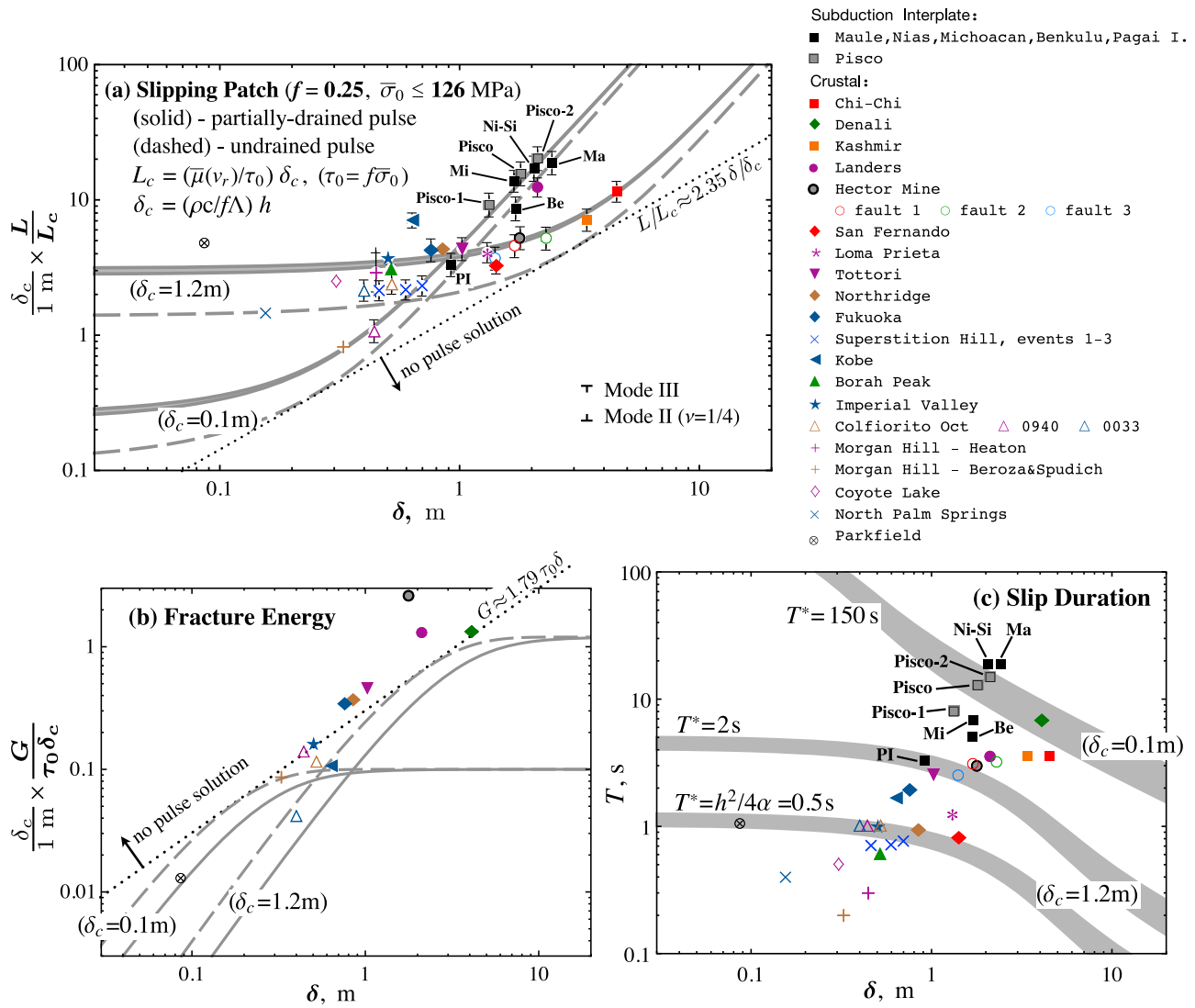

Figure 15. (a) Normalized slipping patch length L/L_c, (b) normalized fracture energy $G/\tau_0\delta_c$, and (c) slip duration T in seconds as functions of total slip δ_L in meters for the earthquake catalog in Table 1. Friction $f = 0.25$, effective normal stress $\bar{\sigma}_0$ = minimum of (18 MPa/km) × (median depth) and 126 MPa, and two different values of the slip-weakening distance δ_c = 1.2 m and δ_c = 0.1 m, respectively, are used to normalize the data. Gray bands show the partially-drained, self-healing pulse solution, which lower (upper) bound in Figure 15a corresponds to α_{hy}/α_{th} = 1 ({0, ∞}), and the reverse of that in Figure 15c, while dashed lines show the undrained pulse solution. Values of the diffusion timescale, T_* = 0.5 s and T_* = 2 s when δ_c = 1.2 m, and T_* = 150 s when δ_c = 0.1 m, are used in Figure 15c to plot the slip duration in the partially-drained pulse solution. The interpretation of the used values of slip (δ_c) and time (T^*) scales in terms of the slip zone thickness and thermo-hydrological parameters of the fault is given in the text.

is $\tau^b/\tau_0 \approx 0.95$–$0.3$ (where the higher value corresponds to the lower slip), and, thus, $\tau^b \approx 30$–10 MPa when $\tau_0 \approx 32$ MPa. This range is in agreement with the stress estimates for major crustal faults, for example, *Townend and Zoback* [2004] estimate for southern and central California part of the San Andreas fault, $\tau^b/\bar{\sigma}_0 \approx 0.2$–$0.3$ and $\tau^b/\bar{\sigma}_0 \approx 0.06$, respectively, which translates to $\tau^b \approx 25$–38 and $\tau^b \approx 8$ MPa at the 7 km median depth of the seismogenic crust ($\bar{\sigma}_0 \approx 126$ MPa).

[99] The subduction megathrusts in our compilation are well modeled by the TP pulse solutions with $\delta_c \approx 0.1$ m, specifically, its large-slip pulse asymptotics, $\delta/\delta_c \approx 10$–$25$ (Figure 15a). This suggests practically complete dynamic stress drop for these events and the background stress ~5–10% of the nominal dynamic strength (Figure 5c), or $\tau^b \approx 1.6$–3.2 MPa ($\tau_0 \approx 32$ MPa). This, very low estimate of the driving stress is consistent with (i) seismological estimates of the static stress drop if it represents complete stress release; and (ii) very low level of megathrust coupling, $\tau^b < 10$ MPa, predicted from analysis of focal mechanisms of small crustal (forearc) earthquakes and lack of the heat flow anomaly [*Wang et al.*, 1995; *Magee and Zoback*, 1993].

[100] The comparison of averaged duration of earthquake slip with the TP self-healing pulse model predictions (Figure 15c) for selected values of the diffusion timescale $T^* = h^2/4\alpha$ shows that, unlike δ_c, there is no well-defined value of T^* for a particular earthquake type: the crustal earthquake data suggests a range $T^* \approx 0.3$–3 s for TP pulses with $\delta_c \approx 1.2$ m; and the subduction megathrust data suggest $T^* \approx 75$–150 s for pulses with $\delta_c \approx 0.1$ m. Furthermore, the data shows a trend for the duration to increase with the amount of slip, whereas the TP pulse solution with fixed T^* shows the opposite tendency. This state of affairs may indicate either that the slip duration is set by some other mechanism of fault restrengthening with diminishing rate of slip; or that the event-average values of the width of the principal shear zone h and/or the two least-constrained hydraulic parameters, α_{hy} and Λ, may vary significantly between different fault zones (or even between different events on the same fault). We don't have a facility to discriminate between these possibilities, and will assume the latter going forward.

7.6.2. Inferred Shear Zone Width and Hydraulic Parameters

[101] Using the order of magnitude estimates $T^* \sim 1$ s for crustal and $T^* \sim 100$ s for subduction interplate events, we can show that h has to exceed 1.7 mm and 17 mm, respectively. The latter values correspond to the lower bound defined by the limit $h = 2\sqrt{\alpha_{th} T^*}$ when $\alpha_{hy} \ll \alpha_{th}$ and $\alpha_{th} \approx 0.7$ mm^2/s. Setting, for example, $h \approx 10$ mm for crustal events with $\delta_c = 1.2$ m results in $\alpha_{hy} \sim 17$ mm^2/s and $\Lambda = (\rho c/f)(h/\delta_c) \approx 0.1$ MPa/°C, -the values that are within a factor of 2 to 3 from those suggested by *Rice* [2006] for the MTL gouge and damaged fault walls, and similar to the values considered by *Noda and Lapusta* [2010] based on the experimental study by *Tanikawa and Shimamoto* [2009] of the gouge from inferred principal slip zone of the Chelungpu fault. The estimated value of Λ may allow for macroscopic melting at the maximum possible temperature rise $\sim\bar{\sigma}_0/\Lambda \sim$ 1260°C attained for crustal earthquakes with moderate-to-large average slip $\delta/\delta_c \gtrsim 2$ (e.g., Chi-Chi, Hector Mine, Landers, and Kashmir events with $\delta_c \sim 1$ m). Increasing shear zone thickness to $h \approx 25$ mm would result in $\alpha_{hy} \sim 130$ mm^2/s and $\Lambda \approx 0.23$ MPa/°C, and preclude melting at arbitrary value of the slip.

[102] On the other hand, using $h \approx 25$ mm for subduction megathrusts leads to $\alpha_{hy} \sim 0.2$ mm^2/s and $\Lambda \approx 2.7$ MPa/°C. There is a lack of information on hydraulic properties of subduction faults in order to assess the relevance of the inferred values directly. Indirectly, the inferred α_{hy}-value is about four times lower than the lower-end estimate for crustal faults (recall the estimate of *Rice* [2006] for elastic fault walls), and orders of magnitude higher than the exceedingly low values based on the permeability estimates put forward by *Audet et al.* [2009] in order to explain the near-lithostatic pore pressure inferred for the part of subducting slab undergoing metamorphic dehydration. On the other hand, the obtained Λ value appears to be too large. Indeed, the upper bound of the pressurization factor can be estimated from the pore fluid properties alone when infinitely stiff gouge matrix is assumed, as $\Lambda < \lambda_f/\beta_f \approx 1.8$ MPa/°C, where thermal expansivity $\lambda_f \sim 0.7 \cdot 10^{-3}$/°C and compressibility $\beta_f \sim 0.39 \cdot 10^{-3}$/MPa values of the supercritical water at 400°C and 450 MPa were used. The latter ambient temperature/pressure conditions represent the 20 km depth along the North Cascadia subducting interface [*Hacker et al.*, 2003], assuming that the pore pressure tracks the lithostatic stress there ($\bar{\sigma}_0 = \sigma_n - p_0 \sim 100$ MPa). (As a side comment, the upper bound estimate for Λ in the crustal settings, using hydrothermal conditions at 7 km depth [*Rice*, 2006], is practically the same ($\sim$1.7 MPa/°C) as the one for subducting slabs.)

[103] The unrealistically large value of $\Lambda = (\rho c/f)(h/\delta_c)$ estimated for subduction megathrust events with $f = 0.25$ and $\delta_c = 0.1$ m can be lowered, if a thinner, and practically impermeable shear zone is assumed, e.g., taking the minimum possible $h \approx 17$ mm yields $\alpha_{hy} \approx 0$ ($\sim 10^{-4}$ mm^2/s) and $\Lambda \approx 1.8$ MPa/°C. Since these estimates still correspond to very restrictive fault conditions, we also explore the possibility that the seismic slip in subduction megathrusts operates at a higher friction than assumed in the above. As already pointed out, a similar quality fit of the data to the pulse model with a higher friction value ($f = 0.6$) and the same $\delta_c = 0.1$ m is obtained if the ambient effective stress is capped at a lower value ($\bar{\sigma}_0 = 50$ MPa), such that the nominal strength $\tau_0 = f\bar{\sigma}_0$ is approximately unchanged (see auxiliary material). Now, using $h \approx 25$ mm in the pulse model with $f = 0.6$ and $\delta_c = 0.1$ m, we estimate a more reasonable value $\Lambda \approx 1.1$ MPa/°C and $\alpha_{hy} \sim 0.2$ mm^2/s the same as before.

7.6.3. Inferred Fracture Energy

[104] Finally, we look at the comparison of the seismological estimates of the fracture energy for a number of crustal events [*Tinti et al.*, 2005, 2008; *Cocco and Tinti*, 2008] with the TP pulse model predictions, Figure 15b. Seismological estimates of G place all energy dissipation in the fault zone (which, besides the fracture energy of the principal slip zone, may include dissipation in inelastic deformation/damage of the gouge/rock outside of the principal slip zone) onto principal slip plane. As the result, a theoretical estimate of G that is based on a model that does not take into account the extra sources of dissipation outside of the principal slip zone, such as the TP pulse model considered in this study, but otherwise matches the inferred slip on the fault plane and the slipping patch size, can be viewed as a lower bound to a seismological estimate. This, indeed, appears to be so in Figure 15b, where the theoretical predictions are consistently less, by an average factor of 1.8, than the data.

[105] The maximum fracture energy of a TP pulse, $\tau_0\delta_c$, is achieved in the large-slip limit ($\delta \gg \delta_c$) that is characterized by the nearly complete dynamic stress drop. For the inferred values of δ_c, $G \lesssim 38$ MJ/m^2 for the crustal events and $G \approx 3$ MJ/m^2 for the great subduction megathrust events in this study. At present, the only available (to our knowledge) seismological estimates of fracture energy of subduction interplate events are for the amended fracture energy G' (based on the static stress drop, the intensity of seismic radiation, and the average slip), which is smaller/larger than G by the product of the dynamic stress undershoot/overshoot onto the earthquake slip [*Abercrombie and Rice*, 2005]. For example, based on the study of *Venkataraman and Kanamori* [2004] of eight large subduction interplate earthquakes, we can obtain the average range $G' \approx 2.4 \pm 1.5$ MJ/m^2, where the lower and upper bounds correspond to the averages based on the minimum and maximum estimates of the static stress

drop used by *Venkataraman and Kanamori* [2004], respectively. This range is rather narrow and, given uncertainty of seismological estimates, is remarkably close to our 3 MJ/m^2 estimate inferred for subduction megathrusts from the independently constrained TP pulse solution.

7.7. Observational Constraints: Slow Slip Events

[106] A partially-drained, TP pulse solution predicts quasi-static rupture propagation for thick principal shear zones, $h \gg h_{\mathrm{dyna}}$, (57), and also, but not necessarily, small total accumulated slip ($\tau^b \approx \tau_0$), see Figure 11. It is, therefore, of interest to investigate the role of the thermal pressurization during the Slow Slip Events (SSEs), -transient aseismic slip observed in many subduction zones below the seismogenic, locked zone [e.g., *Schwartz and Rokosky*, 2007, and references therein], and whether the spatio-temporal development of SSEs can be explained by this mechanism. In the following, we first contrast the appropriately constrained TP pulse solution with the main characteristics of the silent slip events regularly occurring with period of 13–16 months on the northern Cascadia thrust interface [*Dragert et al.*, 2001, 2004]; and, then discuss how TP favors against other physical mechanisms that have been discussed in connection to the aseismic slip transients.

[107] We consider two events from the series of regularly occurring SSEs on the northern Cascadia megathrust, that took place in summers of 1998 and 1999, respectively, and are characterized by large along-strike runout distances ~300 km. The forward models of these events [*Dragert et al.*, 2001, 2004], as well as the kinematic inversion of the time-series of the slow ground motions of the 1999 event [*McGuire and Segall*, 2003], suggest that these SSEs nucleated at the depth of 30–35 km along the subduction thrust interface, propagated updip and downdip over the depth range of roughly 25–40 km (120 to 192 km along the interface dipping at 12°), and then propagated along-strike in the NW direction ('99 event) or bi-directionally, in NW and SE directions, ('98 event) with the speed of 5–17 km/day. High-end speed value (15 km/day) represents roughly the first 200 km of the along-strike propagation in the '99 event (which then slowed down, or stepped over) and the entire along-strike run-out distance of the '98 event [*Dragert et al.*, 2004]. The total accumulated slip in the forward models is 2.3–3 cm uniform along-strike and from about 30 to 40 km depth along the interface, and tapers linearly to zero from 30 to 25 km depth [*Dragert et al.*, 2001, 2004]. The surface displacement anomaly, that signaled a SSE at depth, lasted for 6–14 days at any one GPS location [*Dragert et al.*, 2001], suggesting pulse-like propagation of these SSEs in the along-strike direction. Since duration of slip at depth has to be shorter than its surface signal [e.g., *Liu and Rice*, 2007], we assume the low-end value (T = 6 days) for the average slip duration at the thrust interface, which together with the propagation speed estimate (v_r = 15 km/day) yields the average size of the actively slipping patch traveling along-strike, L = 90 km. The pulse-like nature of these SSEs in the along-strike direction has been also confirmed by *McGuire and Segall* [2003] from the inferred slip time-transients of the '99 event, which prompted these authors to note on the similarity of the SSE propagation mode to that often observed for the earthquake slip [*Heaton*, 1990].

[108] The partially-drained, TP pulse solution in the small-slip regime ($\tau^b/\tau_0 \approx 1$) for the pulse length $L/L_c = L/(\delta_c\bar{\mu}/\tau_0) \approx 2.34$ and duration $T/T^* \approx 2.54$ (see Figure 3 for $\alpha_{\mathrm{hy}}/\alpha_{\mathrm{th}} = 1$), limited to quasi-static rupture speed ($\bar{\mu} = \mu$), allows to estimate the characteristic slip weakening distance $\delta_c \approx 3.87\,(\tau_0 \times 10^4/\mu)$ m and timescale $T^* \approx 3.54$ days in the TP pulse model. We use these estimates to place constraints on the largely uncertain values of the hydraulic parameters α_{hy} and Λ of the gouge, on the thickness of the sheared gouge h, and on the ambient value of the effective stress $\bar{\sigma}_0$, while assuming plausible values for some of the better-constrained parameters (μ = 30 GPa, f = 0.7, ρc = 2.7 MPa/K, α_{th} = 0.7 mm^2/s). The result is shown in Figure 16 as the relations of α_{hy} (a) and h (b) to the product $\Lambda\bar{\sigma}_0$, that are ought to be roughly satisfied were the partially-drained, TP pulse solution to match the observed SSEs' characteristics.

[109] Several recent studies suggest that large quantities of water stored in the hydrous minerals in subducting oceanic crust are released by metamorphic dehydration at depth of the SSEs' source area to the effect of raising the pore pressure there to near-lithostatic values [*Kodaira et al.*, 2004; *Shelly et al.*, 2006; *Audet et al.*, 2009]. Based on the slab fluid production rate ~0.1 mm/yr [*Hyndman and Peacock*, 2003], *Audet et al.* [2009] estimate that very low permeability of the ~1 to 1000 m thick subduction interface, $k \sim 10^{-25}$ to 10^{-22} m^2, is required in order to sustain the near-lithostatic pore pressure there. Corresponding values of the hydraulic diffusivity ($\alpha_{\mathrm{hy}} \sim 10^{-5}$–$10^{-2}$ mm^2/s for assumed bulk compressibility of the fault gouge ~0.1/GPa and a dynamic viscosity of water $\approx 10^{-4}$ Pa s at the temperature and near-lithostatic pore pressure for the Cascadia SSE's median depth of 32.5 km, see the caption of Figure 16) are much smaller than the thermal one ($\alpha_{\mathrm{th}} \sim 0.7$ mm^2/s). This constrains the TP pulse solution to $\Lambda\bar{\sigma}_0 \approx 3.3$ MPa^2/°C (vertical asymptote in Figure 16a) and $h \approx 0.77$ m (Figure 16b). We note that the TP pulse solution with $\alpha_{\mathrm{hy}}/\alpha_{\mathrm{th}} = 0$ would be more appropriate in this example than the one with $\alpha_{\mathrm{hy}}/\alpha_{\mathrm{th}} = 1$ used in Figure 16, but the predictions when using the former ($\Lambda\bar{\sigma}_0 \approx 4.0$ MPa^2/°C and $h \approx 0.84$ m) are not very different. Assuming a plausible range for Λ between 1 and 0.3 MPa/°C, our estimates for $\Lambda\bar{\sigma}_0$ suggest a range of the effective, fault-normal stress $\bar{\sigma}_0 \sim 3$–10 MPa that is consistent with near-lithostatic pore pressure.

[110] It is conceivable that the gouge within the sheared zone ~1 m may develop permeability in excess of the extremely small values suggested by *Audet et al.* [2009]. (Note that a shear zone with increased permeability is likely to be thin compared to the thickness of the subduction interface to significantly perturb/dissipate the near-lithostatic pore pressure there). In this case and due to the lack of information on the hydraulic properties of sheared fault gouge from subduction megathrusts, we use the data of *Wibberley* [2002] and *Wibberley and Shimamoto* [2003] for an ultracataclastic clayey gouge from the principal slip zone of the MTL fault to exemplify 1) what the relevant values of α_{hy}, Λ, and h for a TP-driven SSE might be were the MTL gouge properties similar to those from the subduction interface, and 2) whether the predictions of the TP pulse solution in this case are still consistent with the inferred near-lithostatic values of the ambient pore pressure. The dependence of α_{hy} and Λ on the effective confining stress $\bar{\sigma}_c = \sigma_c - p_0$ for the unloading path from $\bar{\sigma}_c^{\max} = 180$ MPa is shown in

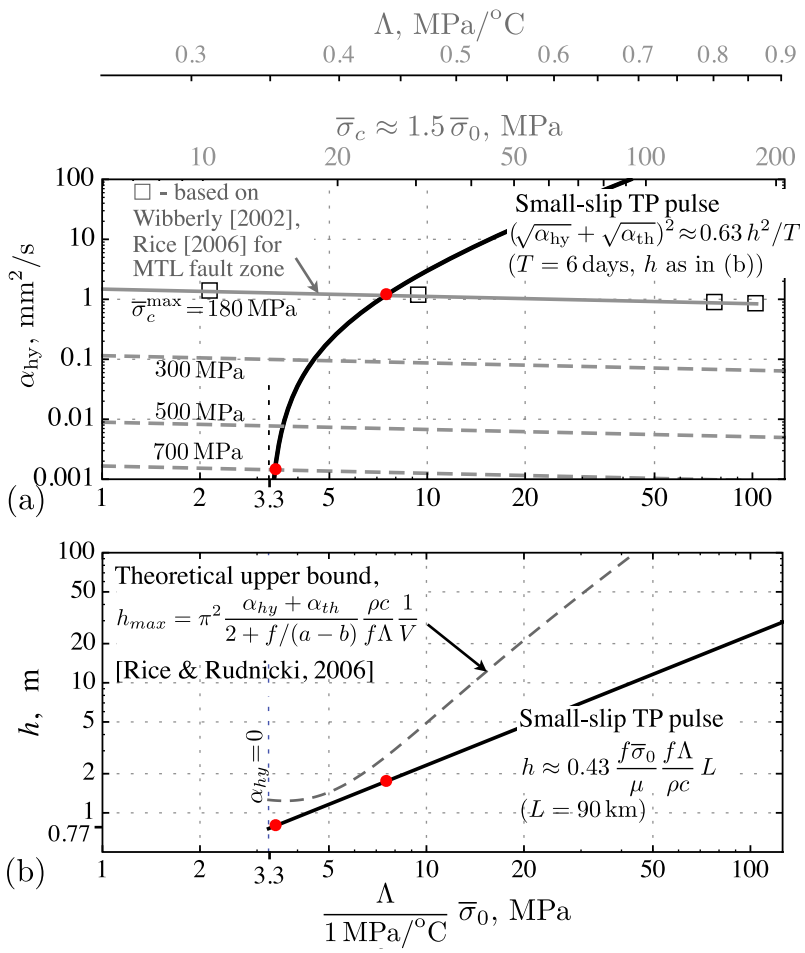

Figure 16. Constraints on the gouge hydraulic parameters $\alpha_{\rm hy}$ and Λ, the shear zone thickness h, and the fault-normal effective stress $\bar{\sigma}_0$ from matching the small-slip, partially-drained TP pulse solution for the slipping patch length and duration (Figure 3, $\alpha_{\rm hy}/\alpha_{\rm th} = 1$), with the observed $L = 90$ km and $T = 6$ days for the '98–'99 Cascadia SSEs [*Dragert et al.*, 2001, 2004]: (a) $\alpha_{\rm hy}$ and (b) h versus $\Lambda\bar{\sigma}_0$. (Assumed values for the other parameters are $\mu = 30$ GPa, $c_s = 3$ km/s, $f = 0.7$, $\rho c = 2.7$ MPa/°C, $\alpha_{\rm th} = 0.7$ mm^2/s.) Gray lines and top axes in Figure 16a show the dependence of $\alpha_{\rm hy} = k/(n(\beta_f + \beta_n)\eta_f)$ and $\Lambda = (\lambda_f - \lambda_n)/(\beta_f + \beta_n)$ of the ultracataclasite gouge from the Median Tectonic Line (MTL) Fault Zone on the effective confining stress $\bar{\sigma}_c$ ($\approx 1.5\bar{\sigma}_0$ for a thrust fault with $f = 0.7$), evaluated from the data of gouge F2xb [*Wibberley*, 2002] for unloading from $(\bar{\sigma}_c)_{\max} = 180$ MPa at room temperature. Specifically, we use Table 3 of *Wibberley* [2002] for the permeability k; Table 1 and Appendix A of *Rice* [2006] for the porosity n, and the pore space pressure and thermal expansivities, β_n and λ_n, respectively; and the values of the pore fluid compressibility, $\beta_f \approx 0.25$/GPa, thermal expansivity, $\lambda_f \approx 0.5 \times 10^{-3}$/°C, and dynamic viscosity, $\eta_f \approx 10^{-4}$ Pa s, for the supercritical H_2O at the temperature $\Theta_0 = 520$°C (thermal model of *Hacker et al.* [2003]) and the near-lithostatic pore pressure $p_0 \approx 900$ MPa at the events' median depth 32.5 km along the top of the subducting slab.

Figure 16a by gray line and gray top axis, respectively. Here, we use $\bar{\sigma}_c/\bar{\sigma}_0 \approx 1.5$ (a value representing the range ≈1.2 to 1.7 for a thrust fault with $f = 0.7$) to convert between the effective confining and the fault-normal stresses. The assumed value of $\bar{\sigma}_c^{\max}$ is likely at the lower end, that is consistent with the notion of elevated interseismic pore pressure along active faults in the seismogenic zone [*Rice*, 1992], of a possible range ~180 to 700 MPa of the peak confining stress experienced by the subducting slab before the unloading by the pore pressure increase due to the onset of metamorphic dehydration at depth ~25 km. (The high end value corresponds to the lithostatic/hydrostatic gradients at the top of the dehydration region). In order to infer $\alpha_{\rm hy}$ along unloading paths from different values of $(\bar{\sigma}_c)_{\max}$, we fit the *Wibberley*'s [2002] unloading data by a power law $k \approx k_{\min}(\bar{\sigma}_c^{\max})(\bar{\sigma}_c^{\max}/\bar{\sigma}_c)^{0.74}$ for $\bar{\sigma}_c \le \bar{\sigma}_c^{\max}$, where $k_{\min}(\bar{\sigma}_c) \approx 4.4 \cdot 10^{-10} \cdot ((1\ \text{MPa})/\bar{\sigma}_c)^{5.0}$ m^2 is the power-law fit to the *Wibberley*'s [2002] loading data (see Figure S7 in the auxiliary material). When extrapolated to $\bar{\sigma}_c^{\max} \ge 180$ MPa, these approximations indicate almost three order of magnitude of the permeability drop for the suggested $\bar{\sigma}_c^{\max}$ - range. Neglecting the dependence of other poromechanical

parameters that enter the expressions for α_{hy} and Λ on the virgin consolidation stress $\bar{\sigma}_c^{max}$, when compared to that of k, the inferred α_{hy} of the MTL-type gouge is shown in Figure 16a (gray lines) for several values of $\bar{\sigma}_c^{max}$ within the suggested range. Juxtaposition of the latter α_{hy} dependency with that in the constrained TP pulse model (heavy line) suggests that the North Cascadia SSEs can operate over a wide range of the MTL-like hydraulic diffusivity $\alpha_{hy} \sim 1$ to 10^{-3} mm^2/s corresponding to $\bar{\sigma}_c^{max} \sim 180$ to 700 MPa, while the corresponding ranges of $\Lambda \approx 0.43$ to 0.35 MPa/°C, of the effective fault-normal stress $\bar{\sigma}_0 \approx 17$ to 10 MPa, and of the shear zone thickness $h \approx 1.7$ to 0.79 m (Figure 16b) are quite narrow.

7.7.1. Thermal Pressurization Versus the Rate- and State-Dependent Friction Mechanism

[111] We have shown in the above that the TP pulse solution with independently constrained gouge parameters can describe the basic spatio-temporal features of the slow slip propagation and is also consistent with near-lithostatic level of the pore pressure inferred seismologically at the source of the slow slip. This suggests that thermal pressurization may, indeed, be one of or the dominant mechanism at the SSE source. Contrary to that, *Segall et al.* [2010], based on the analysis of *Segall and Rice* [2006], estimate for the range of slip velocities (up to 2–3 orders of magnitude above the plate velocity) corresponding to aseismic slip transients that the TP effects on the fault strength are likely negligible compared to those of the rate-and-state dependence of the fault friction. This apparent contradiction can be reconciled, by noting that these and other similar estimates [*Garagash et al.*, 2005] are based on two assumptions, which validity for the aseismic slip is questionable.

[112] The 1st is of a thin, sub-mm thick shear zone, that is relevant to seismic slip on mature faults [e.g., *Rice*, 2006, and references therein], but has no pervasive evidence to be valid for slow slip. J. R. Rice and J. W. Rudnicki (unpublished manuscript, 2006) and *Platt et al.* [2010] provide a theoretical upper-bound to the thickness of the gouge zone where the shear is localized (assuming velocity-strengthening gouge friction and the TP framework), which is consistent with our estimates of a meter-thick shear zone harboring slow slip (Figure 16b).

[113] The 2nd concerns the typically assumed magnitude $|a - b| \sim 5 \cdot 10^{-3}$ of the steady-state friction dependence on the slip velocity, $\mathrm{d}f = (a - b)\mathrm{d}V/V$, that is representative of both locked (seismogenic) and creeping (stable) parts of the fault [*Blanpied et al.*, 1998], respectively, but may be an overestimated for the transitional part of the fault with near-neutral friction, where SSEs are observed. Indeed, based on the recent study of gabbro friction under hydrothermal conditions [*He et al.*, 2007], the velocity-neutral friction ($a - b = 0$) corresponds to 517°C or the 31.8 km depth along the northern Cascadia subduction interface [*Hacker et al.*, 2003], and, as first pointed out by *Liu and Rice* [2009], ties it to the SSE source. Based on the data of *He et al.* [2007], one can obtain the average value $a - b \approx 6 \cdot 10^{-4}$ over the frictionally-stable part of the slipped interface (31.8 to 40 km depth), and, approximately the same value for the average magnitude $|a - b| \approx 6.3 \cdot 10^{-4}$ over the entire slipped interface (25–40 km depth). (This estimate is halved when only the half of the slipped interface centered around the neutral-friction depth, i.e., 28–36 km depth range, is considered). We, therefore, conclude that the effect of the friction rate-dependence at the SSE source may be an order of magnitude smaller than suggested earlier by *Segall et al.* [2010].

[114] The average and the maximum loss of the dynamic strength in the TP, small-slip pulse solution (Figure 4c) are $f\Delta p \approx 1.13\ (\tau_0 - \tau^b)$ and $1.6\ (\tau_0 - \tau^b)$, respectively. Combining the pulse solutions for the total slip and the patch length (Figure 3) as $\delta_L/L \approx 1.16\ (\tau_0 - \tau^b)/\mu$ and using it in the expression for the average dynamic strength loss, one can estimate $f\Delta p \approx 8.8$ kPa for the Cascadia SSEs. On the other hand, the average magnitude of the friction coefficient change due to the inferred velocity-dependence over the slipped interface can be estimated as $|\Delta f| = |a - b| \ln(V/V_{pl}) \approx 2.4 \cdot 10^{-3}$ (using $V = 4.5$ mm/day, $V_{pl} = 38$ mm/yr, and $|a - b| = 6.3 \cdot 10^{-4}$), which translates to $|\Delta f|\bar{\sigma}_0 \approx 2.4$ to 24 kPa for the magnitude of the strength change when $\bar{\sigma}_0 \sim 1$ to 10 MPa is assumed.

[115] Recent 2D simulations of slow slip transients that neglect the TP [*Liu and Rice*, 2007, 2009; *Segall et al.*, 2010] show that the velocity-strengthening of the gouge friction with depth may control the down-dip propagation of slow slip, while the up-dip boundary of the region with lithostatic pore pressure or/and gouge dilatancy [*Segall et al.*, 2010] may define the up-dip extent of the slip. Our estimates for the along-strike slip propagation show that the effects of the thermal pressurization ($f\Delta p$) and of the friction changes with the slip velocity ($|\Delta f|\bar{\sigma}_0$), respectively, on the gouge strength are comparable within the range of $\bar{\sigma}_0$ constrained by near-lithostatic values of the pore pressure at the SSE source, while the thermal pressurization dominates at the low-end of this range. It therefore appears that while some friction rate-weakening may be required to nucleate the SSE in the first place, thermal pressurization mechanism has to be included in realistic models of dynamics of aseismic slip transients, as long as the source of the transients is linked to the conditionally-stable part of the interface (with near velocity-neutral friction).

8. Summary and Conclusions

[116] 1. We have studied spontaneous, steady propagation of a rupture pulse driven by thermal pressurization of the pore fluid on a fault loaded by uniform background stress, assuming a constant friction along the slipping patch. The corresponding family of the TP pulse solutions is parameterized by the magnitude of the background shear stress normalized by the nominal strength (τ^b/τ_0), and the slip duration normalized by the characteristic time for hydro-thermal diffusion across the shear zone (T/T^*). The hydro-mechanical response of the fault to a TP rupture pulse is weakly dependent on the contrast between the hydraulic and thermal diffusivities, and, to the first order, depends only on the lumped hydro-thermal diffusivity $\alpha = (\sqrt{\alpha_{hy}} + \sqrt{\alpha_{th}})^2$ via the characteristic timescale $T^* = h^2/4\alpha$.

[117] 2. The multitude of pulse solutions are bounded by the undrained-adiabatic pulse solution, corresponding to the minimum slip duration $T \ll T^*$, on one hand, and by the partially-drained, *self-healing* pulse solution corresponding to the maximum slip duration, $T \sim T^*$ ($T \sim (\tau^b/\tau_0)^{2/3}\ T^*$ when $\tau^b/\tau_0 \ll 1$), on the other hand. For all pulse solutions, the initial acceleration of slip with the passage of the rupture

front takes place due to the undrained-adiabatic TP and related reduction of the fault strength. With the passage of time and slip, diminishing rate of heating (due to the reduction of the fault strength) and increasing rate of hydrothermal diffusive transport of heat and pore fluid from the shear-heated zone (partially-drained pulse) offset TP, and result in slip deceleration, partial recovery of the strength, and eventual locking of the slip. The partially-drained pulse with the maximum slip duration set by the hydrothermal diffusion timescale T^* possesses an intrinsic self-healing property, i.e., the recovery of the fault strength (by pore pressure diffusion) after the passage of the pulse takes place faster than the elastic rebound of the shear stress.

[118] 3. Strong velocity weakening friction, or heterogeneity of stress and strength along the fault, or material properties across it are, therefore, not necessary to explain the occurrence of self-healing rupture pulses with properties (rupture velocity, slipping patch size, slip duration, fracture energy) consistent with seismological observations [e.g., *Heaton*, 1990]. If such other healing mechanisms are present, they can be responsible for existence of slip pulses which are "too short" to be healed by the hydrothermal diffusion alone (e.g., undrained-adiabatic TP pulse).

[119] 4. Locking of the slip soon after the diffusion transport of the heat and pore fluid becomes efficient ($T \lesssim T^*$) in our pulse solutions indicates that the conditions within the principal shear zone never approach co-seismically the fully-drained conditions, synonymous with the assumption of negligible shear zone thickness in models of slip on a mathematical plane [e.g., *Rice*, 2006]. This has important implications for the characteristic slip weakening distance of earthquake rupture and in moderating the temperature rise in the course of the slip.

[120] 5. Most of the fault weakening in a TP slip pulse takes place during the incipient, undrained-adiabatic pressurization process, which is purely slip-controlled, with the well-defined *Lachenbruch*'s [1980] characteristic slip distance $\delta_c = \rho ch/f\Lambda$. The extent of the weakening (the breakdown values of the slip and the stress) as well as the total slip in the pulse are controlled by τ^b/τ_0. The lower the background stress is to the nominal strength, the larger is the total accrued slip and the more complete is the dynamic loss of fault strength required to drive the pulse, and are further moderated by T/T^*.

[121] 6. The end-member behavior of the TP weakening with τ^b/τ_0 is given by the asymptotic solutions for the small-slip, small-weakening pulse with $\tau^b/\tau_0 \approx 1$ and the large-slip, large-weakening pulse with $\tau^b/\tau_0 \ll 1$, respectively, for which a variety of important analytical results, that constrained otherwise numerical solution in intermediate range of τ^b/τ_0, is obtained.

[122] 7. If the pulse-like mode of earthquake rupture comes to be expected for $\tau^b/\tau_0 \ll 1$ for a variety of fault constitutive models [e.g., *Perrin et al.*, 1995; *Zheng and Rice*, 1998; *Noda et al.*, 2009], it is the enlarging crack-like rupture mode that has been more commonly observed in numerical simulations of spontaneous dynamic rupture at larger values of background stress [*Noda et al.*, 2009]. Thus, it appears that the existence of pulse solutions for $\tau^b/\tau_0 \sim 1$ conclusively shown in this study is a new result. Since these solutions are for a steadily propagating rupture pulses, they bear no information on the nucleation process that may lead to their realization in nature. This is a subject for future work.

[123] 8. The predicted temperature rise during a self-healing TP pulse is bounded by $\bar{\sigma}_0/\Lambda \sim 50$ to 300°C, which is smaller (significantly so for larger slip) than values previously suggested by kinematic slip solutions [e.g., *Rice*, 2006]. As a result, bulk gouge melting and, to lesser degree, some thermal decomposition reactions (gouge dehydration, decarbonation, etc.) are not likely during seismic slip pulses driven by thermal pressurization. A self-consistent picture emerges, where (i) generally small stress level at which mature fault zones operate (as discussed in section 7.6) favors the pulse-like over the crack-like mode of seismic rupture [e.g., *Zheng and Rice*, 1998; *Noda et al.*, 2009; this study], as further supported by seismological observations [*Heaton*, 1990]; while (ii) the pulse-like nature of the earthquake slip appears to be essential in keeping the fault temperature well below melting temperatures (this study), as supported by relatively scarcity of geological observations of macroscopic melting in exhumed mature fault zones [e.g., *Sibson and Toy*, 2006].

[124] 9. Matching of the earthquake data for the length of the slipping patch and the total slip with the predictions of slip-pulse solutions suggests that both mature crustal faults and subduction megathrusts have a similar nominal dynamic strength $\tau_0 = f\bar{\sigma}_0 \sim 30$ MPa (before the onset of the TP), and different magnitudes of driving stress, namely, ~10 to 30 MPa for crustal events (where lower value corresponds to a larger slip event) and very low ~1 to 3 MPa for large subduction events.

[125] 10. The matching does not single out a particular level of dynamic friction during seismic slip, since equally good match is achieved when $f = 0.25$ with $\bar{\sigma}_0 \lesssim 126$ MPa ("<" corresponds to events roughly shallower than 7 km), and when $f = 0.6$ with $\bar{\sigma}_0 \approx 50$ MPa. Both cases correspond to roughly the same nominal strength τ_0, and the two values of $\bar{\sigma}_0 = \sigma_n - p_0$ represent bounds of a possible range of the effective stress in the crust where the pore pressure tracks the lithostatic stress [e.g., *Rice*, 1992].

[126] 11. Remarkably, all crustal earthquakes in this study (spanning nearly two orders of magnitude of seismically accrued slip) correspond to the unique value of the characteristic slip weakening distance $\delta_c \approx 1$ m, while all large subduction interplate events in the compilation are roughly represented by $\delta_c \approx 0.1$ m. These estimates together with the estimates of the diffusion timescale T^* (~1 s for crustal and ~100 s for subduction events obtained from matching the observed and modeled slip duration) allows to infer the nominal thickness of the principal shear zone ~10 to 30 mm, and hydraulic properties of the gouge that are roughly consistent with the estimates put forward by *Rice* [2006, Table 2] for elastic fault walls conditions (subduction events in this study) and for damaged fault walls conditions (crustal events in this study), respectively.

[127] 12. Rupture velocity of a TP pulse is a function of the shear zone thickness. We find that "thick" shear zones, $h \gg h_{\text{dyna}}$, where $h_{\text{dyna}} = (\mu/\tau_0)(\rho c/f\Lambda)(4\alpha/c_s)$, can support aseismic TP pulses propagating at a fraction h_{dyna}/h of the shear speed, while "thin" shear zones, $h \sim h_{\text{dyna}}$ or thinner, can only harbor seismic slip.

[128] 13. For plausible range of fault parameters, h_{dyna} is between 10 s to 100 s of micrometers, suggesting that slow

slip transients propagating at 1 to 10 km/day may occur in the form of a TP slip pulse accommodated by a meter-thick shear zone. We verify that this is, indeed, a possibility by contrasting the predictions for aseismic, small-slip TP pulses operating at seismologically-constrained, near-lithostatic pore pressure with the observations (slip duration at a given fault location, propagation speed, and the inferred total slip) for along-strike propagation of the North Cascadia slow slip events of '98–99 [*Dragert et al.*, 2001]. Furthermore, we show that the effect of thermal pressurization on the strength of the subduction interface is comparable to or exceeds that of the rate-dependence of friction, previously suggested as a mechanism for aseismic transients [e.g., *Liu and Rice*, 2009; *Segall et al.*, 2010], if the frictional properties of gabbro [*He et al.*, 2007] under the hydrothermal conditions for the North Cascadia slab [*Hacker et al.*, 2003] are used.

[129] 14. The results of these studies point to the importance of the principal shear zone thickness during a slip event and its possible change with the slip rate [e.g., *Platt et al.*, 2010]. The predicted seismic and aseismic TP pulses operate on shear zones of very different thickness. The insight into how stable creep or a slow slip event may transition into a seismic rupture and how an earthquake rupture "selects" its principal shear zone, which is shown to largely define the TP slip dynamics, may require addressing the slip localization as a phenomena concurrent to the development of transient slip, and therefore coupled to other relevant source mechanisms (thermal pressurization, flash heating, etc).

Appendix A: Convolution Kernels

[130] The solution of the diffusion equation (6) for the temperature and pressure changes on the $y = 0$ plane [*Rice*, 2006, Appendix B] can be written in the form (13) and (14), which makes use of the normalized convolution kernels for the temperature,

$$\mathcal{A}(\zeta) = \frac{1}{\sqrt{\pi}} \int_{-\infty}^{\infty} g\left(s\sqrt{\zeta}\right) \exp\left(-s^2\right) ds, \quad \left(\zeta = \frac{t-t'}{T_{\text{th}}}\right), \tag{A1}$$

and for the pressure,

$$\mathcal{K}(\zeta;\chi) = \frac{\alpha_{\text{hy}}\mathcal{A}\left(\alpha_{\text{hy}}\zeta/\alpha\right) - \alpha_{\text{th}}\mathcal{A}\left(\alpha_{\text{th}}\zeta/\alpha\right)}{\alpha_{\text{hy}} - \alpha_{\text{th}}}, \quad \left(\zeta = \frac{t-t'}{T*}\right), \tag{A2}$$

where $g(y/h)$ is the normalized shear distribution function, (2), $\alpha_{\text{hy}}/\alpha = (1+\chi^{-1/2})^{-2}$, $\alpha_{\text{th}}/\alpha = (1+\chi^{1/2})^{-2}$, and $\chi \equiv \alpha_{\text{hy}}/\alpha_{\text{th}}$.

[131] The $\zeta \to 0$ asymptotics, $\mathcal{A}(0) = 1$, follows from the integration of (A1) and the use of the constraint $g(0) = 1$. The $\zeta \to \infty$ asymptotics, $\mathcal{A}(\zeta) = 1/\sqrt{\pi\zeta}$, is recovered by the change of the integration variable in (A1) to $s\sqrt{\zeta}$ and the use of the constraint $\int_{-\infty}^{\infty} g(s)ds = 1$. Corresponding asymptotic expressions for the kernel $\mathcal{K}(\zeta;\chi)$, (A2), are identical to the above expressions for $\mathcal{A}(\zeta)$.

[132] For a class of shear distributions centered about the midplane $y = 0$ and monotonically decreasing with the distance from it ($g(s) = g(-s) > 0$ and $g'(s > 0) \le 0$), kernels $\mathcal{A}$ and $\mathcal{K}$ are everywhere positive, monotonically decreasing functions of their argument.

[133] Indeed, positiveness of $\mathcal{A}(\zeta)$ follows from its definition (A1), while the derivative of $\mathcal{A}$, evaluated as,

$$\mathcal{A}'(\zeta) = \frac{1}{2\sqrt{\pi\zeta}} \int_{-\infty}^{\infty} g'\left(s\sqrt{\zeta}\right) s \ \exp\left(-s^2\right) ds, \tag{A3}$$

is negative for all $\zeta \ge 0$, since $g'(s\sqrt{\zeta})\, s/\sqrt{\zeta} \le 0$ for all s.

[134] To establish the same properties for $\mathcal{K}(\zeta;\chi)$, we first notice that based on (A1) and (A3)

$$\mathcal{A}(\omega\zeta) = \frac{1}{\sqrt{\pi}} \int_{-\infty}^{\infty} g\left(s\sqrt{\zeta}\right) \frac{\exp(-s^2/\omega)}{\sqrt{\omega}} ds,$$

$$\mathcal{A}'(\omega\zeta) = \frac{1}{2\sqrt{\pi\zeta}} \int_{-\infty}^{\infty} g'\left(s\sqrt{\zeta}\right) \frac{\exp(-s^2/\omega)}{\omega^{3/2}} s ds,$$

for any $\omega > 0$. Kernel $\mathcal{K}$, (A2), and its derivative can then be expressed as

$$\mathcal{K}(\zeta;\chi) = \frac{1}{\sqrt{\pi}} \int_{-\infty}^{\infty} g\left(s\sqrt{\zeta}\right) \Psi(s;\chi) ds, \tag{A4}$$

$$\mathcal{K}'(\zeta;\chi) = \frac{1}{2\sqrt{\pi\zeta}} \int_{-\infty}^{\infty} g'\left(s\sqrt{\zeta}\right) s \ \Psi(s;\chi) ds, \tag{A5}$$

respectively, where function

$$\Psi(s;\chi) = \frac{\alpha}{\alpha_{\text{hy}} - \alpha_{\text{th}}} \cdot \left(\sqrt{\frac{\alpha_{\text{hy}}}{\alpha}} \exp\left(-\frac{\alpha}{\alpha_{\text{hy}}} s^2\right) - \sqrt{\frac{\alpha_{\text{th}}}{\alpha}} \exp\left(-\frac{\alpha}{\alpha_{\text{th}}} s^2\right)\right)$$

is strictly positive for all positive α's. The stated properties of $\mathcal{K}$ then follow from (A4) and (A5).

Appendix B: Properties of Elastodynamic Integral (21)

B1. Asymptotics Near the Rupture Ends

[135] Since the slip velocity vanishes at the rupture tips, the integral in (21) can be evaluated by parts:

$$\tau(x) = \tau^b - \frac{\bar{\mu}}{2\pi v_r} \int_0^L \frac{dV(x')}{dx'} \ln|x'-x| \ dx'$$

Differentiation of the above in x leads to

$$\frac{d\tau}{dx} = \frac{\bar{\mu}}{2\pi v_r} \int_0^L \frac{dV(x')}{dx'} \frac{dx'}{x'-x} \tag{B1}$$

Since $d\tau/dx = d\tau_f/dx$ along the slipping patch and $d\tau_f/dx$ is bounded (see discussion of (18) in the main text), the well-known inversion of (B1) [*Bilby and Eshelby*, 1968; *Rice*, 1968]

$$\frac{dV(x)}{dx} = -\frac{2v_r}{\pi\bar{\mu}} \int_0^L \sqrt{\frac{x'(L-x')}{x(L-x)}} \frac{d\tau}{dx'} \frac{dx'}{x'-x} \quad (0 < x < L) \tag{B2}$$

allows to find the tip asymptotics of the slip velocity in the form

$$X \to 0^+ : \quad V(x) = v_r \frac{k\sqrt{X}}{\bar{\mu}} \tag{B3}$$

where $X = x$ and $k = k_0$ for the advancing tip asymptote; $X = L - x$ and $k = k_L$ for the trailing tip asymptote; and k's are defined by

$$\{k_0, k_L\} = -\frac{4}{\pi\sqrt{L}} \int_0^L \left\{ \sqrt{\frac{L-x}{x}}, \sqrt{\frac{x}{L-x}} \right\} \frac{d\tau}{dx} dx. \tag{B4}$$

These two coefficients, denoted as the *stress-rate intensity factors*, quantify the strength of a stress-rate tip singularity. The latter can be recovered from analysis of (B1) with (B3), analogous to the classical fracture mechanics treatment [*Muskhelishvili*, 1977; *Rice*, 1968], as follows

$$X \to 0^- : \quad \frac{d\tau}{dx} = \frac{k}{4\sqrt{-X}}. \tag{B5}$$

B2. Inversion and Stress Distribution Constraints

[136] Integration of (B2) in x and subsequent evaluation of the integral in the right hand side by parts results in an inversion of the original elastodynamic equation (16) along the slipping patch, $0 < x < L$:

$$V(x) = -\frac{2}{\pi} \frac{v_r}{\bar{\mu}} \int_0^L \sqrt{\frac{x(L-x)}{x'(L-x')}} \tau(x') \frac{dx'}{x'-x}. \tag{B6}$$

The validity of (B6) as an inversion of (16) hinges upon the vanishing slip velocity at the tips, which, upon revisiting (21), imposes a single constraint on background stress τ^b relative to the stress distribution along the slip pulse,

$$\int_0^L \frac{\tau^b - \tau(x')}{\sqrt{x'(L-x')}} dx' = 0. \tag{B7}$$

We note that for a crack-like rupture (not considered in this work), slip is zero at both tips of the slipping patch (and not just at one of them, as is the case for a pulse), which then requires a constraint additional to (B7) to ensure vanishing slip-rate at both tips [*Rice*, 1968].

B3. Boundary Layer Approximation

[137] Consider a particular solution of the elastodynamic equation (B6) characterized by the negligible stress, $\tau \ll \tau_0$, outside of the immediate vicinity of one of the tips. Without loss of generality, we consider such a boundary layer at the advancing tip, $x = 0$. Equation (B6), rewritten here as

$$\frac{V(x)}{\sqrt{1-x/L}} = -\frac{2}{\pi} \frac{v_r}{\bar{\mu}} \int_0^L \sqrt{\frac{x}{x'}} \frac{\tau(x')}{\sqrt{1-x'/L}} \frac{dx'}{x'-x}, \tag{B8}$$

reduces within the boundary layer, $x \ll L$, to

$$V^{BL}(x) = -\frac{2}{\pi} \frac{v_r}{\bar{\mu}} \int_0^\infty \sqrt{\frac{x}{x'}} \tau^{BL}(x') \frac{dx'}{x'-x} \tag{B9}$$

The superscript "BL" was introduced in (B9) to differentiate its solution, which is applicable within the BL, from the overall solution, which encompasses the entire crack, $0 \le x \le L$. The overall solution affords a simple expression in terms of the BL solution of (B9):

$$V(x) = \sqrt{1-\frac{x}{L}} V^{BL}(x), \quad \tau(x) = \sqrt{1-\frac{x}{L}} \tau^{BL}(x). \tag{B10}$$

[138] Comparing the integral in (B7) to that in (B8) evaluated as $x \to L$, a useful relation between τ^b and L can be established:

$$\tau^b \simeq \frac{1}{2} \frac{\bar{\mu}}{v_r} V^{BL}(L) \tag{B11}$$

[139] Equations (B8)–(B11) are readily adopted to the case of a boundary layer at the trailing tip, $x = L$, by means of a transformation: $x \to L - x$ and $V \to -V$.

Appendix C: Small Slip Considerations for Undrained Pulse

[140] Integration of the linearized equation (27) by parts and subsequent differentiation result in the auxiliary problem:

$$\frac{L}{L_c} \frac{V(x)}{\epsilon V_c} = -\frac{1}{2\pi} \int_0^L \frac{d(V/\epsilon V_c)}{d(x'/L)} \frac{dx'}{x'-x}. \tag{C1}$$

Normalized patch length L/L_c and slip velocity $V(x)/\epsilon V_c$ can be regarded as the eigenvalue and eigenfunction of equation (C1), respectively. A mathematically equivalent eigen problem has been solved by *Uenishi and Rice* [2003], see their Appendix B. They show that there exists an infinite discrete set of positive eigenvalues and corresponding set of alternating even and odd eigen functions. Only a single eigensolution out of this set is non-negative and therefore physically admissible (we consider ruptures with no back-slip). The corresponding eigenvalue is $L/L_c \simeq 1.158$ and the eigenfunction is symmetric about $x = L/2$ and defined up to an arbitrary multiple C by $V(x)/\epsilon V_c = C\, \nu_0(2x/L - 1)$. Normalized function $\nu_0(X)$, $|X| < 1$, is given, to sufficient accuracy, by *Uenishi and Rice* [2003], $\nu_0(X) \simeq (0.925 - 0.308\, X^2)\sqrt{1-X^2}$. To find the prefactor C, we turn to the original equation (27), which suggests that $1 - \delta(x)/(\epsilon\delta_c)$ is anti-symmetric about $x = L/2$ for a symmetric $V(x)$. Consequently, $\delta(L/2) = \delta(L)/2 = \epsilon\delta_c$. Expressing the latter equality in terms of the slip rate leads to a constraint

$$\int_0^L \frac{V(x)}{\epsilon V_c} \frac{dx}{L} = 2, \tag{C2}$$

which evaluation for the above eigensolution yields $C \simeq 3$.

[141] The solution for the normalized slip rate and slip is shown in its finality in Figures 4a and 4b (marked by $T/T^* = 0$). The numerical value of the maximum slip rate (at $x = L/2$) is $V_{max}/\epsilon V_c \simeq 2.775$. We note that this solution can also be obtained directly from (27) using the numerical method of Appendix D.

Appendix D: Solution by Chebyshev Polynomials

[142] Elastodynamic equation (21) lands itself to the solution by means of expansion into a series of the Chebyshev's polynomials [*Erdogan et al.*, 1973]. Upon mapping $\xi = 2(x/L) - 1$ of the slipping patch $x \in (0, L)$ onto $\xi \in (-1, 1)$, a solution of (21), which satisfies the tip asymptotics (B3), is furnished by

$$\frac{V(x)}{V_c} = \sum_{n=1}^{\infty} B_n \sin n\theta, \quad (\theta = \arccos\xi) \tag{D1}$$

$$\frac{\tau(x)}{\tau_0} - \frac{\tau^b}{\tau_0} = -\frac{1}{2L/L_c}\sum_{n=1}^{\infty} B_n \cos n\theta \tag{D2}$$

where B_n are arbitrary expansion coefficients. The corresponding expression for the normalized slip follows from integration of (D1):

$$\frac{\delta(x)}{\delta_c} = \frac{B_1}{4}\left(\frac{\sin 2\theta}{2} + \pi - \theta\right) + \sum_{n=2}^{\infty}\frac{B_n}{4}\left(\frac{\sin(n+1)\theta}{n+1} - \frac{\sin(n-1)\theta}{n-1}\right). \tag{D3}$$

[143] Using (D1) and (D2) to evaluate τV, and substituting the result for $\tau_f V$ under the integral in the fault constitutive equation (23) leads to

$$1 - \frac{\tau_f(x)}{\tau_0} = \frac{\tau^b}{\tau_0}\sum_{n=1}^{\infty} B_n \psi_n\left(\xi, \frac{T}{T_*}\right) - \frac{1}{2L/L_c}\sum_{n,m=1(n\geq m)}^{\infty} B_n B_m \psi_{n+m}\left(\xi, \frac{T}{T_*}\right), \tag{D4}$$

where

$$\psi_n\left(\xi, \frac{T}{T_*}\right) \equiv \frac{1}{2}\int_{-1}^{\xi} \sin n\theta' \; \mathcal{K}\left(\frac{T}{T^*}\frac{\xi - \xi'}{2}; \frac{\alpha_{hy}}{\alpha_{th}}\right) d\xi', \tag{D5}$$

and $\theta' = \arccos \xi'$. We note that, apart from the undrained case, see (D7) below, functions ψ_n (ξ, T/T^*) have to be evaluated numerically.

[144] Corresponding expressions for the stress-rate intensity factors, (B4), can be evaluated as

$$\frac{\{k_0, k_L\}}{\tau_0/\sqrt{L}} = \frac{2}{L/L_c}\sum_{n=1}^{\infty}\{(-1)^n, 1\} n B_n. \tag{D6}$$

[145] Equating series expansions for τ, (D2), and τ_f, (D4), truncated to the first N terms, and evaluating the result at $N + 1$ collocation points ξ_k ($k = 1, .., N + 1$), $\cos((N + 1)\theta(\xi_k)) = 0$, along the patch yields the system of $N + 1$ algebraic equations. The latter is solved numerically for the patch L/L_c and expansion coefficients $B_1, .., B_N$. The resulting numerical solution is parameterized by the slip duration T/T^*, the background stress τ^b/τ_0, and the diffusivity ratio α_{hy}/α_{th}.

[146] Further notes on implementation of the numerical method for particular cases considered in this study are as follows.

[147] 1. In the undrained limit ($T/T^* \to 0$), the convolution kernel is $\mathcal{K}(0) = 1$, and functions ψ_n, (D5), in the strength's expansion (D4) are evaluated analytically:

$$\psi_n(\xi, 0) = \begin{cases} \frac{1}{4}\left(\xi\sqrt{1-\xi^2} + \pi - \theta\right), & n = 1 \\ \frac{1}{2(n^2-1)}\left(n\sqrt{1-\xi^2}\cos n\theta - \xi \sin n\theta\right), & n > 1 \end{cases} \tag{D7}$$

The numerical solution is carried out in the range of $\tau^b/\tau_0 \in [0.03, 0.99]$ with $N = 56$ terms in the truncated series. When τ^b/τ_0 is not small (>0.1), only few terms ($N = 2$ to 10) in the series result in a sufficiently accurate solution, see the plot of an integral measure $\mathcal{E} = ((\tau_0 - \tau^b)L)^{-1}\sqrt{\int_0^L (\tau - \tau_f)^2 dx}$ of the numerical error as a function of τ^b/τ_0 for various N in Figure D1a. The quality of the numerical solution degenerates with the decreasing τ^b/τ_0 due to the increasing localization of the slip rate and of the stress gradient into a small region near the rupture edge, Figures 6a and 6e; and therefore an increasing number of terms N is required to maintain the accuracy of the numerical solution. This underscores the importance of the large-slip asymptotic solution (section 6) which can be evaluated for arbitrarily small τ^b/τ_0.

[148] 2. In the self-healing, partially-drained slip limit, the solution is obtained as a subset of the general solution by invoking the intrinsic healing condition, $k_L = 0$, with k_L given by (D6). The numerical solution is obtained in the range of $\tau^b/\tau_0 \in [0.06, 0.99]$ using $N = 76$ terms in the truncated series. A similar deterioration of the numerical accuracy with decreasing τ^b/τ_0 is observed, where an accurate solution requires only a few terms in the series for moderate values of τ^b/τ_0, and up to the maximum number used here, $N = 76$, when τ^b/τ_0 drops below 0.1 (Figure D1b).

[149] 3. In the small slip limit ($\epsilon = (\tau_0 - \tau^b)/\tau_0 \ll 1$), the normalized slip rate V/V_c and its expansion (D1) coefficients B_n are $O(\epsilon)$. Consequently, the 2nd sum in the strength expansion (D4) is negligible, $O(\epsilon^2)$. Dividing the stress (D2) and the linearized strength expansions through ϵ, we have

$$\frac{\tau(x) - \tau^b}{\tau_0 - \tau^b} = -\frac{1}{2L/L_c}\sum_{n=1}^{\infty}\frac{B_n}{\epsilon}\cos n\theta \tag{D8}$$

$$1 - \frac{\tau_f(x) - \tau^b}{\tau_0 - \tau^b} = \sum_{n=1}^{\infty}\frac{B_n}{\epsilon}\psi_n\left(\xi, \frac{T}{T_*}\right) \tag{D9}$$

Numerical solution for L/L_c and the scaled coefficients B_n/ϵ in truncated series (D8) and (D9) follows the same path as in the general case, and is carried out in the range of T/T_* between zero and the maximum value corresponding to the self-healing limit, using $N = 22$ terms in the truncated series. We note that a sufficiently accurate solution requires between $N = 2$ to 5 terms in the entire range of T/T_* (with the largest N in the case of self-healing pulse). In the case of self-healing pulse, first five expansion coefficients are

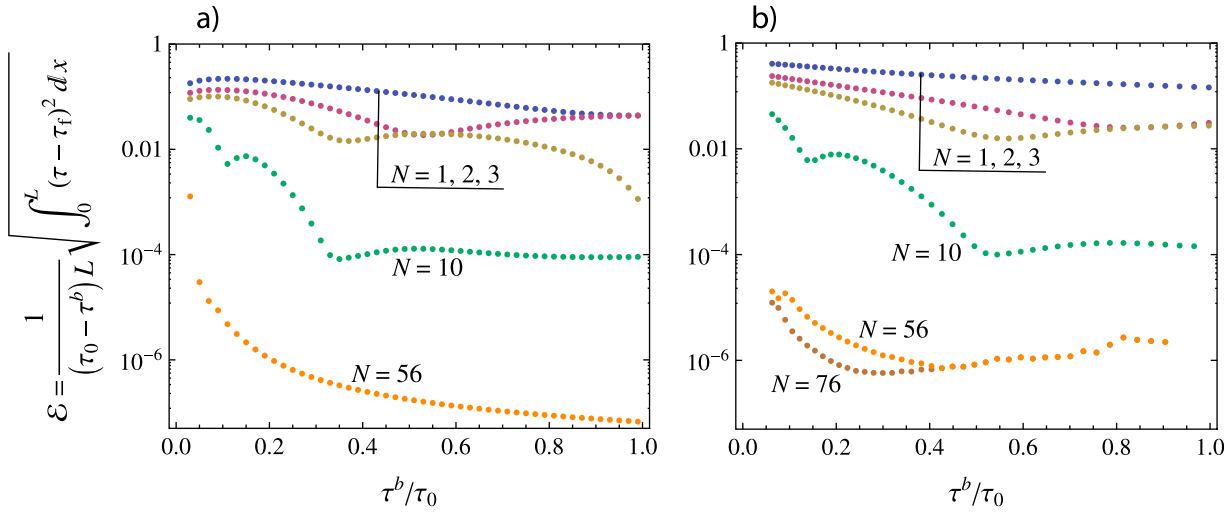

Figure D1. A measure $\mathcal{E}$ of the numerical error in (a) the undrained pulse and (b) the partially-drained, self-healing pulse with $\alpha_{hy} = \alpha_{th}$ solutions as a function of the background stress τ^b/τ_0, for various number N of terms in the truncated Chebyshev series (D1)–(D4).

$B_{0,\dots,4}/\epsilon$ = {3.660, −4.981, −0.308, 2.527, −0.917} and {3.805, −5.628, 0.307, 2.781, −1.316} when α_{hy}/α_{th} = 1 and 0 or ∞, respectively.

Appendix E: Non-Existence of a Slip Pulse on a Plane With a Constant Friction

[150] We show here that existence of a slip pulse on a plane (the thickness h of the shear zone is neglected) with a constant friction would require backslip ($V < 0$) near the trailing edge of the rupture.

[151] Integrating constitutive equation (12) by parts and differentiating the result in time $t = x/v_r$ leads to:

$$\frac{d\tau_f}{dx} = -\frac{\sqrt{L}}{\delta^*}\frac{1}{v_r}\int_0^x \frac{d(\tau_f V)}{dx'}\frac{dx'}{\sqrt{\pi(x-x')}}.$$

Substituting $d\tau_f/dx$ for $d\tau/dx$ in (B4) and changing the order of integration in the resulting double integral, we obtain an expression for the stress-rate intensity factor at the trailing edge, as follows

$$k_L = \frac{4}{\pi\delta^* v_r}\int_0^L \frac{d(\tau_f V)}{dx'}dx' \int_{x'}^L \sqrt{\frac{x}{L-x}}\frac{dx}{\sqrt{\pi(x-x')}}.$$

Carrying out the integration in x and then integrating by parts in x' leads to the final expression

$$k_L = -\frac{4}{\pi^{3/2}\delta^*\sqrt{L}v_r}\int_0^L \tau_f(x')V(x')\Phi(1-x'/L)dx',$$

where $\Phi(\xi) \equiv (\boldsymbol{K}(\xi) - \boldsymbol{E}(\xi))/\xi$, and $\boldsymbol{K}$ and $\boldsymbol{E}$ are the complete elliptic integrals of the first and second kind, respectively [*Abramowitz and Stegun*, 1964]. Function $\Phi(\xi)$ is positive for all $\xi \in [0, 1]$ and the shear heating rate $\tau_f V$ is non-negative. Thus, $k_L < 0$ and the slip rate near the trailing edge, $V(x) \sim v_r(k_L/\bar{\mu})\sqrt{L-x}$, (B3), is negative.

Appendix F: Large Slip Considerations

F1. Boundary Layer at the Advancing Tip

[152] The method of solution relies on the inversion (B9) of the BL elastodynamic equation (30). Using the scaling (32), this inversion can be written in the normalized form

$$\tilde{V}(\tilde{x}) = -\frac{2}{\pi}\int_0^\infty \sqrt{\frac{\tilde{x}}{s}}\frac{\tilde{\tau}(s)ds}{s-\tilde{x}} \quad \text{with} \quad \tilde{x} = \frac{x}{L_c}. \tag{F1}$$

Integrating (F1) by parts, we obtain

$$\tilde{V}(\tilde{x}) = -\frac{2}{\pi}\int_0^\infty \ln\left|\frac{\sqrt{\tilde{x}}+\sqrt{s}}{\sqrt{\tilde{x}}-\sqrt{s}}\right|\frac{d\tilde{\tau}}{ds}ds, \tag{F2}$$

and the near field asymptote of the slip rate,

$$\tilde{x}\to 0 : \tilde{V}(\tilde{x}) = \tilde{k}_0\sqrt{\tilde{x}}, \quad \tilde{k}_0 \equiv -\frac{4}{\pi}\int_0^\infty \frac{d\tilde{\tau}(s)}{ds}\frac{ds}{\sqrt{s}}. \tag{F3}$$

We note that this asymptote can be obtained directly from the tip asymptotics of the finite crack (B3) and (B4) by evaluating expression (B4) for k_0 in the limit $L \to \infty$ and using the scaling (32). As the result, $\tilde{k}_0$, as defined in (F3), attains the meaning of the normalized stress-rate intensity factor at the advancing tip, $\tilde{k}_0 = k_0\sqrt{L_c}/\tau_0$.

[153] We now seek numerical solution for $\tilde{V}(\tilde{x})$ and $d\tilde{\tau}/d\tilde{x}$ governed by the elastodynamics equation (F2) and the following reduction of the undrained constitutive law,

$$\tilde{V}(\tilde{x}) = -\frac{1}{\tilde{\tau}(\tilde{x})}\frac{d\tilde{\tau}}{d\tilde{x}}, \quad \text{with} \quad \tilde{\tau}(\tilde{x}) = 1 + \int_0^x \frac{d\tilde{\tau}}{d\tilde{x}}d\tilde{x}, \tag{F4}$$

obtained from the differentiation of $\tilde{\tau}(\tilde{x}) = \exp(-\tilde{\delta}(\tilde{x}))$, (24) in scaling (32), and the use of $\tilde{V}(\tilde{x}) = d\tilde{\delta}/d\tilde{x}$, (31).

[154] Let us consider a discretization of the semi-infinite crack into $n+1$ elements, $0=\tilde{x}_1<\ldots<\tilde{x}_{n+1}<\tilde{x}_{n+2}=\infty$. A piece-wise constant approximation for the stress rate is adopted over the intermediate elements, $d\tilde{\tau}/d\tilde{x}=\tilde{\tau}'_j$, $\tilde{x}\in(\tilde{x}_j,\tilde{x}_{j+1})$, $j=2,..,n$; while the near-field, $d\tilde{\tau}/d\tilde{x}=-\tilde{k}_0\sqrt{\tilde{x}}$, and the far-field, $d\tilde{\tau}/d\tilde{x}\simeq 0$ (exponentially small), asymptotes are used in the bounding elements, $(0,\tilde{x}_2)$ and $(\tilde{x}_{n+1},\infty)$, respectively. Evaluation of the corresponding approximations of (F2),

$$\tilde{V}(\tilde{x})=-\tilde{k}_0 C_1(\tilde{x})+\sum_{j=2}^{n}\tilde{\tau}'_j C_j(\tilde{x}) \tag{F5}$$

with

$$C_j(\tilde{x})\equiv-\frac{2}{\pi}\int_{\tilde{x}_j}^{\tilde{x}_{j+1}}\ln\left|\frac{\sqrt{\tilde{x}}+\sqrt{s}}{\sqrt{\tilde{x}}-\sqrt{s}}\right|\left\{\begin{array}{ll}\sqrt{s}, & j=1\\ 1, & j>1\end{array}\right\}ds,$$

and (F4), respectively, at a set of points $\tilde{x}_{i+1/2}$ within the intermediate elements $(\tilde{x}_i,\tilde{x}_{i+1})$, $i=2,..,n$, results in a set of $n-1$ algebraic equations in terms of the unknown values of the stress-rate $\tilde{\tau}'_2,..,\tilde{\tau}'_n$.

[155] We used $\tilde{x}_2=0.001$, $\tilde{x}_{n+1}=100$, $n=201$, logarithmic ($\log_{10}$) spacing of nodes $\tilde{x}_i$ $(2<i<n+1)$, and $\tilde{x}_{i+1/2}\equiv\sqrt{\tilde{x}_i\tilde{x}_{i+1}}$ to obtain $\tilde{k}_0\simeq 1.848$, (F3), and the normalized distributions of the slip rate, slip, and stress shown in Figure 9. Additional calculations with the increased density of grid points and/or different thresholds $\tilde{x}_2$ and $\tilde{x}_{n+1}$ of the asymptotic regions show that the reported solution is accurate to at least four significant digits.

F2. Boundary Layer at the Trailing Tip

[156] Similarly to the advancing tip considerations (section F1), the method of solution in the trailing tip boundary layer relies on the inversion of the corresponding elastodynamic equation (45). This inversion is obtained from (B6) by evoking the transformation $x\rightarrow L-x$, $V^{\mathrm{BL}}\rightarrow-\Delta V^{\mathrm{BL}}$, and $\tau^{\mathrm{BL}}\rightarrow\Delta\tau^{\mathrm{BL}}$ (see section B3), and is written in the normalized form

$$\Delta\hat{V}(\hat{X})=\frac{2}{\pi}\int_0^\infty\sqrt{\frac{\hat{X}}{s}}\frac{\Delta\hat{\tau}(s)ds}{s-\hat{X}}\quad\text{with}\quad\hat{X}=\frac{L-x}{(L/L_c)^{-1/3}L}, \tag{F6}$$

where the normalized perturbations $\Delta\hat{V}$ and $\Delta\hat{\tau}$ are defined in (47) and (48).

[157] The normalized form of the BL approximation of the fault constitutive law, (46), is given by

$$\hat{T}=\Delta\hat{\tau}\left(2\sqrt{\hat{X}/\pi}+\Delta\hat{V}\right)-\frac{d\Delta\hat{\tau}}{d\hat{X}}, \tag{F7}$$

where $\hat{T}\equiv\kappa(L/L_c)^{1/3}\,T/T^*$ is the normalized slip duration.

[158] The near field asymptote of $\Delta\hat{V}$ is recovered from (F6), after integrating it by parts and passing to the limit $\hat{X}\rightarrow 0$,

$$\hat{X}\rightarrow 0:\Delta\hat{V}=\Delta\hat{k}_L\sqrt{\hat{X}},\quad\Delta\hat{k}_L\equiv\frac{4}{\pi}\int_0^\infty\frac{d\Delta\hat{\tau}}{ds}\frac{ds}{\sqrt{s}} \tag{F8}$$

Here $\Delta\hat{k}_L=\Delta k_L\,L/(\tau_0\sqrt{L_c})$ is the normalized perturbation of the stress-rate intensity factor $k_L=k_L^{und}+\Delta k_L$ at the trailing tip. Evaluating the self-healing condition ($k_L=0$) in the normalized form, we find

$$2/\sqrt{\pi}+\Delta\hat{k}_L=0 \tag{F9}$$

The near field asymptotics of the constitutive law (F7) with (F8) and (F9) is

$$\hat{X}\rightarrow 0:\frac{d\Delta\hat{\tau}}{d\hat{X}}=-\hat{T}. \tag{F10}$$

[159] The far field asymptotics of the BL solution can be obtained (see section F3) in the form

$$\hat{X}\rightarrow\infty:\Delta\hat{\tau}=\frac{\hat{T}}{2\sqrt{\hat{X}/\pi}}+O\left(\frac{\ln\hat{X}}{\hat{X}^{3/2}}\right),\quad\Delta\hat{V}=-\hat{T}\frac{\ln\hat{X}}{\sqrt{\pi\hat{X}}}+\frac{B}{\sqrt{\hat{X}}}. \tag{F11}$$

[160] For the numerical solution of the BL equations at the trailing tip, (F6) and (F7), we use a modification of the method applied to the BL at the advancing tip in section F1. Specifically, the numerical treatment of equation (F6) is identical to that of (F1) upon a transformation ($\hat{X}\rightarrow\tilde{x}$, $\Delta\hat{V}\rightarrow-\tilde{V}$, and $\Delta\hat{\tau}\rightarrow\tilde{\tau}$) and the use of the appropriate set of the near and far field asymptotics, (F11). Upon discretization of the semi-infinite crack in $n+1$ elements, $0=\hat{X}_1<\ldots<\hat{X}_{n+1}<\hat{X}_{n+2}=\infty$, we adopt a piece-wise constant approximation for the stress-rate perturbation in the intermediate elements, $d\Delta\hat{\tau}/d\hat{X}=\Delta\hat{\tau}'_j$ with $\hat{X}$ from $(\hat{X}_j,\hat{X}_{j+1})$ and $j=2,..,n$; and use the near-field, $d\Delta\hat{\tau}/d\hat{X}=-\hat{T}$, and the far-field, $d\Delta\hat{\tau}/d\hat{X}=-(\sqrt{\pi}/4)\,\hat{T}\,\hat{X}^{-3/2}$, approximations in the bounding elements $(0,\hat{X}_2)$ and $(\hat{X}_{n+1},\infty)$, respectively. Integrating (F6) by parts and using the stress-rate approximation, we have

$$\Delta\hat{V}(\hat{X})=-\hat{T}\;C_1(\hat{X})+\sum_{j=2}^{n}\Delta\hat{\tau}'_j\;C_j(\hat{X})-\frac{\sqrt{\pi}}{4}\hat{T}\;C_{n+1}(\hat{X}) \tag{F12}$$

with

$$C_j(\hat{X})\equiv\frac{2}{\pi}\int_{\hat{X}_j}^{\hat{X}_{j+1}}\ln\left|\frac{\sqrt{\hat{X}}+\sqrt{s}}{\sqrt{\hat{X}}-\sqrt{s}}\right|\left\{\begin{array}{ll}1, & j<n+1\\ s^{-3/2}, & j=n+1\end{array}\right\}ds.$$

[161] Using (F12) and the approximation of $\Delta\hat{\tau}(\hat{X})=-\int_{\hat{X}}^{\infty}(d\Delta\hat{\tau}/d\hat{X})d\hat{X}$ to evaluate (F7) at a set sample points $\hat{X}_{i+1/2}\in(\hat{X}_i,\hat{X}_{i+1})$, $i=2,..,n$, we obtain a system of $n-1$ algebraic equations, which, when complimented by the self-healing condition (F9), $\Delta\hat{k}_L=-2/\sqrt{\pi}$, with $\Delta\hat{k}_L$ evaluated from (F8), allows to solve for the n unknowns $\Delta\hat{\tau}'_2,..,\Delta\hat{\tau}'_n$, and $\hat{T}$, respectively.

[162] We use $\hat{X}_2=0.001$, $\hat{X}_{n+1}=1000$, $n=201$, the logarithmic ($\log_{10}$) spacing of nodes $\hat{X}_i$ $(2<i<n+1)$, and $\hat{X}_{i+1/2}\equiv(\hat{X}_i\hat{X}_{i+1})^{1/2}$ to obtain the following solution (with the four

significant digits of precision): $\hat{T} \simeq 0.3727$, $\Delta\hat{\tau}(0) \simeq 0.7584$, $B \simeq -1.009$, (F14), and the normalized distributions shown in Figure 10.

F3. Derivation of (F11)

[163] The leading term in the $\Delta\hat{\tau}$-expansion, (F11), follows from (F7) and the requirement of vanishing $\Delta\hat{V}$ and $d\Delta\hat{\tau}/d\hat{X}$ away from the trailing tip.

[164] In order to establish the leading term in the $\Delta\hat{V}$-expansion, (F11), let us decompose the elasticity integral (F6) into the two integrals over a finite $(0, \hat{X}_*)$ and an infinite $(\hat{X}_*, \infty)$ range, respectively, with large enough $\hat{X}_*$, so that the approximation $\Delta\hat{\tau} \simeq (\sqrt{\pi}/2)\hat{T}/\sqrt{\hat{X}}$ holds for all $\hat{X}$ from $(\hat{X}_*, \infty)$. Evaluating the integrals in the said decomposition for $\hat{X} \gg \hat{X}_*$ we have

$$\Delta\hat{V}(\hat{X}) \simeq -\frac{2}{\pi}\left(\int_0^{X_*} \frac{\Delta\hat{\tau}(s)ds}{\sqrt{s}}\right)\frac{1}{\sqrt{\hat{X}}} - \hat{T}\frac{\ln(\hat{X}/\hat{X}_*)}{\sqrt{\pi\hat{X}}}.$$

This establishes the leading asymptotic term in the $\Delta\hat{V}$-expansion, (F11), and suggests the form of the next term.

[165] In order to establish the next term in the $\Delta\hat{V}$-expansion, we first notice that

$$\int_0^\infty \sqrt{\frac{\hat{X}}{s}}\frac{\sqrt{s}}{1+s}\frac{ds}{s-\hat{X}} = -\frac{\sqrt{\hat{X}}}{1+\hat{X}}\ln\hat{X} = -\frac{\ln\hat{X}}{\sqrt{\hat{X}}} + O\left(\frac{\ln\hat{X}}{\hat{X}^{3/2}}\right).$$

Thus, for $\hat{X} \gg 1$, we can establish

$$\Delta\hat{V}(\hat{X}) = -\hat{T}\frac{\ln\hat{X}}{\sqrt{\pi\hat{X}}} + \frac{2}{\pi}\int_0^\infty \sqrt{\frac{\hat{X}}{s}}\left(\Delta\hat{\tau}(s) - \frac{\sqrt{\pi}\hat{T}}{2}\frac{\sqrt{s}}{1+s}\right)\frac{ds}{s-\hat{X}} + O\left(\frac{\ln\hat{X}}{\hat{X}^{3/2}}\right). \tag{F13}$$

The latter integral's asymptotic expression $= B/\sqrt{\hat{X}}$ with

$$B = -\frac{2}{\pi}\int_0^\infty \left(\frac{\Delta\hat{\tau}(s)}{\sqrt{s}} - \frac{\sqrt{\pi}}{2}\hat{T}\frac{1}{1+s}\right)ds. \tag{F14}$$

The integral in (F14) is converging based on the asymptotic behavior of the integrand, which is $O(1/\sqrt{s})$ for $s \to 0$ and $o(1/s)$ for $s \to \infty$.

[166] **Acknowledgments.** The support for this research by the National Science Foundation (grant EAR-1036985) and by the Natural Science and Engineering Research Council of Canada (Discovery Grant 371606) is acknowledged. Thanks to Jim Rice for discussions of the results of these studies, to him and Robert Viesca for constructive comments on a draft of the text, and to Dan Faulkner, Paul Segall, and anonymous reviewer for helpful comments.

References

Abercrombie, R. E., and J. R. Rice (2005), Can observations of earthquake scaling constrain slip weakening?, *Geophys. J. Int.*, *162*, 406–424, doi:10.1111/j.1365-246X.2005.02579.x.

Abramowitz, M., and I. A. Stegun (Eds.) (1964), *Handbook of Mathematical Functions With Formulas, Graphs, and Mathematical Tables*, *Appl. Math. Ser.*, vol. 55, U.S. Gov. Print. Off., Washington, D. C.

Andrews, D. J. (2002), A fault constitutive relation accounting for thermal pressurization of pore fluid, *J. Geophys. Res.*, *107*(B12), 2363, doi:10.1029/2002JB001942.

Andrews, D. J., and Y. Ben-Zion (1997), Wrinkle-like slip pulse on a fault between different materials, *J. Geophys. Res.*, *102*(B1), 553–571.

Asano, K., and T. Iwata (2006), Source process and near-source ground motions of the 2005 West Off Fukuoka Prefecture earthquake, *Earth Planets Space*, *58*, 93–98.

Asano, K., T. Iwata, and K. Irikura (2005), Estimation of source rupture process and strong ground motion simulation of the 2002 Denali, Alaska, earthquake, *Bull. Seismol. Soc. Am.*, *95*(5), 1701–1715, doi:10.1785/0120040154.

Audet, P., M. G. Bostock, N. I. Christensen, and S. M. Peacock (2009), Seismic evidence for overpressured subducted oceanic crust and megathrust fault sealing, *Nature*, *457*, 76–78, doi:10.1038/nature07650.

Avouac, J.-P., F. Ayoub, S. Leprince, O. Konca, and D. V. Helmberger (2006), The 2005, Mw 7.6 Kashmir earthquake: Sub-pixel correlation of ASTER images and seismic waveforms analysis, *Earth Planet. Sci. Lett.*, *249*, 514–528, doi:10.1016/j.epsl.2006.06.025.

Beeler, N. M., and T. E. Tullis (1996), Self-healing pulse in dynamic rupture models due to velocity-dependent strength, *Bull. Seismol. Soc. Am.*, *86*, 1130–1148.

Beeler, N. M., T. E. Tullis, and D. L. Goldsby (2008), Constitutive relationships and physical basis of fault strength due to flash heating, *J. Geophys. Res.*, *113*, B01401, doi:10.1029/2007JB004988.

Beroza, G. C., and P. Spudich (1988), Linearized inversion for fault rupture behavior: Application to the 1984 Morgan Hill, California, earthquake, *J. Geophys. Res.*, *93*(B6), 6275–6296.

Bilby, B., and J. Eshelby (1968), Dislocations and the theory of fracture, in *Fracture, an Advanced Treatise*, vol. I, edited by H. Liebowitz, chap. 2, pp. 99–182, Academic, New York.

Bizzarri, A., and M. Cocco (2006a), A thermal pressurization model for the spontaneous dynamic rupture propagation on a three-dimensional fault: 1. Methodological approach, *J. Geophys. Res.*, *111*, B05303, doi:10.1029/2005JB003862.

Bizzarri, A., and M. Cocco (2006b), A thermal pressurization model for the spontaneous dynamic rupture propagation on a three-dimensional fault: 2. Traction evolution and dynamic parameters, *J. Geophys. Res.*, *111*, B05304, doi:10.1029/2005JB003864.

Blanpied, M. L., D. A. Lockner, and J. D. Byerlee (1991), Fault stability inferred from granite sliding experiments at hydrothermal conditions, *Geophys. Res. Lett.*, *18*(4), 609–612.

Blanpied, M. L., C. J. Marone, D. A. Lockner, J. D. Byerlee, and D. P. King (1998), Quantitative measure of the variation in fault rheology due to fluid-rock interactions, *J. Geophys. Res.*, *103*, 9691–9712.

Borcherdt, R. D., M. J. S. Johnston, G. Glassmoyer, and C. Dietel (2006), Recordings of the 2004 Parkfield earthquake on the General Earthquake Observation System array: Implications for earthquake precursors, fault rupture, and coseismic strain changes, *Bull. Seismol. Soc. Am.*, *96*(4B), S73–S89, doi:10.1785/0120050827.

Boullier, A.-M., E.-C. Yeh, S. Boutareaud, S.-R. Song, and C.-H. Tsai (2009), Microscale anatomy of the 1999 Chi-Chi earthquake fault zone, *Geochem. Geophys. Geosyst.*, *10*, Q03016, doi:10.1029/2008GC002252.

Brantut, N., A. Schubnel, J.-N. Rouzaud, F. Brunet, and T. Shimamoto (2008), High-velocity frictional properties of a clay-bearing fault gouge and implications for earthquake mechanics, *J. Geophys. Res.*, *113*, B10401, doi:10.1029/2007JB005551.

Broberg, K. B. (1999), *Cracks and Fracture*, Academic, San Diego, Calif.

Brune, J. N., T. L. Henyey, and R. F. Roy (1969), Heat flow, stress, and rate of slip along the San Andreas fault, California, *J. Geophys. Res.*, *74*(15), 3821–3827.

Byerlee, J. (1978), Friction of rocks, *Pure Appl. Geophys.*, *116*, 615–626.

Carslaw, H., and J. C. Jaeger (1959), *Conduction of Heat in Solids*, 2nd ed., Oxford Univ. Press, Oxford, U. K.

Chester, F. M., and J. S. Chester (1998), Ultracataclasite structure and friction processes of the Punchbowl fault, San Andreas system, California, *Tectonophysics*, *295*, 199–221.

Chester, F. M., J. S. Chester, D. L. Kirschner, S. E. Schulz, and J. P. Evans (2004), Structure of large-displacement, strike-slip fault zones in the brittle continental crust, in *Rheology and Deformation in the Lithosphere at Continental Margins*, edited by G. D. Karner et al., pp. 199–221, Columbia Univ. Press, New York.

Cocco, M., and E. Tinti (2008), Scale dependence in the dynamics of earthquake propagation: Evidence from seismological and geological observations, *Earth Planet. Sci. Lett.*, *273*, 123–131, doi:10.1016/j.epsl.2008.06.025.

Cochard, A., and R. Madariaga (1994), Dynamic faulting under rate-dependent friction, *Pure Appl. Geophys.*, *142*, 419–445.

Custodio, S., M. T. Page, and R. J. Archuleta (2009), Constraining earthquake source inversions with GPS data: 2. A two-step approach to combine seismic and geodetic data sets, *J. Geophys. Res.*, *114*, B01315, doi:10.1029/2008JB005746.

Day, S. M. (1982), Three-dimensional finite difference simulation of fault dynamics: Rectangular faults with fixed rupture velocity, *Bull. Seismol. Soc. Am.*, *72*, 705–727.

De Paola, N., T. Hirose, T. Mitchell, G. Di Toro, C. Viti, and T. Shimamoto (2011), Fault lubrication and earthquake propagation in thermally unstable rocks, *Geology*, *39*(1), 35–38, doi:10.1130/G31398.1.

Di Toro, G., R. Han, T. Hirose, N. De Paola, S. Nielsen, K. Mizoguchi, F. Ferri, M. Cocco, and T. Shimamoto (2011), Fault lubrication during earthquakes, *Nature*, *471*, 494–498, doi:10.1038/nature09838.

Dieterich, J. (1979), Modeling of rock friction: 1. Experimental results and constitutive equations, *J. Geophys. Res.*, *84*(15), 2161–2168.

Dieterich, J. H. (1992), Earthquake nucleation on faults with rate- and state-dependent strength, *Tectonophysics*, *211*, 115–134.

Dragert, H., K. Wang, and T. S. James (2001), A silent slip event on the deeper Cascadia subduction interface, *Science*, *292*, 1525–1528.

Dragert, H., K. Wang, and G. Rogers (2004), Geodetic and seismic signatures of episodic tremor and slip in the northern Cascadia subduction zone, *Earth Planets Space*, *56*, 1143–1150.

Erdogan, F., G. D. Gupta, and T. S. Cook (1973), Numerical solution of singular integral equations, in *Mechanics of Fracture*, vol. 1, edited by G. C. Sih, chap. 7, pp. 368–425, Noordhoff Int., Leyden, Netherlands.

Faulkner, D. R., and E. H. Rutter (2000), Comparison of water and argon permeability in natural clay-bearing fault gouge under high pressure at 20°C, *J. Geophys. Res.*, *105*, 16,415–16,427.

Freund, L. B. (1979), The mechanics of dynamic shear crack propagation, *J. Geophys. Res.*, *84*, 2199–2209.

Garagash, D. I., D. G. Schaeffer, and J. W. Rudnicki (2005), Effect of rate dependence in shear heating of a fluid-saturated fault zone, in *Poromechanics—Biot Centennial*, edited by Y. Abousleiman, A. H.-D. Cheng, and F. Ulm, pp. 789–794, Taylor and Francis, London.

Hacker, B. R., S. M. Peacock, G. A. Abers, and S. D. Holloway (2003), Subduction factory: 2. Are intermediate-depth earthquakes in subducting slabs linked to metamorphic dehydration reactions?, *J. Geophys. Res.*, *108*(B1), 2030, doi:10.1029/2001JB001129.

Hartzell, S. H. (1989), Comparison of seismic waveform inversion results for the rupture history of a finite fault: Application to the 1986 North Palm Springs, California, earthquake, *J. Geophys. Res.*, *94*(B6), 7515–7534.

Hartzell, S. H., and T. H. Heaton (1983), Inversion of strong ground motion and teleseismic waveform data for the fault rupture history of the 1979 Imperial Valley, California, earthquake, *Bull. Seismol. Soc. Am.*, *73*(6A), 1553–1583.

Hartzell, S. H., and T. H. Heaton (1986), Rupture history of the 1984 Morgan Hill, California, earthquake from the inversion of strong motion records, *Bull. Seismol. Soc. Am.*, *76*(3), 649–674.

He, C., W. Yao, Z. Wang, and Y. Zhou (2007), Strength and stability of frictional sliding of gabbro gouge at elevated temperatures, *Tectonophysics*, *427*, 217–229, doi:10.1016/j.tecto.2006.05.023.

Heaton, T. H. (1982), The 1971 San Fernando earthquake: A double event?, *Bull. Seismol. Soc. Am.*, *72*(6), 2037–2062.

Heaton, T. H. (1990), Evidence for and implications of self-healing pulses of slip in earthquake rupture, *Phys. Earth Planet. Inter.*, *64*, 1–20.

Hernandez, B., M. Cocco, F. Cotton, S. Stramondo, O. Scotti, F. Courboulex, and M. Campillo (2004), Rupture history of the 1997 Umbria-Marche (central Italy) main shocks from the inversion of GPS, DInSAR and near field strong motion data, *Ann. Geophys.*, *47*(4), 1355–1376.

Hirose, T., and M. Bystricky (2007), Extreme dynamic weakening of faults during dehydration by coseismic shear heating, *Geophys. Res. Lett.*, *34*, L14311, doi:10.1029/2007GL030049.

Hyndman, R. D., and S. M. Peacock (2003), Serpentinization of the forearc mantle, *Earth Planet. Sci. Lett.*, *212*, 417–432, doi:10.1016/S0012-821X(03)00263-2.

Ida, Y. (1972), Cohesive force across the tip of a longitudinal-shear crack and Griffith's specific surface energy, *J. Geophys. Res.*, *77*, 3796–3805.

Ji, C., D. J. Wald, and D. V. Helmberger (2002), Source description of the 1999 Hector Mine, California, earthquake, part II: Complexity of slip history, *Bull. Seismol. Soc. Am.*, *92*(4), 1208–1226.

Johnson, E. (1990), On the initiation of unilateral slip, *Geophys. J. Int.*, *101*, 125–132.

Kodaira, S., T. Iidaka, A. Kato, J.-O. Park, T. Iwasaki, and Y. Kaneda (2004), High pore fluid pressure may cause silent slip in the Nankai trough, *Science*, *304*, 1295–1298, doi:10.1126/science.1096535.

Kohli, A. H., D. L. Goldsby, G. Hirth, and T. Tullis (2011), Flash weakening of serpentinite at near-seismic slip rates, *J. Geophys. Res.*, *116*, B03202, doi:10.1029/2010JB007833.

Konca, O., V. Hjorleifsdottir, T.-R. A. Song, J.-P. Avouac, D. V. Helmberger, C. Ji, K. Sieh, R. Briggs, and A. Meltzner (2007), Rupture kinematics of the 2005 Mw 8.6 Nias–Simeulue earthquake from the joint inversion of seismic and geodetic data, *Bull. Seismol. Soc. Am.*, *97*(1A), S307–S322, doi:10.1785/0120050632.

Konca, O., et al. (2008), Partial rupture of a locked patch of the Sumatra megathrust during the 2007 earthquake sequence, *Nature*, *456*, 631–635, doi:10.1038/nature07572.

Kostrov, B. V., and L. V. Nikitin (1970), Some general problems of mechanics of brittle fracture, *Arch. Mech. Stosow.*, *22*, 749–775.

Lachenbruch, A. H. (1980), Frictional heating, fluid pressure, and the resistance to fault motion, *J. Geophys. Res.*, *85*, 6097–6112.

Lachenbruch, A. H., and J. H. Sass (1980), Heat flow and energetics of the San Andreas fault zone, *J. Geophys. Res.*, *85*(B11), 6185–6223.

Lapusta, N., and J. R. Rice (2003a), Nucleation and early seismic propagation of small and large events in a crustal earthquake model, *J. Geophys. Res.*, *108*(B4), 2205, doi:10.1029/2001JB000793.

Lapusta, N., and J. R. Rice (2003b), Low-heat and low-stress fault operation in earthquake models of statically strong but dynamically weak faults, *Eos Trans. AGU*, *84*(46), Fall Meet. Suppl., Abstract S51B-02.

Lee, T. C., and P. T. Delaney (1987), Frictional heating and pore pressure rise due to a fault slip, *Geophys. J. R. Astron. Soc.*, *88*(3), 569–591.

Liu, H.-L., and D. V. Helmberger (1983), The near-source ground motion of the 6 August 1979 Coyote Lake, California, earthquake, *Bull. Seismol. Soc. Am.*, *73*(1), 201–218.

Liu, Y., and J. R. Rice (2007), Spontaneous and triggered aseismic deformation transients in a subduction fault model, *J. Geophys. Res.*, *112*, B09404, doi:10.1029/2007JB004930.

Liu, Y., and J. R. Rice (2009), Slow slip predictions based on granite and gabbro friction data compared to GPS measurements in northern Cascadia, *J. Geophys. Res.*, *114*, B09407, doi:10.1029/2008JB006142.

Ma, K.-F., J. Mori, S.-J. Lee, and S. B. Yu (2001), Spatial and temporal distribution of slip for the 1999 Chi-Chi, Taiwan, earthquake, *Bull. Seismol. Soc. Am.*, *91*(5), 1069–1087.

Ma, K.-F., et al. (2006), Slip zone and energetics of a large earthquake from the Taiwan Chelungpu-fault drilling project, *Nature*, *444*, 473–476, doi:10.1038/nature0525.

Ma, S., S. Custodio, R. J. Archuleta, and P. Liu (2008), Dynamic modeling of the 2004 Mw 6.0 Parkfield, California, earthquake, *J. Geophys. Res.*, *113*, B02301, doi:10.1029/2007JB005216.

Magee, M. E., and M. D. Zoback (1993), Evidence of a weak interplate thrust fault along the northern Japan subduction zone and implications for the mechanics of thrust faulting and fluid expulsion, *Geology*, *21*, 809–812.

Mase, C. W., and L. Smith (1987), Effects of frictional heating on the thermal, hydrologic, and mechanical response of a fault, *J. Geophys. Res.*, *92*, 6249–6272.

McGuire, J. J., and P. Segall (2003), Imaging of aseismic fault slip transients recorded by dense geodetic networks, *Geophys. J. Int.*, *155*, 778–788.

Mendoza, C., and S. H. Hartzell (1988), Inversion for slip distribution using teleseismic P waveforms: North Palm Springs, Borah Peak, and Michoacan earthquakes, *Bull. Seismol. Soc. Am.*, *78*(3), 1092–1111.

Mikumo, T. K., K. B. Olsen, E. Fukuyama, and Y. Yagi (2003), Stress-breakdown time and slip-weakening distance inferred from slip-velocity functions on earthquake faults, *Bull. Seismol. Soc. Am.*, *93*, 264–282.

Mizoguchi, K., T. Hirose, T. Shimamoto, and E. Fukuyama (2008), Internal structure and permeability of the Nojima fault, southwest Japan, *J. Struct. Geol.*, *30*, 513–524, doi:10.1016/j.jsg.2007.12.002.

Muskhelishvili, N. (1977), *Singular Integral Equations*, Noordhoff Int., Leyden, Netherlands.

Nielsen, S., and R. Madariaga (2003), On the self-healing fracture mode, *Bull. Seismol. Soc. Am.*, *93*(6), 2375–2388.

Noda, H., and N. Lapusta (2010), Three-dimensional earthquake sequence simulations with evolving temperature and pore pressure due to shear heating: Effect of heterogeneous hydraulic diffusivity, *J. Geophys. Res.*, *115*, B12314, doi:10.1029/2010JB007780.

Noda, H., and T. Shimamoto (2005), Thermal pressurization and slip-weakening distance of a fault: An example of the Hanaore fault, southwest Japan, *Bull. Seismol. Soc. Am.*, *95*(4), 1224–1233, doi:10.1785/0120040089.

Noda, H., E. M. Dunham, and J. R. Rice (2009), Earthquake ruptures with thermal weakening and the operation of major faults at low overall stress levels, *J. Geophys. Res.*, *114*, B07302, doi:10.1029/2008JB006143.

Palmer, A. C., and J. R. Rice (1973), The growth of slip surfaces in the progressive failure of over-consolidated clay, *Proc. R. Soc. London*, *433*, 469–477.

Perrin, G., J. R. Rice, and G. Zheng (1995), Self-healing slip pulse on a frictional surface, *J. Mech. Phys. Solids*, *43*, 1461–1495.

Platt, J., J. R. Rice, and J. W. Rudnicki (2010), Strain localization within a fluid-saturated fault gouge layer during seismic shear, Abstract T31D-03 presented at 2010 Fall Meeting, AGU, San Francisco, Calif., 13–17 Dec.

Rempel, A. W., and J. R. Rice (2006), Thermal pressurization and onset of melting in fault zones, *J. Geophys. Res.*, *111*, B09314, doi:10.1029/2006JB004314.

Rice, J. R. (1968), Mathematical analysis in the mechanics of fracture, in *Fracture, an Advanced Treatise*, vol. II, edited by H. Liebowitz, chap. 3, pp. 191–311, Academic, New York.

Rice, J. R. (1980), The mechanics of earthquake rupture, in *Physics of the Earth's Interior*, edited by A. Dziewonski and E. Boschi, *Proc. Int. Sch. Phys. Enrico Fermi*, *78*, 555–649.

Rice, J. R. (1992), Fault stress states, pore pressure distributions, and the weakeness of the San Andreas fault, in *Fault Mechanics and Transport Properties of Rock: A Festschrift in Honor of W. F. Brace*, edited by B. Evans and T.-F. Wong, pp. 475–503, Academic, San Diego, Calif.

Rice, J. R. (1999), Flash heating at asperity contacts and rate-dependent friction, *EOS Trans. AGU*, *80*(46), Fall Meet. Suppl., F681.

Rice, J. R. (2006), Heating and weakening of faults during earthquake slip, *J. Geophys. Res.*, *111*, B05311, doi:10.1029/2005JB004006.

Rice, J. R., C. G. Sammis, and R. Parsons (2005), Off-fault secondary failure induced by a dynamic slip pulse, *Bull. Seismol. Soc. Am.*, *95*(1), 109–134, doi:10.1785/0120030166.

Rubin, A. M., and J.-P. Ampuero (2005), Earthquake nucleation on (aging) rate and state faults, *J. Geophys. Res.*, *110*, B11312, doi:10.1029/2005JB003686.

Rubin, A. M., and J.-P. Ampuero (2009), Self-similar slip pulses during rate-and-state earthquake nucleation, *J. Geophys. Res.*, *114*, B11305, doi:10.1029/2009JB006529.

Schwartz, S., and J. M. Rokosky (2007), Slow slip events and seismic tremor at circum-Pacific subduction zones, *Rev. Geophys.*, *45*, RG3004, doi:10.1029/2006RG000208.

Segall, P., and J. R. Rice (1995), Dilatancy, compaction, and slip instability of a fluid-infiltrated fault, *J. Geophys. Res.*, *100*, 22,155–22,171.

Segall, P., and J. R. Rice (2006), Does shear heating of pore fluid contribute to earthquake nucleation?, *J. Geophys. Res.*, *111*, B09316, doi:10.1029/2005JB004129.

Segall, P. A., A. M. Rubin, A. M. Bradley, and J. R. Rice (2010), Dilatant strengthening as a mechanism for slow slip events, *J. Geophys. Res.*, *115*, B12305, doi:10.1029/2010JB007449.

Shelly, D. R., G. C. Beroza, S. Ide, and S. Nakamula (2006), Low-frequency earthquakes in Shikoku, Japan, and their relationship to episodic tremor and slip, *Nature*, *442*, 188–191, doi:10.1038/nature04931.

Sibson, R. (1973), Interaction between temperature and fluid pressure during earthquake faulting—A mechanism for partial or total stress relief, *Nature*, *243*, 66–68.

Sibson, R. H., and V. G. Toy (2006), The habitat of fault-generated pseudotachylyte: Presence vs. absence of friction-melt, in *Earthquakes: Radiated Energy and the Physics of Faulting*, *Geophys. Monogr. Ser.*, vol. 170, edited by R. Abercrombie et al., pp. 153–166, AGU, Washington, D. C., doi:10.1029/170GM16.

Sladen, A., et al. (2010), Source model of the 2007 Mw 8.0 Pisco, Peru earthquake: Implications for seismogenic behavior of subduction megathrusts, *J. Geophys. Res.*, *115*, B02405, doi:10.1029/2009JB006429.

Tanikawa, W., and T. Shimamoto (2009), Frictional and transport properties of the Chelungpu fault from shallow borehole data and their correlation with seismic behavior during the 1999 Chi-Chi earthquake, *J. Geophys. Res.*, *114*, B01402, doi:10.1029/2008JB005750.

Tinti, E., P. Spudich, and M. Cocco (2005), Earthquake fracture energy inferred from kinematic rupture models on extended faults, *J. Geophys. Res.*, *110*, B12303, doi:10.1029/2005JB003644.

Tinti, E., P. Spudich, and M. Cocco (2008), Correction to "Earthquake fracture energy inferred from kinematic rupture models on extended faults," *J. Geophys. Res.*, *113*, B07301, doi:10.1029/2008JB005829.

Townend, J., and M. D. Zoback (2004), Regional tectonic stress near the San Andreas fault in central and southern California, *Geophys. Res. Lett.*, *31*, L15S11, doi:10.1029/2003GL018918.

Uenishi, K., and J. R. Rice (2003), Universal nucleation length for slip-weakening rupture instability under nonuniform fault loading, *J. Geophys. Res.*, *108*(B1), 2042, doi:10.1029/2001JB001681.

Venkataraman, A., and H. Kanamori (2004), Observational constraints on the fracture energy of subduction zone earthquakes, *J. Geophys. Res.*, *109*, B05302, doi:10.1029/2003JB002549.

Vredevoogd, M., D. Oglesby, and S. Park (2007), Effect of non-linear terms on pore fluid pressurization, paper presented at SCEC Annual Meeting, Southern Calif. Earthquake Cent., Palm Springs.

Wald, D. J. (1996), Slip history of the 1995 Kobe, Japan earthquake determined from strong motion, teleseismic, and geodetic data, *J. Phys. Earth*, *44*, 489–503.

Wald, D. J., and T. H. Heaton (1994), Spatial and temporal distribution of slip for the 1992 Landers, California, earthquake, *Bull. Seismol. Soc. Am.*, *84*(3), 668–691.

Wald, D. J., D. V. Helmberger, and S. H. Hartzell (1990), Rupture process of the 1987 Superstition Hills earthquake from the inversion of strong-motion data, *Bull. Seismol. Soc. Am.*, *80*(5), 1079–1098.

Wald, D. J., D. V. Helmberger, and T. H. Heaton (1991), Rupture model of the 1989 Loma Prieta earthquake from the inversion of strong-motion and broadband teleseismic data, *Bull. Seismol. Soc. Am.*, *81*(5), 1540–1572.

Wald, D. J., T. H. Heaton, and K. W. Hudnut (1996), The slip history of the 1994 Northridge, California, earthquake determined from strong ground motion, teleseismic, GPS, and leveling data, *Bull. Seismol. Soc. Am.*, *86*(1B), S49–S70.

Wang, K., T. Mulder, G. C. Rogers, and R. D. Hyndman (1995), Case for very low stress on the Cascadia subduction fault, *J. Geophys. Res.*, *100*(B7), 12,907–12,918.

Weertman, J. (1980), Unstable slippage across a fault that separates elastic media of different elastic constants, *J. Geophys. Res.*, *85*(B3), 1455–1461.

Wibberley, C. A. J. (2002), Hydraulic diffusivity of fault gouge zones and implications for thermal pressurization during seismic slip, *Earth Planets Space*, *54*, 1153–1171.

Wibberley, C. A. J., and T. Shimamoto (2003), Internal structure and permeability of major strike-slip fault zones: The median tectonic line in Mie prefecture, southwest Japan, *J. Struct. Geol.*, *25*(1), 59–78.

Zheng, G., and J. R. Rice (1998), Conditions under which velocity-weakening friction allows a self-healing versus a cracklike mode of rupture, *Bull. Seismol. Soc. Am.*, *88*(6), 1466–1483.

D. I. Garagash, Department of Civil and Resource Engineering, Dalhousie University, 1360 Barrington St., Halifax, NS B3J 1Z1, Canada. (garagash@dal.ca)